\

Preparation of nickel-based oxide photocatalytic nano materials and their application in hydrogen production

A dissertation submitted in complete fulfilment of the requirements for the degree of Doctor of Philosophy

Jiayou Mou

February 2025

Supervised by

Prof. Yong Ren

Prof. Yong Shi

Prof. Yuying Yan

Department of Mechanical, Materials and Manufacturing Engineering

University of Nottingham

\

Abstract

This thesis investigates the synthesis and application of Ni_2O_3 nanoparticles in photocatalytic hydrogen generation, employing a novel microfluidic synthesis method based on a centrifugal microfluidic chip platform and a traditional participation method. The research analyzed the influence of different factors in microfluidic synthesis procedure. The next study focuses on the development of a TiO_2-Ni_2O_3/carbon nanotube (CNT) heterojunction composite that serves as an effective catalyst for hydrogen production. The synthesized composite achieved an impressive hydrogen generation rate of 1422 μmol/g/h in full light condition, outperforming traditional TiO_2 catalysis by more than eleven times. Characterization techniques such as X-ray Diffraction (XRD), High-Resolution Transmission Electron Microscopy (HRTEM), X-ray Photoelectron Spectroscopy (XPS), UV-Visible spectroscopy, photocurrent measurements, photoluminescence (PL), and Electrochemical Impedance Spectroscopy (EIS) were employed to elucidate the composite's morphology, structure, and optical properties. These analyses revealed that the incorporation of Ni_2O_3 significantly improved light absorption and charge separation efficiency, critical factors for effective photocatalysis and the characterization results should be interpreted with caution and are primarily valid for intragroup comparisons due to variations in sample synthesis and processing conditions. A core-shell structure was formed through calcination at

\

800°C, comprising Ni as the outer shell, NiO as an intermediate layer, and Ni_2O_3 as the core. This unique architecture optimized electron transfer and enhanced carrier lifetime, with electron lifetime increasing from 1.44 ns to 2.18 ns after treatment. Consequently, photocatalytic performance markedly improved, achieving a hydrogen generation rate of 2626.7 μmol/g/h under full light conditions. Moreover, the carbon footprint associated with hydrogen production was measured at 81.91 kg CO_2-equivalent per kg of H_2 produced, indicating environmental considerations in the process, with potential reductions through the use of renewable energy sources and recycling techniques. Composites are all synthesized from conventional method as the microfluidic tube may be clogged by solid reactants. Additionally, as some of the characterizations were not applied at the same time, therefore, the variation between groups may exist, however, the results are still valid for intragroup comparative analysis. it This work highlights a promising, cost-effective approach to photocatalytic hydrogen generation and provides valuable insights into optimizing catalysts for sustainable energy solutions. By advancing our understanding of Ni_2O_3's role in photocatalytic systems, this research contributes to the broader field of renewable energy technologies, emphasizing the importance of efficient materials and processes in addressing the global energy problem.

\

Acknowledgements

During the past four years of my PhD, I have gained a lot and learned a great deal. I have acquired many experiences and lessons, learned various life philosophies, and understood the hardships and challenges of research. I would like to take this opportunity to thank those who have helped, encouraged, and supported me throughout these four years, and to express my gratitude for their contributions and support

First and foremost, I would like to express my heartfelt gratitude to my supervisor, professor. Yong Ren, whose unwavering support, guidance, and encouragement have been instrumental in completing this research. From the initial stages of formulating my research proposal to the final stages of writing this thesis. Prof. Shi Yong and Prof. Yuying Yan has consistently provided invaluable insights and constructive feedback that have profoundly shaped my work. Their passion for research and commitment to excellence have inspired me to strive for the highest standards in my own work.

I am also deeply thankful to my committee members, Dr Kok Hoong Wong, for the expert guidance and insightful discussions throughout my doctoral journey. He diverse perspectives and suggestions have significantly enhanced the quality of my research and broadened my understanding of the field.

I would like to extend my appreciation to my fellow colleagues and friends in Prof. Yong Ren's group and China beacon instate of UNNC. The

camaraderie and collaboration within our group have made this challenging journey enjoyable and fulfilling. In particular, I want to thank Zhiyu Zhang, Guanlin Zhang, Run Pan, Zhiyu Xiao for their constant support, brainstorming sessions, and moral encouragement. Our countless discussions, both academic and personal, have enriched my experience at University of Nottingham Ningbo China.

I gratefully acknowledge the financial support received from UNNC and CBI, which has been critical to the completion of my research. This funding allowed me to focus on my studies and explore new avenues of inquiry without the burden of financial constraints. I would also like to recognize the resources and facilities provided by CBI, which have been essential for conducting my experiments and achieving my research objectives.

A special mention goes to the administrative staff of the CBI whose assistance with the myriad logistical details has made my life considerably easier. Their efficiency and willingness to help have ensured that I could concentrate on my research efforts.

I must also express my profound gratitude to my family, especially my parents, whose unwavering belief in me and sacrifices have laid the foundation for my academic pursuits. Your love, encouragement, and moral support have been my anchor through the challenges of graduate school. Moreover, I want to thank my wife, thank you for your support

and encouragement, thank you for your contribution for the family, thank you for give me the most precious treasure, an adorable daughter, love you.

Last but certainly not least, I want to acknowledge every participant who contributed to my research; your willingness to share your experiences and insights was invaluable. Without your contributions, this thesis would not have been possible.

As I conclude this acknowledgment, I reflect on the countless individuals who have influenced my journey. Each of you has played a vital role in shaping me as a researcher and person. I am truly grateful for your support, mentorship, and friendship over these years.

\

Contents

\

Achievements

- **Mou J**, Wang C, Zhao H, Xiong C, Ren Y, Wang J, Jiang D, Zheng Z. Centrifugal Microfluidic Synthesis of nickel Sesquioxide Nanoparticles. Micromachines (Basel). 2023 Sep 6;14(9):1741. doi: 10.3390/mi14091741. PMID: 37763904; PMCID: PMC10538187.

- **Mou, J**., Ren, Y., Wang, J., Wang, C., Zou, Y., Lou, K., Zheng, Z., & Zhang, D. (2022). Nickel oxide nanoparticle synthesis and photocatalytic applications: evolution from conventional methods to novel microfluidic approaches. Microfluidics and Nanofluidic, 26. https://doi.org/10.1007/s10404-022-02534-2

- **Mou, J**., Wang, C., Pan, R., Zhang, G et al., A novel z-type heterojunction Ni2O3 composite catalyst for photocatalytic hydrogen generation. International Journal of Hydrogen Energy. (Required reviews complete)

- **Mou, J**., Wang, C., Pan, R., Zhang, G et al., Core-shell NiO_x - TiO_2/CNT photocatalyst for efficient hydrogen production. (Under preparation)

- Wang, C., **Mou, J**., Erfani, T., Wu, T. Impacts of different waste treatment scenarios on carbon footprint of municipal solid waste: A case study of Shanghai City, China. 2022. Journal of Environmental Management. (Revised manuscript submitted).

\

- Wang, C., Parvez, A., **Mou, J**., Wu, T. et al. The status and opportunities for improvement on the path to carbon neutrality of a campus in China: A case study for the energy transition and innovation perspectives. 2024 Journal of Cleaner Production. DOI: https://doi.org/10.1016/j.jclepro.2023.137521.

- Zhu J, Qin Z, Lan A, Jiang S, **Mou J**, Ren Y, Do H, Chen ZK, Chen F. A-D-A Type Norfullerene Acceptors Synthesized by Core Segmentation and Isomerization for Realizing Organic Solar Cells with Low Nonradiative Energy Loss. Small. 2024 Jan;20(3):e2305529. doi: 10.1002/smll.202305529. Epub 2023 Sep 8. PMID: 37688316.

\

List of abbreviations

CB	Conduction band
CNT	Carbon nanotubes
Eds	Energy dispersive spectrometer
EIS	Electrochemical impedance
FT-IR	Fourier transform infrared
GC	Gas chromatograph
HER	Hydrogen evolution reaction
IPCC	The Intergovernmental Panel on Climate Change
LCA	Life cycle assessment
OER	Oxygen evolution reaction
PDMS	Polydimethylsiloxane
PL	Photoluminescent
SEM	Scanning electron microscope
TEM	Transmission electron microscopy
TEOA	Triethanolamine
TRPL	Time-Resolved Photoluminescence
UV-vis	Ultraviolet–visible spectroscopy

\

VB	Valence band
VOF	Volume of fluid
XPS	X-ray photoelectron spectroscopy
XRD	X-ray diffraction

List of symbols

AD_i	Process activity data
E_i	Carbon emissions from source i
EF_i	Carbon emissions factor of activity i
A	Proportionality constant
E_g	Optical band gap energy
f	external force per unit volume of fluid
g	Gravity
hv	Photon energy
n	Power index
p	Pressure
r	Radius
t	Time
V	Velocity vector
v	Velocity
α	Absorption coefficient
λ	Wavelength
μ	Dynamic viscosity
ρ	Density
ω	Angular velocity
R_s	Solution resistance

\

R_{ct}	Charge transfer resistance

List of tables

\

List of figures

\

1 Chapter 1. General overview

1.1 Introduction

With the global shift toward clean energy and the need to reduce dependence on fossil fuels, photocatalytic hydrogen generation has garnered significant attention due to its potential to provide a sustainable and eco-friendly alternative for hydrogen production. By producing hydrogen without emitting greenhouse gases, this process could play a crucial role in addressing the energy and environmental challenges of the future. However, the widespread adoption of photocatalytic hydrogen generation faces challenges such as low efficiency, catalyst stability, and cost. Nickel trioxide (Ni_2O_3) has emerged as a promising material for photocatalytic applications due to its unique chemical structure and high oxidation state of nickel. As an advanced oxide, Ni_2O_3 has attracted significant attention in photocatalysis, particularly for water splitting and hydrogen generation processes, which are crucial for the development of sustainable energy systems. Unlike more commonly used photocatalysts, such as titanium dioxide (TiO_2), nickel trioxide possesses the ability to undergo reversible redox reactions due to the high-valence state of nickel, allowing it to facilitate various catalytic cycles. Its ability to absorb light and drive oxidation reactions makes it suitable for photocatalytic processes, where it can participate in both oxygen evolution and

\

hydrogen evolution reactions. Additionally, the material's stability under light irradiation and its potential for enhancing the efficiency of photocatalytic systems make it an attractive candidate for further investigation. Despite challenges related to the synthesis and stability of nickel trioxide, ongoing research into its electronic properties and interactions in photocatalytic systems holds promise for improving the overall performance of photocatalytic water splitting and other related reactions. This makes nickel trioxide an important material for advancing clean energy technologies and contributing to the development of efficient, sustainable hydrogen production methods. In order to synthesized the nano particles significantly, microfluidic technology has been adopted in the synthesized process. Microfluidic synthesis of nanoparticles represents a highly controlled and efficient method for producing nanomaterials with precise size, shape, and composition. This technique utilizes micro-scale devices that manipulate small volumes of fluids in channels with dimensions typically in the range of tens to hundreds of micrometers. The controlled environment of microfluidic systems allows for rapid mixing, precise reaction control, and better uniformity in particle formation, making it an ideal platform for the synthesis of nanoparticles. Unlike traditional precipitation synthesis methods, microfluidics enables the production of nanoparticles with highly reproducible properties, such as

narrow size distributions, enhanced surface areas, and well-defined morphologies.

1.2 Aims and objectives

The aim of this project is to combine microfluidics with traditional nanoparticle precipitation methods to fabricate uniform, controllable, and high-quality nickel trioxide (Ni_2O_3) nanoparticles. Meanwhile, by leveraging the unique catalytic and optoelectronic properties of Ni_2O_3, to optimize traditional catalysts, resulting in reliable, low-cost photocatalytic hydrogen production catalysts. Additionally, through the doping of nickel elements in different oxidation states and the design of core-shell structures, the catalytic performance of the catalyst is further enhanced, ensuring that the catalyst maintains relatively high photocatalytic hydrogen production performance while being simple to prepare and cost-effective.

The main research objectives are:

1. To review the literature on the researches of conventional synthesis methods of nickel based nano particles and microfluidic fabrication methods of different experiments.
2. Combined the conventional synthesized method with microfluidic platform to synthesis uniformly, size controllable Ni_2O_3 nano particles.
3. To investigate the properties and performance of TiO_2- Ni_2O_3 /CNT (TNC) composite in photocatalytic hydrogen evolution.

\

4. To investigate the properties and performance of core-shell structure composites of TN_xC in photocatalytic hydrogen evolution reaction.

1.3 Thesis structure:

In chapter 2, a detailed literature is given about the conventional synthesized method of nickel based nano particles and presented the advantages and disadvantages of different methods. Meanwhile, introducing some examples of microfabrication of nano particles and induced their advantages and application methods. By comparing the conventional synthesis methods and microfluidic synthesis methods to find an efficient combination method to synthesized nickel trioxide nano particles. This section also gave a comparison of different composite of hydrogen generation including titanium oxide and nickel trioxide, it has been well reviewed of different composites about their generation rate, principle and costs.

In chapter 3, the details of experimental procedure has been listed include microfluidic synthesized process, hydrogen generation process, catalyst synthesized process with the medicine involved. The chapter also provided the characterized methods and a brief description of life cycle assessment standard.

\

In chapter 4, the simulation model and experimental results of centrifugal microfluidic synthesized method has been investigated. The 80nm Ni_2O_3 nano particles has been successfully fabricated.

In chapter 5, TiO_2-Ni_2O_3/CNT (TNC) has been successfully fabricated through a simple one-pot method. The generate rate of the composite is 1400μmol/g/h which is 11 times more than TiO_2 nanoparticles. The composite was designed as a z-type heterojunction to enhance the electron transfer and active time, the electron-photo characters has been analyzed in the chapter.

In chapter 6, the core-shell composite of TNC was synthesized based on chapter 5. By recovering the outside Ni_2O_3 into NiO and Ni, to decrease the resistance inside the composite and improve the electron separation. The generation rate reaches more than 2626.7 μmol/g/h.

In chapter 7, a summary of catalysis performance and synthesis procedure is given. Catalyst fabricated though microfluidic method has better uniformity and quality. Z-type heterojunction and core-shell structure of TNC significantly improve the hydrogen evolution efficiency through enhancing the electron and photo properties. After that, the future plan on improving the catalysis efficiency and strategies for microfluidic synthesis has been proposed.

\

2 Chapter 2. Literature Review

2.1 Photocatalysis hydrogen generation

Photocatalysis for hydrogen generation has emerged as a pivotal research domain due to its potential to address the global energy crisis sustainably. The process hinges on the utilization of photocatalysts, typically semiconductors, to harness light energy and split water into hydrogen and oxygen.

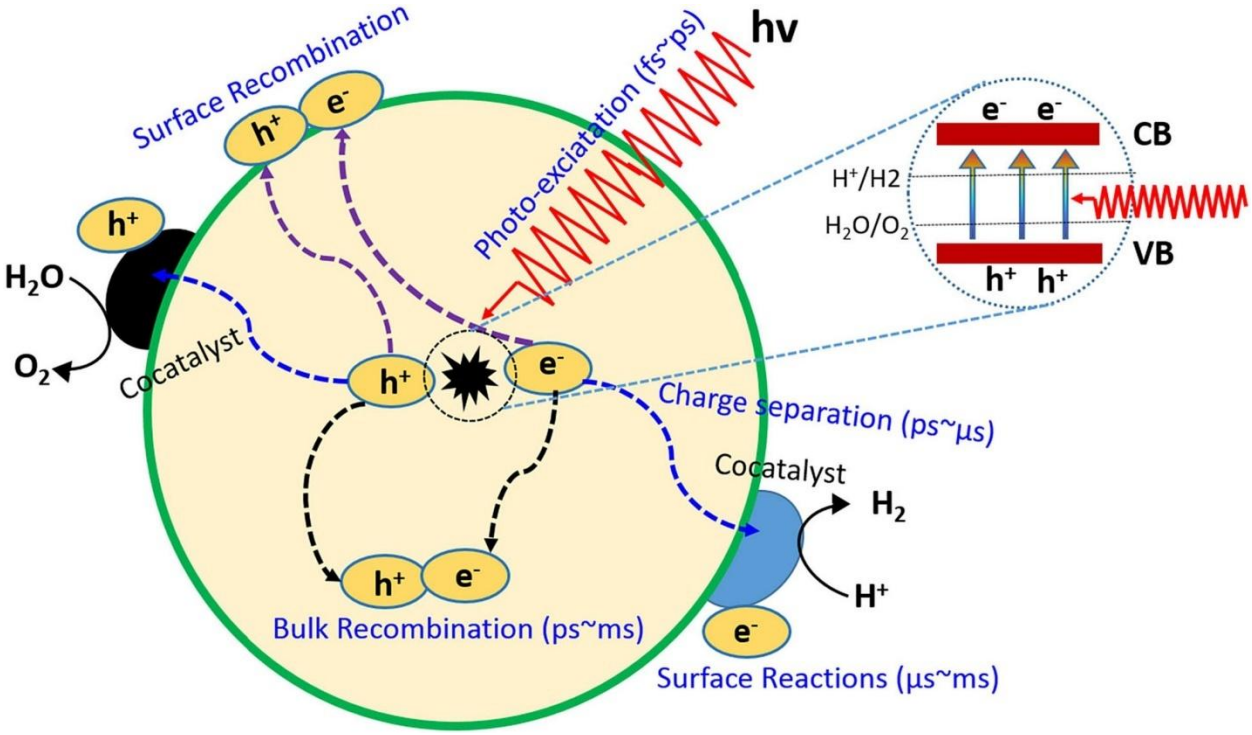

Figure 2-1 Scheme of essential steps for photocatalytic full-water splitting with cocatalysts. [1] .

The full-water splitting process includes three main steps as shown in figure 2-1. Firstly, the electrons and holes are created by the absorption

\

of light with λ bigger than the semiconductor band gap. After that, some of electrons and holes will separate and move to catalyst surface, others will recombined and release heat. On the surface of catalyst, the reduction and oxidation reactions will happen. For reduction reactions, H^+ get separated electrons becomes H_2. On the oxidation sides, H_2O reacts with holes and get positive charge then created H^+. The reduction process is called HER (hydrogen evolution reaction) and the oxidized one is called OER (oxygen evolution reaction). OER reaction is a 4 charges reaction with relative high energy barrier and slow reaction kinetics, which directly affect the overall energy efficiency of the water-splitting process. In order to solve the restriction of OER process and improve the efficiency of water splitting, sacrificial agents are involved. After adding sacrificial agents the photo generated holes (h^+) will consumed by sacrificial agents instead of H_2O as sacrificial agents has lower oxidation state than H_2O [2] [3]. The widely used sacrificial agents are mainly divided in two categories: organic sacrificial agents: triethanolamine, Methanol and Ethanol [4] [5] [6]. Inorganic type: Sulfide Ions (e.g., Na_2S or Na_2SO_3) [7].

Semiconductors such as titanium dioxide (TiO_2) [8] [9], zinc oxide (ZnO) [10] [11] [12], and cadmium sulfide (CdS) [13] have been extensively investigated for their photocatalytic properties. TiO_2, in particular, has garnered significant attention due to its chemical stability, low cost, and non-toxicity. However, TiO_2 is limited by its wide

band gap of 3.2 eV, restricting its activity to ultraviolet (UV) light, which constitutes only 4-5% of solar energy [14]. To overcome this limitation, strategies such as doping with transition metals (e.g., Fe [15], Cu [16], Cr [17]) or non-metals (e.g., N [18], C [19], S [20]), coupling with narrow-bandgap semiconductors, and introducing surface plasmon resonance effects by integrating noble metals like gold and silver have been explored [21]. Transition metal doping introduces mid-gap states, enabling visible-light absorption, but can increase charge recombination. Non-metal doping, particularly nitrogen, has shown promise in reducing the bandgap while maintaining TiO_2's stability.

Beyond TiO_2, alternative semiconductors such as ZnO and CdS have been explored for their narrower band gaps and better visible-light responsiveness. ZnO shares many properties with TiO_2 but suffers from photo-corrosion under prolonged operation [22] [23]. CdS, with a band gap of 2.4 eV, enables efficient visible-light absorption but is limited by its susceptibility to photo corrosion and toxicity[24-26]. Recent advances in the field have introduced novel photocatalysts such as graphitic carbon nitride (g-C_3N_4), a metal-free material with excellent photocatalytic efficiency under visible light. The heptazine-based polymeric structure of g-C_3N_4 provides a narrow band gap of ~2.7 eV, along with good thermal and chemical stability, making it a viable alternative to traditional metal-based photocatalysts[27-29]. Efforts to enhance the performance of g-C_3N_4 include doping with non-metals

\

such as phosphorus and sulfur, as well as constructing heterojunctions with materials like TiO_2[30, 31] or MoS_2[32, 33] to improve charge separation and broaden light absorption.

The incorporation of co-catalysts has played a transformative role in improving photocatalytic hydrogen generation. Noble metals such as platinum (Pt) [34] and palladium (Pd) [35] are among the most effective hydrogen evolution co-catalysts due to their excellent conductivity and low overpotential for hydrogen evolution reactions. However, the high cost and scarcity of noble metals have driven the search for alternatives. Transition metal phosphides (e.g., Ni_2P [36]), carbides [37], and sulfides [38] have emerged as promising substitutes, offering comparable performance at a fraction of the cost. For example, nickel-based compounds have demonstrated remarkable activity and stability when coupled with semiconductor photocatalysts such as g-C_3N_4 or ZnO. Furthermore, the use of dual co-catalyst systems, combining hydrogen evolution and oxygen evolution catalysts, has shown to significantly enhance overall water-splitting efficiency.

2.2 Nano structure and effect

Nano structuring plays a crucial role in enhancing the photocatalytic performance of materials by improving key factors such as surface area, charge separation, and light absorption. By reducing the particle size, nanostructured photo catalysts, such as nanoparticles, nanowires,

\

and nano sheets, offer a larger surface area that increases the number of active sites for reactions. This can significantly improve the photocatalytic efficiency, as seen in materials like TiO_2 nanoparticles [39] and g-C_3N_4 Nano sheets [40], which exhibit superior photocatalytic activity compared to their bulk counterparts. Moreover, nanostructuring reduces charge recombination rates, which is essential for maintaining the generation of electron-hole pairs. For example, composites like ZnO/rGO [41] and TiO_2 nanowires [42]demonstrate enhanced charge transport and separation, thereby boosting photocatalytic performance. Additionally, nanoscale materials can exhibit quantum size effects, which influence light absorption properties and allow for tuning the bandgap for better utilization of visible light, further improving photocatalytic applications such as CO_2 reduction and pollutant degradation [43, 44].

Core-shell structures, where a photocatalytic material (such as TiO_2 or CdS) is coated with another material (such as graphene oxide or a noble metal), are particularly effective in improving charge carrier dynamics. The core material often serves as the active photocatalyst, while the shell material can prevent charge recombination, enhance light absorption, and offer stability under reaction conditions. For example, core-shell TiO_2@Ag [45] (silver-coated TiO_2) nanostructures have demonstrated superior photocatalytic efficiency due to the plasmonic enhancement of silver, which increases light absorption and

\

facilitates charge separation. Similarly, ZnO@ZnS core-shell nanostructures exhibit improved photocatalytic dyes degradation, attributed to the enhanced electron transport and reduced recombination due to the ZnS shell [46]. Additionally, the core-shell design allows for better durability under harsh photocatalytic conditions, extending the material's lifespan in practical applications.

In addition to charge separation, core-shell structures can further tailor the electronic properties of photocatalysts by adjusting the bandgap, enhancing visible light absorption, and reducing electron-hole recombination. This is crucial for improving the efficiency of photocatalytic reactions such as pollutant degradation and water splitting [47] [48] . The versatility of core-shell designs offers exciting opportunities for optimizing photocatalytic materials and broadening their applications in renewable energy and environmental remediation.

2.3 Heterostructure design and influence

Heterostructure engineering has revolutionized the field of photocatalysis by enabling more efficient charge separation and transfer. As shown in figure 2-2, Type I heterojunction means both the conduction band minimum (CBM) and valence band maximum (VBM)

of one semiconductor lie within the bandgap of the other semiconductor, both electrons and holes will come to the same material. Type-II heterojunctions, where the conduction band of one semiconductor aligns with the valence band of another, facilitate spatial separation of photogenerated charge carriers. Examples include TiO_2-Cu_2O [35], C_2N/WS_2 [49] and $Cu_2O/ZnFe_2O_4$ [50] systems, which have demonstrated superior photocatalytic activity compared to their individual components. Another advanced concept, Z-scheme heterojunctions, mimics natural photosynthesis by using two semiconductors with staggered band alignments to retain strong redox potentials while suppressing recombination [51] [52]. For instance, a Z-scheme system comprising ZnO and $CeVO_4$ [24] has shown enhanced hydrogen evolution under visible-light irradiation with the hydrogen generation rate of 1289μmol/g/h.

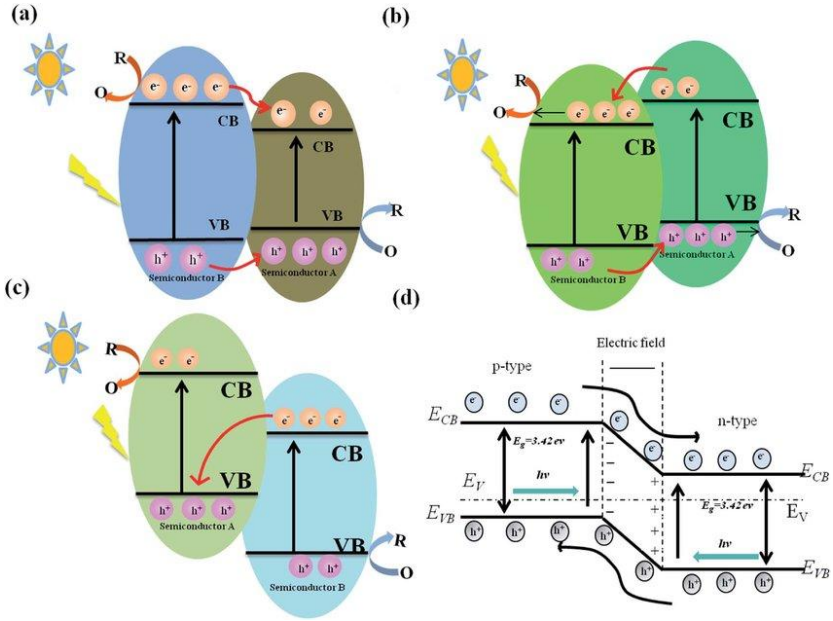

\

Figure 2-2 Different types of heterojunctions. (a) Type I heterojunction model. (b) Type II heterojunction model. (c) Z-type heterojunction model. (d) p-n heterojunction model [53].

Nanostructure engineering has further advanced photocatalytic hydrogen generation by increasing surface area, active sites, and light-harvesting capabilities. Nanorods, nanosheets, and quantum dots have been integrated into photocatalytic systems to enhance light absorption and reaction kinetics. For example, CdS quantum dots [54] have been employed in photoelectrochemical cells to achieve high hydrogen evolution rates under visible light. Similarly, black phosphorus nanosheets have emerged as efficient co-catalysts, offering high conductivity and strong interaction with semiconductor substrates [55].

Emerging trends in computational materials science and machine learning have significantly accelerated the discovery and optimization of photocatalysts. Density functional theory (DFT) calculations provide insights into electronic band structures, surface energetics, and charge transfer processes, enabling the rational design of materials with tailored properties). Machine learning models, trained on large datasets of material properties, have been employed to predict key activity descriptors, such as band gap, conduction band alignment, and light absorption efficiency . The integration of computational and experimental techniques is paving the way for high-throughput

\

screening and the discovery of novel photocatalytic materials [56] [57] [58].

Despite these advancements, several challenges remain in the quest for economically viable photocatalytic systems. One of the critical barriers is the rapid recombination of photogenerated electron-hole pairs, which significantly reduces photocatalytic efficiency . Strategies to mitigate this include surface passivation, defect engineering, and the use of photosensitizers such as perovskite nanocrystals. Photoelectrochemical systems that combine photocatalysis with an applied electrical bias offer an effective solution to overcome the kinetic and thermodynamic barriers associated with water splitting. Economic and environmental sustainability considerations are increasingly influencing research directions. The use of earth-abundant materials, such as Fe-based or Ni-based catalysts, offers a cost-effective alternative to noble metals. Additionally, scalable synthesis techniques, such as hydrothermal or sol-gel methods, are being developed to fabricate high-performance photocatalysts at reduced costs.

The integration of experimental innovations, computational tools, and sustainable material design will play a pivotal role in advancing the field of photocatalytic hydrogen generation. As global energy demands rise, the development of efficient, durable, and cost-effective photocatalytic

\

systems remains an essential research priority to enable the transition to a sustainable energy future.

Nickel(III) oxide (Ni_2O_3) has emerged as a promising material for photocatalytic hydrogen generation due to its unique electronic properties, high oxidation state, and ability to absorb visible light [59]. As a p-type semiconductor, Ni_2O_3 has a narrow bandgap that facilitates efficient light absorption and the generation of electron-hole pairs, which are crucial for water-splitting reactions. In photocatalysis, Ni_2O_3 primarily contributes to the oxygen evolution reaction (OER) due to its strong oxidizing potential, while also serving as a co-catalyst to enhance the hydrogen evolution reaction (HER) by improving charge carrier dynamics and reducing recombination [60]. Various synthesis methods, including sol-gel, hydrothermal, and chemical vapor deposition, have been employed to produce Ni_2O_3 with tailored properties, such as particle size, crystallinity, and morphology, which significantly influence its photocatalytic performance. To overcome its limitations, including charge recombination and moderate stability under light irradiation, Ni_2O_3 is often combined with other materials to form heterostructures or composites, such as MCM-48/Ni_2O_3 [61] and Hu/PANI@Ni_2O_3 [62] systems, which exhibit enhanced charge separation, extended light absorption into the visible spectrum, and improved hydrogen production rates. Additionally, doping strategies using elements like cobalt and lanthanides have been explored to

optimize its electronic properties, while plasmonic enhancements involving gold or silver nanoparticles have shown potential for increasing light absorption through localized surface plasmon resonance (LSPR). Despite these advancements, challenges such as stability under prolonged operational conditions and the scalability of Ni_2O_3-based photocatalytic systems persist, necessitating further research into cost-effective synthesis techniques, material durability, and environmental performance. Ni_2O_3's ability to serve as an efficient and sustainable photocatalyst for hydrogen generation positions it as a key material in renewable energy applications, offering potential for clean hydrogen production that aligns with global efforts to transition toward carbon-neutral energy systems [63].

The catalyst chose titanium oxide as the main body of catalyst. The reasons are as followed: TiO_2 photocatalysts have emerged as a promising material for hydrogen generation, offering an environmentally friendly and renewable method of converting solar energy into chemical energy through water splitting [64]. However, TiO_2's wide bandgap (3.2 eV) restricts its ability to absorb visible light, limiting its efficiency under sunlight [65]. Consequently, various modification strategies have been developed to enhance TiO_2's photocatalytic performance, such as doping with metal (Pt [66], Pd [34], Fe [67], Cu [68], Ni [69]) and non-metal (N [70] [71], C [72]) elements. These modifications reduce the bandgap, extend absorption into the visible light range, and improve

\

charge separation, ultimately enhancing the hydrogen evolution reaction (HER) efficiency. Additionally, surface modifications, including the formation of heterojunctions by coupling TiO_2 with other semiconductors (e.g., g-C_3N_4 [73], CdS [74], Cu_2O [75]), further improve photocatalytic performance by facilitating charge transfer and enhancing catalytic activity. TiO_2 composites, such as TiO_2-graphene, have demonstrated remarkable hydrogen production rates, with some systems achieving hydrogen generation up to 2626.7 μmol/g/h under visible light. Despite these advancements, challenges remain, including low quantum efficiency due to rapid charge carrier recombination and limited stability under prolonged light exposure. To address these challenges, recent research has focused on developing more stable and efficient TiO_2-based composites. Future studies should aim to optimize synthesis methods, improve charge separation, and explore novel doping and surface modification techniques. TiO_2 photocatalysts continue to play a key role in the ongoing development of efficient, low-cost renewable energy technologies for hydrogen generation. Table 1 shows the examples of TiO_2 composites photocatalysis hydrogen generation. As shown in the Table 1, many metals/metal oxides can combine with TiO_2 to form efficient photocatalyst. Metal doped composite like Pt, Au, Cu, Rh, Co showed significant ability in electron transfer and surface field which improved the catalysis performance. The enhancement of photocatalytic hydrogen evolution by metal

\

cocatalysts like Pt, Au, and Cu is primarily attributed to their dual function as efficient electron sinks and reactive sites. The Schottky junction formed at the metal-semiconductor interface promotes the spatial separation of photogenerated charge carriers by rapidly extracting electrons, thereby mitigating recombination. Concurrently, these metals, particularly Pt, provide active sites with exceptionally low overpotentials for the hydrogen evolution reaction (HER), optimizing the adsorption-free energy of hydrogen intermediates and drastically improving surface reduction kinetics. While Pt remains the benchmark due to its superior electron affinity and HER activity, Au offers additional plasmonic effects, and Cu serves as a low-cost alternative, collectively enhancing the overall quantum efficiency. However, the precious metal will significantly increase the cost of composite, therefore, a cost efficient composite is needed for industrial application. Nickel-based catalysts is primarily attributed to their multifunctional role in facilitating charge separation and surface reaction kinetics, while offering significant economic advantages over noble metals. The fundamental mechanism involves the formation of a Schottky junction at the Ni/semiconductor interface, which promotes the efficient extraction and migration of photogenerated electrons from the semiconductor to the Ni nanoparticles, thereby suppressing charge carrier recombination. Concurrently, Ni nanoparticles provide abundant active sites for proton adsorption and reduction. Although the intrinsic

\

hydrogen evolution reaction (HER) activity of metallic Ni is lower than that of Pt, it can be drastically optimized through the *in-situ* generation of a Ni/NiO_x core-shell structure or the formation of Ni-based compounds (e.g., NiS, Ni_2P) [76] [77] [78] [79]. These modified phases exhibit more favorable hydrogen adsorption free energy (ΔG_H*), closer to the thermodynamic optimum, thereby significantly reducing the reaction overpotential and accelerating the surface redox kinetics. Furthermore, the oxidation state versatility of Ni allows it to participate in catalytic cycles, enhancing stability and activity. In essence, Ni-based cocatalysts serve as a highly effective, low-cost alternative that concurrently addresses the critical challenges of charge separation and surface reaction efficiency in photocatalytic hydrogen production systems.

Table 1 Description of the production of H_2 with various photo-catalyst and their key effects [4].

Photo-catalyst	**Concentration of dopants or cocatalyst**	**Light source**	**Q.E.**	**H_2 production (μmol/g/h)**	**Reference**
Rh/Nb-TiO_2	Rh (0.2 wt%)	300 W Xe	3%	7850	[80]

\

Cu/TiO_2	Nb (0.2 wt%)	UV (450 W Hg)	7.00%	8470	[81]
Cu/S-TiO_2	Cu (5 wt%) Nb (0.2 wt%)	500 W Xe lamp with U*V* cut-off filter	–	7500	[82]
Pt/Ga-TiO_2	Ga (3.125 wt%)Pt (0.5 wt%)	150 W Xe U*V* cut-off filter	–	5722	[83]
Ru-TiO_2	Ru (3 wt%) –	500 W Xe lamp with a light cut-off filter UV light (280–400 nm) 300 W Xe lamp	3.10% –	4700 3918	[84] [85]

\

Ni/TiO_2	1 wt%	UV (450 W Hg)	2.80%	3390	[86]
Fe^{3+}/TiO_2	Fe (0.1 mol %)	solar light irradiation of $\lambda \geq 320$ nm	–	2423	[87]
Cu-In_2O_3 NRs/TiO_2 NWs	–	35 W Car-HID lamps	–	2196	[88]
NiO/TiO_2	–	Solar	4.50%	1200	[89]
C-Ti/CN-10	MXeneTi_3C_2 (10 vol%)	300 W Xe lamp with	–	1409	[72]

2.4 Nickel based nano particles conventional synthesis method

The synthesis of pure Ni_2O_3 is severely constrained by its inherent thermodynamic instability. As a metastable compound, Ni_2O_3 readily decomposes into stable NiO and oxygen gas, especially at moderate temperatures, drastically narrowing the viable synthesis conditions. Furthermore, Ni_2O_3 is highly sensitive to atmospheric moisture and

carbon dioxide, often transforming into unwanted phases, necessitating complex oxygen- and moisture-free environments. Compounding these issues, the Ni^{3+} oxidation state is energetically unfavorable compared to Ni^{2+}, requiring very precise and strong oxidizing conditions during synthesis to achieve and maintain it, which often leads to side reactions or decomposition. Finally, common chemical synthesis routes (like precipitation or thermal decomposition of typical precursors) overwhelmingly favor the formation of NiO or mixed-valence compounds rather than pure Ni_2O_3 due to these stability challenges [90]. Research on the stable and well-understood NiO is highly beneficial for developing Ni_2O_3 synthesis methods due to several key connections. Firstly, both oxides share similar structural frameworks (e.g., rock-salt derived structures); insights into stabilizing NiO's lattice through defects, doping, or morphology control provide direct strategies for potentially stabilizing the metastable Ni_2O_3 structure and its Ni^{3+} ions. Secondly, techniques extensively refined for controlling NiO particle size, shape, and porosity (e.g., sol-gel, hydrothermal methods) offer a proven experimental blueprint that can be adapted for Ni_2O_3 synthesis under controlled oxidizing conditions. Crucially, NiO often acts as an intermediate phase during the oxidation to Ni_2O_3; studying this transformation pathway reveals optimal conditions (temperature, oxygen pressure, kinetics) for Ni_2O_3 formation versus decomposition. Additionally, using NiO's

properties as a benchmark helps evaluate Ni_2O_3 synthesis success and isolate the specific effects of the Ni^{3+} ions.

2.4.1 Solid-phase method

The solid phase method is a traditional and long-standing way of fabricating nanomaterials; it has advantages of low cost, solvent-free, high selectivity, and can be applied in industrial production at a relatively mild reaction environment. However, it has drawbacks such as limited accuracy, relatively low efficiency, and difficulty in controlling the particle characteristic properties [91]. Solid powders are normally used as precursors or reactants. Once homogeneously mixed, the input energy is required to initiate the reaction. Therefore, the high reaction temperature is usually indispensable for the solid-phase method. The microwave reaction system can be applied in solid-phase method, microwave can uniformly radiate to each part of reactants, it can cause the rotation, vibration, and swing of particles, therefore, increasing the efficiency of particles collision, and shortening the reaction time. As shown in figure 2-3, the solid reactants are grinded into powders, then mixed through vibration or rotation, and the heat treatment via calcination is applied to facilitate the pyrolytic reaction before the nanparticles can be synthesized.

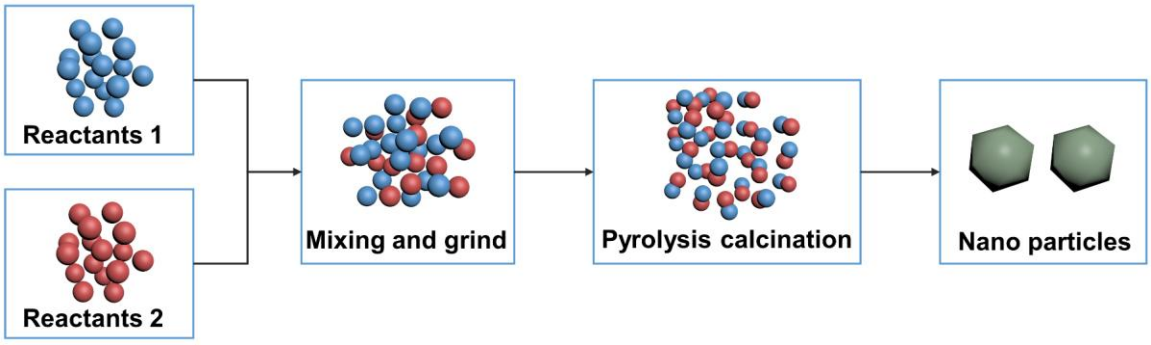

Figure 2-3 The scheme of the solid-phase method using calcination

Xia et al. [92] used nickel nitrate and oxalic acid as reactants with heat treatment at the temperature of 400˚C for four hours. Wang et al. [93] used $Ni(OAc)_2 \cdot 4H_2O$ and Tween 80 as the precursor, grinded them into the powder, and then applied the heat treatment by the calcination at 400˚C for 2 hours and drying the samples for four hours under 80 ˚C. NiO nanoparticles with a well mesoporous structure were synthesized, as shown in Figure 2-4. Hosny et al. [94] produced 8-nm nanoparticles through a semi-solid phase reaction with a 700 ˚C decomposition process.

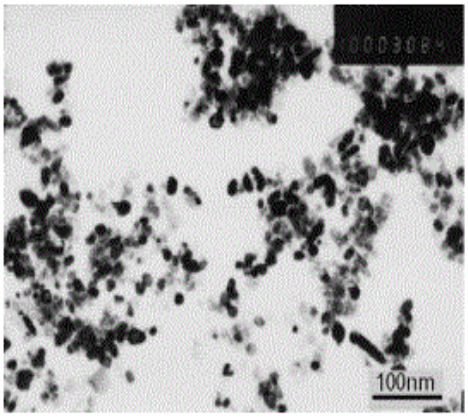

\

Figure 2-4 The TEM of NiO nanoparticle samples synthesized by solid-phase method, reproduced with permission [78] from Elsevier.

2.4.2 Liquid phase method

The liquid phase method can be classified into several subtypes, such as direct precipitation method, homogeneous precipitation method, sol-gel method, hydrothermal method, microemulsion method, organic complex precursor method, biosynthesis method and polymer-network gel method, according to the different liquid medias that have been used. The liquid phase method mostly uses metallic sault solution to separate the metal element into ions. The heat treatment, hydrolysis, or other processes can be applied to obtain the material precipitation or crystal, and dehydration will turn the precipitation into the target powders [91]. The NiO nanoparticles fabricated by the liquid-phase method normally feature with relatively uniform distribution of particle size, thus high monodispersed, thus this method has been most widely used nowadays, owing to the controllable reaction conditions [95]. The representative samples fabricated by each type of liquid phase method is shown in Figure 2-5.

\

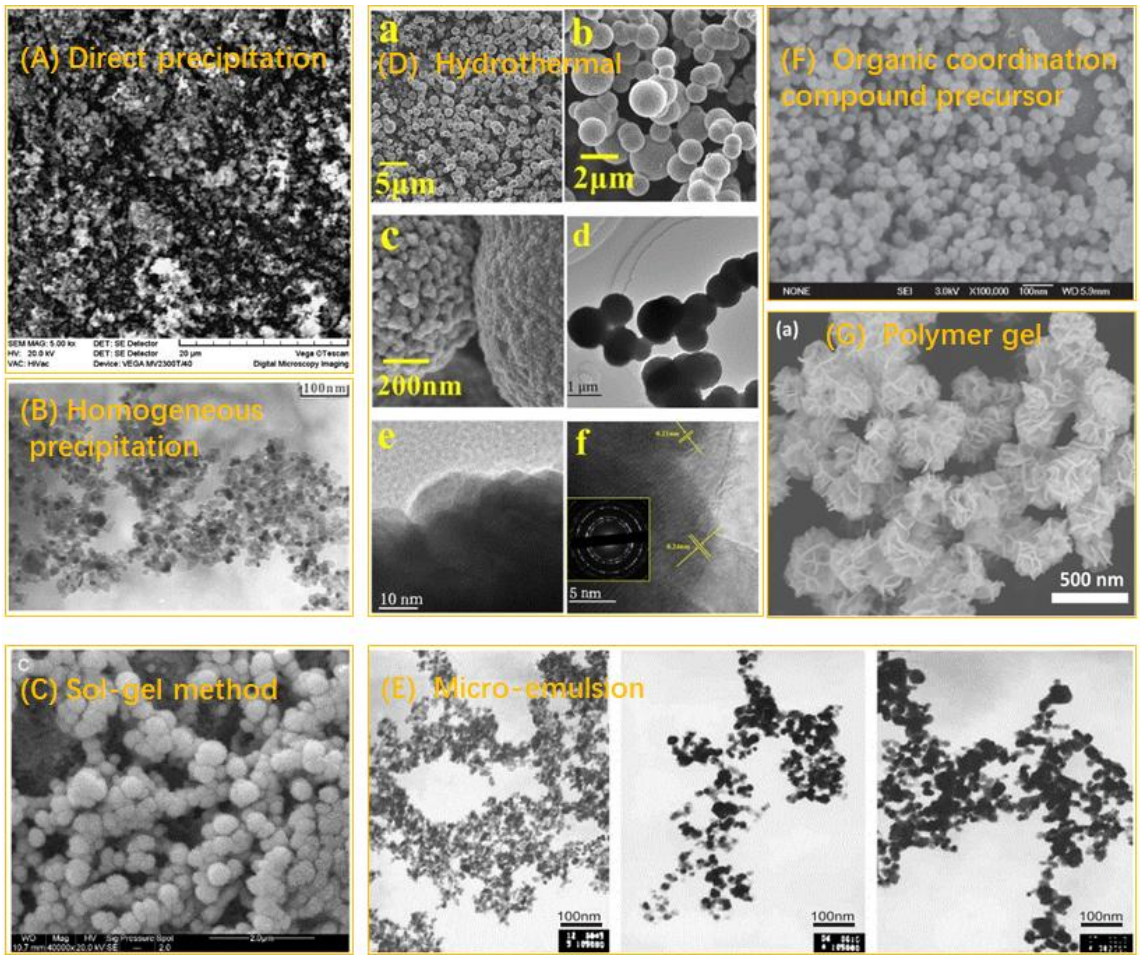

Figure 2-5 (A) Scanning electron micrographs (SEM) images of powders synthesized by direct precipitation method.

(N.B. Reproduced with permission [96] from Elsevier. (B) TEM image of NiO nanoparticles synthesized by homogeneous precipitation. Reproduced with permission [97] from Elsevier. (C) SEM images of sol-gel product. Reproduced by permission [98] from Elsevier. (D) SEM (a, b, c) and TEM (d, e, f) images of particles synthesized by the hydrothermal method. Reproduced with permission(Cao et al. [99] from Elsevier. (E) TEM image of NiO nanoparticles synthesized by the micro-emulsion method. Reproduced with permission (Han et al. [100]

from Elsevier. (F) SEM image of NiO nanoparticles at high magnification [101]. Reproduced with permission [101] from Elsevier. (G) SEM images of NiO nanoflowers synthesized by polymer gel method. Reproduced with permission [102] from Elsevier.)

Direct precipitation method

The direct precipitation method has been widely adopted in fabricating ultrafine particles. This method uses a chemical reaction to precipitate intact wedges. Then precipitation will turn into nano powders through purification, grinding, and heat treatment process [95]. Bahadur et al. [96] used sodium hydroxide (NaOH) and nickel nitrate ($Ni(NO_3)_2$) as the precursor, reacting and leading to formation of a wet cake of nanocrystalline NiO, which was subsequently dried and grinded into powders. The grinding process gives rise to big variations in the particle dimension, and distribution of density, thus lacking physical integrality.

Homogeneous precipitation method

The homogeneous precipitation method adopts a principle similar to that of the direct precipitation method; it also used the chemical reaction to produce solid precipitation. However, it keeps the precipitation in solution at a balance condition and makes the precipitate at a uniform speed (Pan et al. [103]. It is attained through controlling the concentration of the precipitant. Therefore, this method is stable, balanced, and able to fabricate high-quality particles. Deng et al. [97] fabricated the NiO nano

\

powders with the purity of 99.73%, cube structure, and averaged size of 9 nm through homogeneous precipitation. Despite the high-quality nano powders they have synthesized, they used $NiCl_2 \cdot 6H_2O$ solution and $NH_3 \cdot H_2O$ as pre-reactants. The ammoniate products will pollute the environment, so this method needs an extra purification process.

Sol-gel method

This method uses high-chemical activity substances as a precursor, through hydrolyze, aldolization, condensation, and other chemical reactions to get stable sol with relative uniform distribution of the nanoparticles(Kumar et al.[104, 105]. Then heat treatment was utilized to obtain metal nanoparticles. The final particles can reach atom level and possess a very small grain diameter. Thota et al.[98] adopted nickel acetate tetrahydrate and oxalic acid as reactants, ethyl alcohol as a solute, undergoing 400 ˚C calcination. The black powders of NiO nanoparticles were fabricated by Pooyandeh et al. [106] using the sol-gel methods with nickel nitrate hexahydrate and nickel chloride hexahydrate as the precursor, and magnetic stirring was applied in the fabricate process, after quiescence for a short time, the solution was filtrated to form the NiO nanoparticles.

Hydrothermal method

The hydrothermal method refers to the nanoparticle fabrication process in which a solution was sealed in a high-pressure vessel with the chemical reaction occurring at high pressure and temperature condition,

reactants will undergo dissolving, recrystallization, and heat treatment to form the final products [107]. Figure 2-6 shows the typical synthesis mechanisms and procedures of hydrothermal method, the chemical reactions take place in a solution to trigger the formation of the nanoparticles, followed by the heat treatment to remove wastes and obtain the purified products. It has the advantages such as intact development of grain, relative uniform distribution of particle diameter, less aggregation of particles, obviation of calcination at high temperature in the final process, and in particular it is a cost-effective and facile synthesis process. However, it is more time-consuming than most other methods. Adschiri et al. applied the continuous hydrothermal method for synthesis of 10 various metal oxide nanomaterials including NiO nanoparticles, by using a microreactor with inner diameter of microchannel to be 9.5mm. They synthesized NiO nanomaterial with an average size of 200 nm in 2 minutes[108]. Cao et al.[99] successfully fabricated three hierarchical NiO microspheres through the hydrothermal method. The molar ratio of 1,2-Propanediol and water were kept at 1:1 in the solution. Nickel nitrate ($Ni(NO_3)_2 \cdot 6H_2O$), urea($CO(NH_2)_2$, and citric acid were chosen as reactants and the ratio was kept at 2:1:1. NiO microspheres were self-assembled and grew in a uniform condition. Nickel nitrate and NH_2CONH_2 are also widely used reactants in the hydrothermal method. An accurate calculation is needed to determine the ratio between each reactant.

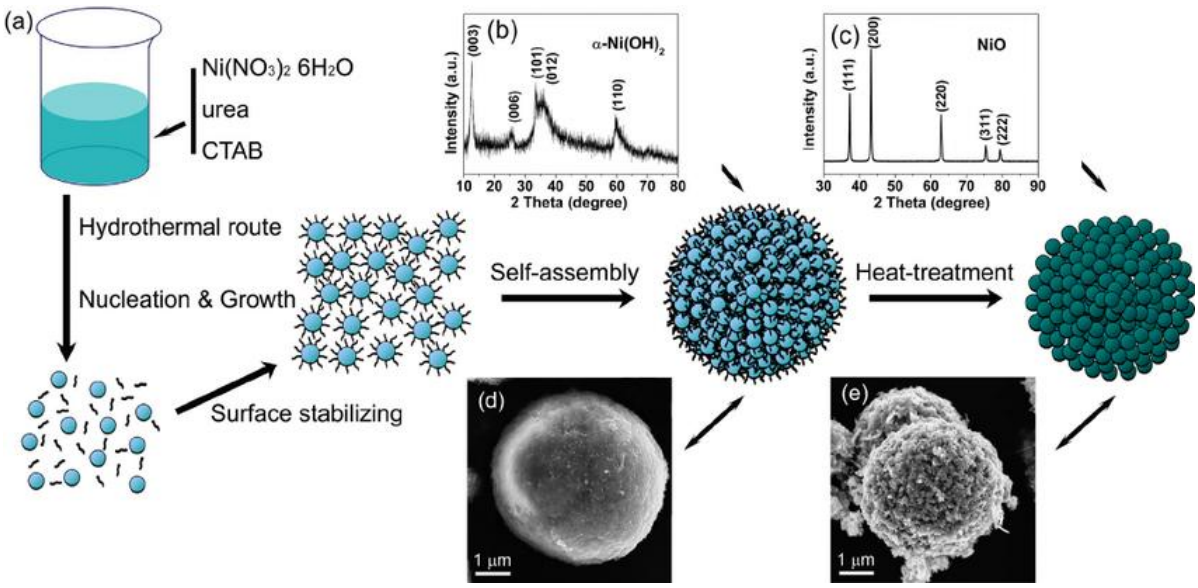

Figure 2-6 Scheme of hydrothermal decomposition method for producing the NiO nanoparticles. Reproduced with permission [109] from Elsevier.

Microemulsion method

This method works through two insoluble solvents, for example, oil/water system, to form an emulsion in the presence of a surfactant, or cosurfactants, which can decrease the water/oil surface tension to 1-10 mN m^{-1}, facilitating the formation of emulsions [110]. Meanwhile, surfactants and cosurfactants will create a transient interfacial tension to prevent the droplets from coalescence [111]. The formation of microemulsions normally needs centrifugation or magnetic stirring to accelerate the dispersion process. For example, Han et al. [100] used cyclohexane as oil phase, Triton X100 as surfactants, and hexyl alcohol as cosurfactants, which were mixed at a ratio of 5:3:2 with the aid of magnetic force to form emulsions effectively.

\

Fabricating nanoparticles through microemulsion methods has multiple advantages, such as relatively simple experiment setup, low energy cost, and facile operation. Moreover, the range of particle diameter distribution is relatively narrow, and the particle diameter can be efficiently controlled; secondly, choosing appropriately different surfactants and co-surfactants can lead to the formation of nanoparticles with a special property [110], and the particles will have less aggregation. They are stable due to the presence of surfactants and co-surfactants.

Organic coordination compound precursor method

This method used coordination compounds which are the substances with central metal atoms surrounded by nonmetal atoms [112], and are easy to be removed by pyrolytic reactions as a dispersing agent, then mixed with a metal ion to activate the coordination reaction. During the reaction, the dispersing agent will separate particles and prevent them from agglomeration. The reaction will lead to the fabrication of a highly dispersed precursor, which undergoes heat treatment to produce the target particles. Tao et al. [101] selected polymer as a dispersing agent, nickel acetate as reactants, which were mixed to form the precursor at a raised environment temperature of 373K. NiO nanoparticles were fabricated when the temperature was further raised to 673K with homogeneous size distribution of around 30 nm as shown in Figure 2-5(F).

Polymer-network gel method

\

The polymer network gel method can successfully fabricate the relatively pure phase of NiO particles with a uniform distribution of particle diameter and facile control over the shape of the crystalline grain. The formation of a macromolecular chain will make metal sault ion evenly distributed in the sol-gel. Drying and calcining the sol-gel will lead to the fabrication of the nanoparticles. Zhao et al. [113] adopted acrylamide free radical polymerization and N, N '-methylene diacylamine bifunctional group by using nickel nitrate aqueous solution as raw material, water-soluble propylene Amide monomer and N, N '-methylene diacylamine as network agents, ammonium sulfate as initiator, finally obtaining NiO particles with size ranging in 15 ~ 20 nm. Munkaila et al. [102] synthesized NiO nanoflower using amphiphilic block copolymer as reactants in one-pot synthesis method. The NiO nanoflowers with mesoporous structure were successfully fabricated, as shown in Figure 2-5(G).

Biosynthesis method

The biosynthesis techniques are very effective in synthesizing metal oxide nanoparticles. It has drawn much attention as it is both environmentally and economically friendly, it does not require complex operation, and it is innoxious to cell and other biosystems. It uses the small natural molecules in biosystems in combination with the conventional synthesis methods (mainly liquid phase method) to fabricate nanoparticles and has been proved to have better quality and

productivity compared to the conventional methods [114, 115]. Figure 2-7 shows the basic principle of the biosynthesis method. The extract substance of plant can be incorporated in the synthesis process of the nanoparticles. Its pH value, concentration, reaction time, and temperature will directly influence the quality of final products. Sabour et al. [116] applied the biosynthesis method, using Rheum Turkestanicum plant extractions, and successfully fabricated CeO_2 nanoparticles with average diameter of 30 nm. Similarly, Najjar et al. [117] used gelatin as stabilizing agent, and sol-gel method to successfully synthesize SnO_2 nanoparticles with an average diameter of 27 nm.

Sabouri et al. used tragacanth as stabilizing agents via the co-precipitation method to synthesize nanosheets with comparable high quality and low toxicity to cells. Its absorption efficiency of anionic dyes and cationic dyes reaches 82% and 60%, respectively [118]. The same group also combined the bio-method with the sol-gel method. They successfully synthesized NiO nanoparticles with an average diameter of 59 nm. They used Arabic gum as stabilizing agent, nickel nitrate ($Ni(NO_3)_2 \cdot 6H_2O$) as reactants, forming an aerogel at 80°C, enabling the formation of NiO nanoparticles via the biology activities [119]. Therefore, biosynthesis method paves a promising way to synthesize NiO nanoparticles in future.

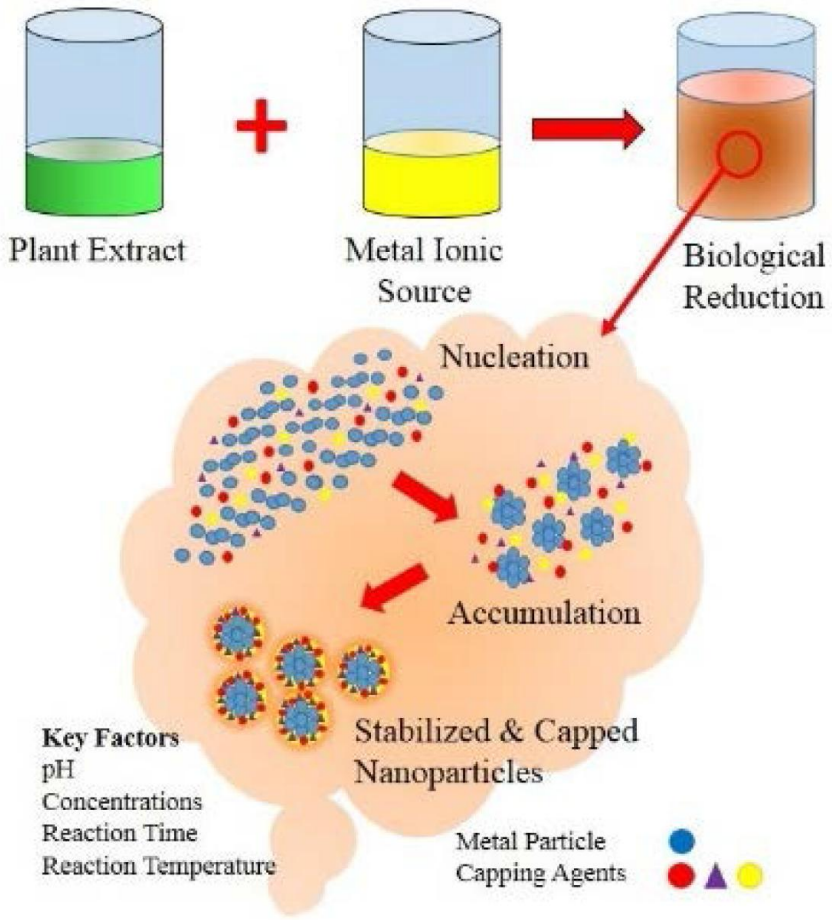

Figure 2-7 The diagram of biosynthesis principles for forming the metal oxide nanoparticles. Reproduced with permission of [120] from MDPI.

2.4.3 Vapor phase method

The vapor phase method uses high pressure and temperature vapor to carry the precursor and use its energy to finish the reaction. The most used vapor phase method is spray pyrolysis, which applies the high temperature and pressure at the nozzle to stimulate the pyrolytic reaction, and the precipitation reaction occurs simultaneously [121]. As the metal

\

salt solution sprays out from the nozzle, it will instantly turn into vapor and separate into nanoparticles. Due to the rapid solution evaporation and release of vapor, it is hard to control the particle characteristics such as crystalline shape, particle diameter, and phase purity using this method. However, as it possesses the advantages of a large production rate and facile operation, it has wide industrial production potential [95]. Figure 2-8 shows the different stages of the process. Mixture of air and fuel will provide an environment with high temperature and high pressure, the precursors are sprayed into droplets prior to the taking place of the pyrolytic reaction and evaporation process. Precursor droplets will start to nucleate and grow to form nanoparticles.

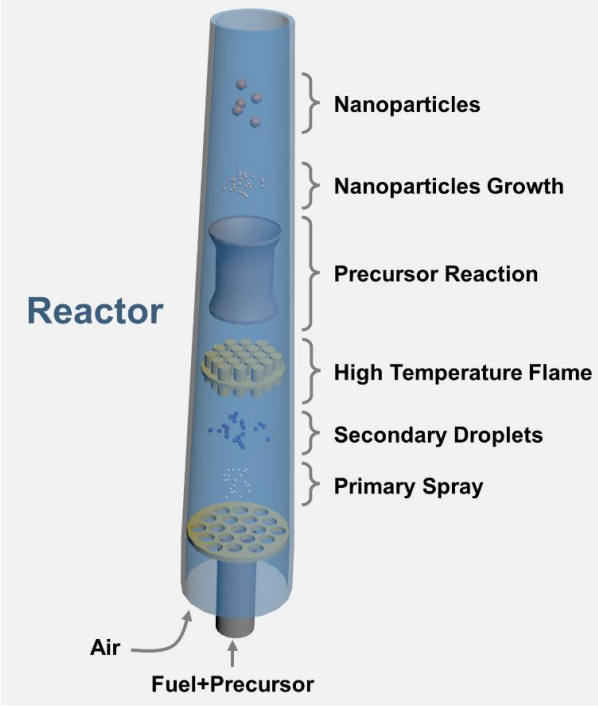

Figure 2-8 The different stages during the synthesis process of nanoparticles using the vapor phase method.

\

Lenggoro et al. [121] used low-pressure spray pyrolysis and successfully synthesized the NiO nanoparticles with an average size of 20 nm. The conversion process and results under different condition are shown in Figure 2-9. The solution contains precursor driven by pump going through the channels and is spurted at the nozzle, the solubility of precursor decides the final type of particles. High solubility precursor produces nano particles, low solubility precursor become sub micro particles. Oh et al. [122] synthesized hollow spherical nanoparticles with uniform distribution of particle diameter of around 20 nm, and well-dispersed nanocrystalline structures. Moravec et al. [123] fabricated NiO nano particles with average diameter about 50nm by pyrolysis and reduction reaction through 1.5cm inner diameter nozzle. They proved the production rate include particle size and particle size distribution increase with the increasing of saturation temperature.

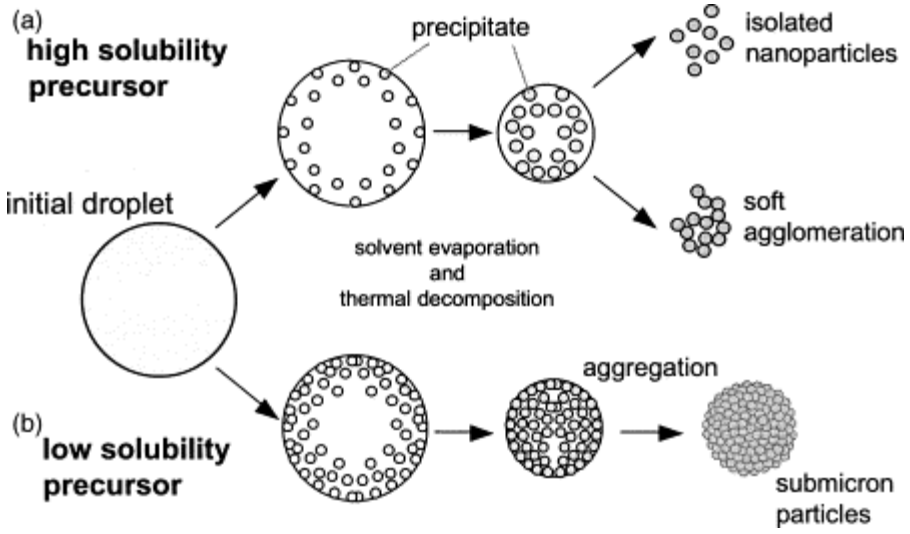

\

Figure 2-9 Conversion process from droplet to particles of low pressure spray pyrolysis. Reproduced with permission [121] from Elsevier.

2.4.4 The advantages and limitations of conventional methods

Each method has its own advantages and challenges, as summarized in Table 2. The liquid phase method is the most widely used method in industrial production and lab-scale synthesis. The size of nanoparticles is more uniform and controllable than the solid phase and vapor phase method. The solid-phase method widely uses pyrolysis or microwave, and it is convenient to operate, it has low requirements on the reaction environment and low cost, the produced particles have a relatively uniform distribution of diameter. However, its quality is relative hard to control and always accompanied by agglomeration. The vapor phase method has great potential in industrial manufacture, and it has great efficiency with relatively facile operation. However, it has relatively high requirements on the reaction environment, and complexity of the devices.

Table 2 Summary of merits and limitations of conventional NiO synthesis methods

Fabrication methods	Average particle size (nm)	Effective temperature (Degree Celsius)	Synthesis duration (hours)	Merits	Limitations	References
Solid phase method	8	700	4.3	Low cost, facile operation, no solvent, high	Large energy consumption, low efficiency,	[124]

	10	400	6.5	selectivity, high yield	vulnerable to oxidation deformation	[93]
Direct precipitation method	9	300	13	Acceptable cost with relative high purity of product, good stoichiometry.	Low power density with poor physical integrity	[125]
Homogeneous precipitation method	9	400	3.5	Low cost, facile operation, stable reaction, and high quality of product	Stringent requirements on reaction environment and post-processing including centrifugal deposition, mixed crystal co-precipitation, and extra purification process	[103]
Sol-gel method	19	400	> 28	Facile operation. uniform particle size distribution, and high chemical activity	Relatively high cost with accurate control over solution concentration, sol-gel temperature, and heat treatment temperature.	[106]
	4-22	500	28			[105]

\

Hydrothermal method	15-20	400	16.6	Particle diameter is small with monodispersed distribution, less agglomeration.	Requirement of stringent control over solution concentration, reaction duration and temperature	[107]
Micro-emulsion method	3-15	450	25.5	Monodispersed particle size distribution,	Requirement of surfactants and co-surfactants, relatively high cost.	[126]
Organic complex precursor method	Around 30	400	-	Uniform particle size distribution with good dispersion performance.	High cost and requirements on material and chemicals.	[101]
Polymer-network gel method	Mostly < 40	500	31	High purity of products, good control over the particle size	High cost and low operation accuracy	[127]
	Mostly 210	350	>15			[102]
Vapor phase method	Around 20	900	<1	High productivity with high potential in industrial scale production, fast reaction process	Difficulty in controlling the morphology of solid particles, stringent requirements on instrument and devices.	[121]
	14	400	About 20			[122]

\

Biosynthesis method	59	500	18	Low biotoxicity, applicable in cell and bio-engineering, facile operation and experiment process.	Relatively high cost with accurate control over solution concentration, reaction duration, reaction temperature, the substance from plant extraction may pollute the reaction environment.	[119]

2.4.5 Microfluidic synthesis of nano particles

The nanomaterial formation process can be achieved using a microfluidic platform with accurate control and monitor over the nucleation and growth of nanoparticles [128]. Moreover, the nano particles synthesized by microfluidic applications have been proved to have enhanced physical properties than the particles synthesized by conventional method. For example, average particle size distribution, more accurate size control and better loading efficiency [129]. Zhang et al.[130] provided an overview on mixing, flow dynamics, and mass and heat transfer in microreactors along with three strategies for scaling up microreactors: parallel numbering-up, consecutive numbering-up, and scale-out. They also proposed a possible methodology to design microchemical systems. Wang et al. [131] had developed a new

\

strategy for scaling-up of a micro sieve dispersion reactor. Deposition methods can be applied to create a thin coating on the particles surface and form a layered structure [132], it has been widely used in food [133], medicine [134], textiles [135], materials [136] and environmental protection. Zhao et al.[137] successfully used a microfluidic interfacial synthetic method to fabricate covalent organic polymer microcapsules, and it has been widely used in wastewater treatment and environmental protection.

Microfluidics can produce particles with high purity, complex structures and a highly evenly distribution of particle sizes. Lian et al.[138] successfully applied microfluidics in fabricating TiO_2 nanoparticles through surfactant wrapping sol-gel method, with TiO_2 nanoparticles evenly distributed on the outer surface of the multiple wall carbon nanotubes (MWCNTs), and it has the ability to absorb Rhodamine B for wastewater treatment. Du et al.[139] fabricated Sio_2 nanoparticles using membrane microreactor, they suggested a gas-liquid precipitation reaction system which can guarantee the quality meanwhile saving the cost. The same group improved the synthesized process of $BaSO_4$ by adding microbubbles created by the microreactor[140]. $CaCO_3$ nanoparticles were fabricated by Wang et al.[141] via integration of a microstructure reactor and the microfluidics to enhance mass transfer in the mixing process. It is feasible to apply microfluidic technology in the synthesis process of NiO nanoparticles. Most nanomaterial growth

processes involve three steps: nucleation, growth, and aging. As shown in figure 2-10, the microfluidic system enables accurate control over the flow conditions of different phases which are pumped into the microchannels, and the synthesis of nanomaterials can be achieved in the microreactors, with yielded products adopting different forms such as sphere-shaped, non-sphere-shaped particles and capsules, and fibers. The microfluidic platform provides a powerful mixing ability that can significantly stimulate the nucleation process. Besides, the stable fluid flow environment is suitable for the growth of large size particles and the formation of complex-shaped particles [142].

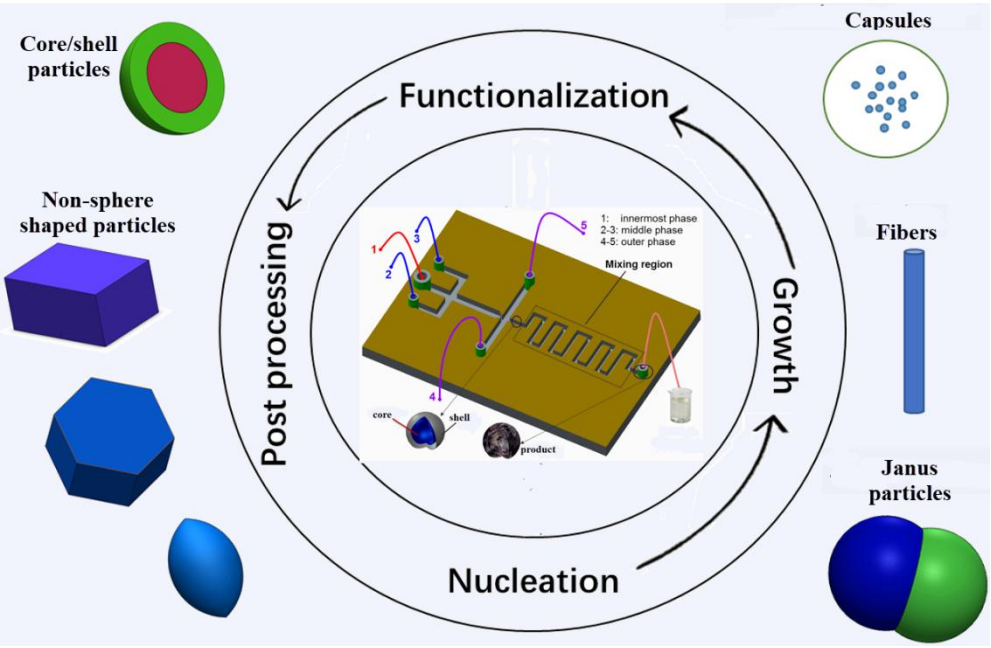

Figure 2-10 Nanomaterial synthesis process based on microfluidic technology

2.4.6 Microfluidic synthesis of nickel based materials

\

Liang et al.[143] developed a continuous mode microfluidic reactor, which can effectively enhance heat transfer and mixing. They successfully synthesized $Ni_{0.6}Mn_{0.2}Co_{0.2}CO_3$ with uniform particle size distribution, good thermal stability, and homogeneous transition metal distribution. As the NiO nanoparticle fabrication process normally involves high pressure, either the number of channels could be increased, the channel cross-section could be enlarged, or the flow rate in the channels could be increased to cope with a high mass flow rate [144]. Kawasaki et al.[145] used a T-shaped micromixer and successfully applied a continuous supercritical hydrothermal method to synthesize NiO nanoparticles with size of 20-50 nm. Meanwhile, when they decreased the tube diameter from 2.3 mm to 0.3 mm, the size of NiO nanoparticles changed from 54.3 nm to 20.1 nm. Sue et al. used a central collision type micromixer for synthesis of Fe_2O_3 and NiO nanoparticles. They investigated the effects of the key factors such as residence time and temperature in the synthesis process. They used $Fe(NO)_3$ and $Ni(NO)_2$ as reactants in the continuous hydrothermal method and successfully fabricated nickel ferrite with a diameter less than 5nm [146]. They also used a 0.3 mm T-shape micromixer to successfully fabricate NiO nanoparticles with an average diameter of 16 nm. They used preheated water flow in the T-shape tube to provide the energy for the hydrothermal reaction shown in figure 2-11 [147]. Kiwamu et al. [148]

\

invented a new type of micromixer for synthesis of nanoparticles. As shown in figure 2-11B, they adopted a T-shaped micromixer with the tube inner diameter to be 0.18 mm. The completed flow system consists of the pumps, reactor and other devices. The micromixer was positioned at upstream of the reactor, the powerful mixing ability of the microfluidic mixer provided the highly uniform mixture solution. With hydrothermal reaction, they used this new mixer to achieve the fabrication of NiO nanoparticles with size of 18.2 nm and 23.5 nm, respectively. Kawasaki et al (2010) developed a new swirl micromixer for synthesis of NiO nanoparticles. Compared to a conventional T-shaped mixer, the average diameter of particles has been reduced from 47 nm to 20 nm with monodispersed size distribution. Moreover, computational fluid dynamic simulation results suggested that the swirl mixer can enable rapid and homogeneous mixing of fluids, therefore producing high-quality nanoparticles. Zhao et al. [149] constructed various NiO nanoarrays through Y-shaped needles, and they used a pump to drive the solution flow through the needles then reactions happened in microtubes to form nanosheets with a thickness of about 40 nm, they used the nanosheets to modify microchannels to enhance its ability to absorb protein. Yoko et al. (2020) applied a T-shaped micromixer system to investigate the correlation between the mass transfer rate and Reynolds number and the kinetics under reaction control conditions, and evaluated the reaction kinetics of synthesis for the nickel nitrate to nickel oxide reaction that took

\

place in a wide range of temperatures and pressures around the critical point of water. Michalska et al. (2021) deposited high-quality NiO film with thickness of 30 nm using a Tesla-valve micromixer. The key synthesis conditions for NiO nanomaterial formation using microfluidic reactors are summarized in Tab. 2 which demonstrates that the morphology and size of NiO nanomaterials can be well tuned via control over the flow rate and the dimensions of the microreactor systems.

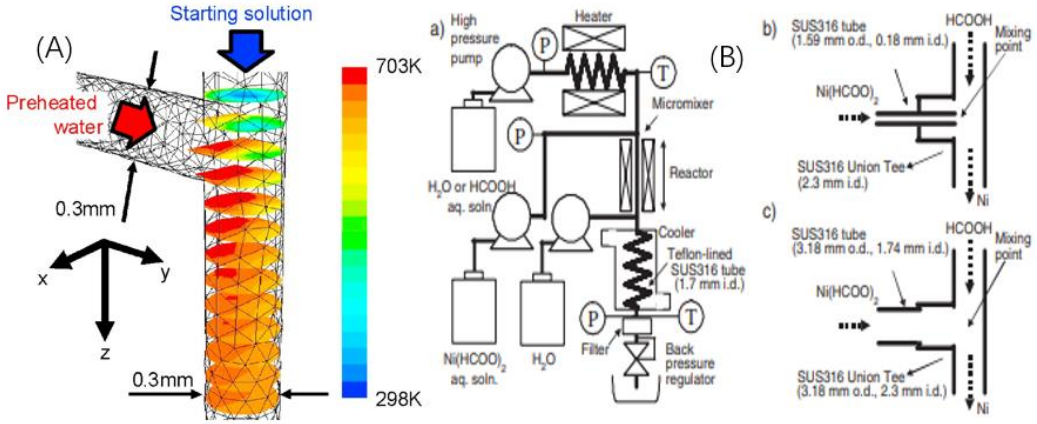

Figure 2-11 (A)Temperature contour of T-shape mixer. Reproduced with permission of.[147] from Elsevier. (B) (a) Schematic diagram of reaction flow system (b) Newly designed T-shape mixer (c) Conventional T-shape mixer. Reproduced permission of [148] from Springer.

Table 3 The summary of key synthesis conditions for NiO nanomaterial formation using microfluidic reactors

\

Shape of NiO nanomaterials	Size of NiO nanomaterials	Flow rate	Channel size of microreactors	Flow residence time	References
Nanoplate	20.1-54.3 nm in thickness	30 mL/min	0.57mm	1.3-2.7 s	[68]
Spherical nanoparticle	4-6 nm in diameter	/	Eggshell membrane reactor with 70 μm in thickness.	~8 hours	[83]
Nanofilm	30 nm in thickness	50-100 μL one time	1-3 μm	<10 s	[146]
Array	40 nm in thickness	25 μL/min	530 μm	400 min	[144]
Spherical nanoparticle	10-40 nm in diameter	38.7 g/min	0.3 mm	<1 s	[147]

In summary, microfluidics has the intrinsic superior ability in enhancing mixing, heat, and mass transfer and provides a stable chemical reaction environment, giving rise to these advantages as follows:

(1) Microfluidics enables high mixing efficiency even in laminar flow at low Reynolds number. It can accelerate the formation of precursor and shorten the reaction time significantly. Meanwhile, a microfluidic mixer, either in a passive or active way, can rapidly lead to homogeneous mixing of reactants, hence enhancing the quality of the final products.

\

(2) Stable flow environment can facilitate the reaction with very stable conditions. A Microfluid reactor with a uniform fluid flow can provide a very stable chemical environment, which is suitable for NiO nanoparticle synthesis.

(3) Improved heat transfer ability can decrease the energy loss and make the reaction take place rapidly, most synthesis methods of NiO nanoparticles need heat treatment, microfluidic reactor accelerates the process of heat transfer and facilitates the nucleation and growth of nanoparticles.

The detailed comparison between conventional synthesis methods and microfluidic synthesis methods has been shown in Table 4.

Table 4 Summary of the advantages and disadvantages of conventional method and microfluidic methods

	Conventional methods	Microfluidic methods
Reaction time	Relatively long: a few hours for mixing reactants to fabricate precursors; and several hours for the nanomaterial formation process.	Significantly reduced reaction time due to the enhanced heat and mass transfer and rapid homogeneous mixing capability.
Device requirements	Most solid and liquid phase methods have low requirements on devices. The Vapour phase method has relatively higher requirements on devices.	High requirements on the size of the microtube or microchannels in the microreactor.

\

Flow conditions	Mostly batch mode multiphase flow environment. For example, sol-gel method needs the samples to be transferred and dried for a long time, therefore it is not appropriate to be applied into continuous synthesis. Only a few conventional methods such as spray pyrolysis and supercritical hydrothermal methods enables continuous NiO synthesis.	Mostly dynamic multiphase flow environment in the mixing process and the reaction process, therefore microfluidics is competent for continuous mode formation of NiO nanomaterials.
Production rate	The vapor phase method has a relatively high production rate. Most liquid and solid phase methods have a relatively limited production rate.	Easy to scale up by continuous synthesis in parallel mode
Material restrictions	A wide range of reactants in solid phase, liquid phase and vapor phase can be applied.	Suitable for liquid phase reactants with relatively low viscosity.
Nanoparticle size uniformity and product material property discrepancy	More challenging to control the particle size distribution, relatively high property discrepancy from batch to batch.	The precise control over the flow conditions and more uniform pressure and temperature distribution in confined reaction domain gives rise to high particle size monodispersed and low property discrepancy.
Reactant consumption	Relatively high.	Low reactant consumption as the reaction occurs in the micro-scale with high reaction efficiency.

Owing to the exquisite control over the particle diameter, shape, and other properties in a tunable way, microfluidic systems have been demonstrated to be useful platforms for synthesizing nanoparticles of organic polymers, oxides, semiconductors, and metals as well as hybrid structures combining multiple materials and functionalities. Despite the rapid development of microfluidic technologies for nanomaterial synthesis, the novel approach still faces some challenges. First, it is important to identify and understand the mechanisms of channel

clogging, such as constriction by deposition and accumulation on the walls or particle agglomeration, which remains challenging during the material synthesis process via the microfluidic approach [20]. The microdevices will have to be cleaned thoroughly or even completely replaced by a new one. The surface modifications and flow modulation can potentially address these issues. For example, the contact between reactants and microreactor wall can be minimized using droplet flow or applying special coating on the reactor wall can efficiently isolate control the particle agglomeration [150]. Mitigation of the clogging in microchannels can also be achieved using pulsatile driven flow instead of static flow and this will significantly delay the formation of clogging [151]. Second, the throughput of microfluidic approach remains far from meeting the practical industrial demands. This challenge can be addressed by scale-up approach via increasing the number of devices running in a parallel mode [152], however parallel model require relative large space and driven energy, which may cause other problems. It is assumed as one of the methods to fix the low output problem. Third, the design of microfluidic chips requires substantial efforts to explore the optimal parameters, such as the number of microchambers and channel size (length, width, height) [153]. Therefore, the development of microfluidic technology for nanomaterial synthesis requires more in-depth investigations and multidisciplinary integration of material science and fluid mechanics.

\

2.5 Conclusion

Micro-emulsion method has been decided as the best nanoparticles synthesized method for applying in the centrifugal microfluidic synthesis platform (microfluidic chip), as the method has the advantages of rapid reaction speed, relative low requirements of environment and devices, mainly 2 or 3 liquid reaction substances which are easy to be applied in the microchannel. The microfluidic system can satisfy the needs of unform reactants solution, rapid mixing efficiency etc. For the composite structure designed, Ni_2O_3 has very limited literatures, adding Ni_2O_3 as co-catalyst in the composite could significantly improve the light absorption and improve the electron transfer efficiency and direction. In the photocatalysis hydrogen generation area, precious metal (Pt, Au) is widely included to enhance the charge separation and modify electron transfer path, however, it will significantly increase the cost of catalyst. In order to decrease the cost and created a economic friendly with low carbon emissions composite. Ni_2O_3 and TiO_2 were selected. The designed z-type heterojunction increase the electron exist time and decrease the recombination of electrons and holes. Moreover, the influence created by different valence of Ni atom could also benefit the catalysis performance.

\

3 Chapter 3. Methodology

3.1 Experimental Chemicals

3.1.1 Centrifugal microfluidic synthesis of nanoparticles.

All chemicals are purchased from Aladdin Company, China and belonged to analytical grade with no further purification. Nickel nitrate hexahydrate ($Ni(NO_3)_2•6H_2O$), Sodium hypochlorite with four percent active chlorine (NaClO), Sodium hydroxide (NaOH). Sodium hexametaphosphate ($(NaPo_3)_6$)

3.1.2 Photocatalytic application of TiO_2- Ni_2O_3/CNT heterojunctions

All chemicals are purchased from Aladdin Company, China and belonged to analytical grade with no further purification. Chemicals include MWCNT, nickel nitrate hexahydrate ($Ni(NO_3)_2•6H_2O$), Sodium hypochlorite with four percent active chlorine (NaClO), Sodium hydroxide (NaOH),Titanium oxide nanoparticles, Triethanolamine ($C_6H_{15}NO_3$), Nitric acid (HNO_3), Sulfuric acid (H_2SO_4), Potassium permanganate ($KMnO_4$), Hydrogen peroxide(H_2O_2), Sodium Nitrate ($NaNO_3$) and Hydrogen chloride (HCl).

3.1.3 Hydrogen evolution reaction of core-shell Ni/NiO/Ni_2O_3/TiO_2-CNT heterojunctions

The chemicals for chapter 6 are same as the chemicals in chapter 5 except the H_2(10%)/Ar mix gas.

\

3.2 Experimental methods

3.2.1 Centrifugal microfluidic synthesis procedure

For a typical experiment, 0.8g $Ni(NO_3)_2 \bullet 6H_2O$ was dissolved in 15ml deionized water, mark the solution as solution A. For another beaker, dissolved 1.6g NaOH in 20ml NaClO solution with 5% active chlorine, mark the solution as solution B. Transport these two solutions into two different injectors. Push the injectors and inject the solution A and solution B into the opposite two chambers (shown in blue group and red group in figure 3.1) from four inject holes on the top surface. Use eight screws at the edge of microfluidic chip to fix the microfluidic on the centrifugal platform. Start the centrifuge machine to see two solutions quickly formed black particles and collected by the lower chamber. After five minutes, turn off the machine, and open the microfluidic chip to collect the solution consists precipitation. Pour the solution on the funnel covered by filter paper, wait until the liquid all goes to the lower collect beaker, then the produced black precipitate ($Ni_2O_{3*}xH_2O$) was further washed several times by 20ml NaClO solution and 200ml deionized water. After filtration, the final dark black precipitate was put into a 90℃ air blowing thermostatic oven for 12 hours. Then move into an agate mortar and grind for five minutes manually to get uniform powder which is Ni_2O_3 nano particles powder. Then collected the powders. One cycle of experiments will produce about 0.2g Ni_2O_3 nano particles powder. For comparison between

conventional synthesis method and microfluidic synthesis method, the quantity of product is same and the conventional synthesis processes are as follows: A solution was prepared by dissolving 0.8 g of nickel(II) nitrate hexahydrate ($Ni(NO_3)_2 \cdot 6H_2O$) in 15 mL of deionized water. Separately, 1.6 g of sodium hydroxide (NaOH) was dissolved in 20 mL of a sodium hypochlorite (NaClO) solution containing 5% active chlorine.

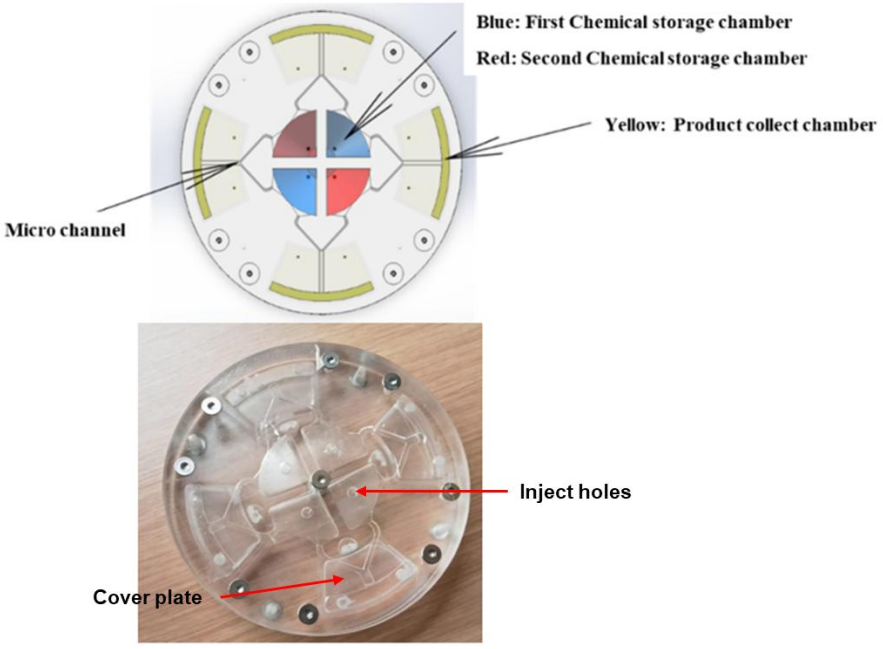

Figure 3-1 The model of microfluidic chip.

Figure 3-1 shows the model of microfluidic chip with the thickness 8 cm, radius 10cm and the width of micro tube is 0.5mm. The material of microfluidic chip is acrylic. The fabrication of thermoplastic microfluidic chips via hot embossing combined with chemical etching is a efficient and cost-effective method. Initially, a master mold featuring the desired

\

microchannel patterns is fabricated, typically using standard photolithography on a silicon or metal substrate. PMMA is then heated above its glass transition temperature and subjected to pressure to emboss the patterns from the master mold, resulting in a substrate with raised features. Subsequently, chemical etching used glacial acetic acid and concentrated nitric acid is employed to selectively remove material and precisely define the microchannel geometries and depths. Finally, the etched substrate is thoroughly cleaned and bonded to a flat cover layer using thermal or solvent-assisted methods to form enclosed microchannels. This approach allows for rapid prototyping and high-resolution microstructures suitable for various lab-on-a-chip applications.

The synthesized chemical reaction formula was listed below:

$$2(Ni(NO_3)_2 \cdot 6H_20) + NaClO + 4NaOH \rightarrow Nacl + Ni_2O_3 \downarrow + 4Na(NO_3) + 14H_2O \quad \textit{Equation 1}$$

The precursors of nickel $Ni(NO_3)_2 \bullet 6H_2O$ dissolved in water will create $Ni^{2+}$and NO_3^-. After that sodium hypochlorite with 5% active chlorine will dissociate into Na^+ and ClO^-, ClO^- will self-decomposition into cl^- and O_2. However, in alkaline condition, the self-decomposition of ClO^- will be restrained, more active ClO^- exists in the solution. Then ClO^- will react with Ni^{2+}, the Cl^+ ion in ClO^- will be reduced to Cl^- , meanwhile, $2Ni^{2+}$ lost two electrons into $2Ni^{3+}$. The product of the solution reaction

\

is $Ni_2O_3 \cdot xH_2O$, therefore the final step using air blowing thermostatic oven set as 90 ℃ to remove the H_2O in the black precipitation.

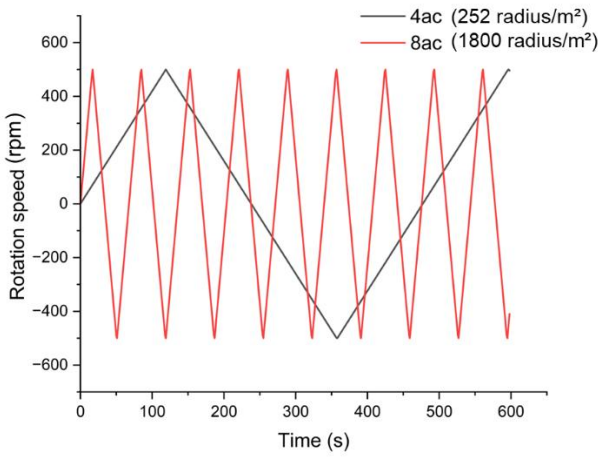

Figure 3-2 Example of cyclic rotational speed distribution of microfluidic chip.

As shown in Figure 3-2, cyclic rotational speed was applied on the microfluidic chip, 4 class acceleration (4ac) of rotation speed is 252 rad/m². 8 class acceleration (8ac) is 1800 rad/m².

In the factors analyze section, the following factors are included: rotation speed, rotation acceleration and rotation duration (time). The diameters of different groups were measured from ImageJ following the process: Particle size analysis was conducted using ImageJ by first converting the micrograph (SEM results) to an 8-bit image, applying background subtraction, and adjusting the contrast to optimize particle distinction. The image was then thresholded and binarized to create a mask. Using the "Analyze Particles" tool, all particles within a defined

\

size and circularity range were identified and measured, with particles touching the edges excluded to avoid bias. By apply the settings, only separate, complete shape particles will be involved in diameter analyzing. To ensure random selection, the complete dataset of all detected particles was exported, and a statistically random subset of 30 particles was generated using a random number algorithm in origin for final statistical determination of the size distribution.

. The experiment matrix is shown in Table 5:

Table 5 The experimental matrix for factors and their level

Rotation speed(rpm)	Acceleration class	Time (min)	Average particles diameter (nm)
500	4ac	5	399
500	4ac	10	390
500	8ac	5	600
500	8ac	10	420
1000	4ac	5	337
1000	4ac	10	320
1000	8ac	5	392
1000	8ac	10	344

The dispersion process are as followed: Place 100 mg of the sample into water and mix for 5 minutes. Subsequently, add the required

chemicals to the mixture and continue mixing for an additional 10 minutes. Transfer the resulting solution to the particle size analyzer (Bettersize 2000 Particle Sizer) to determine the particle size distribution. Activate the analyzer and mix the solution for a further 5 minutes. Apply ultrasonic treatment if necessary.

3.2.2 TiO_2- Ni_2O_3/CNT synthesis procedure

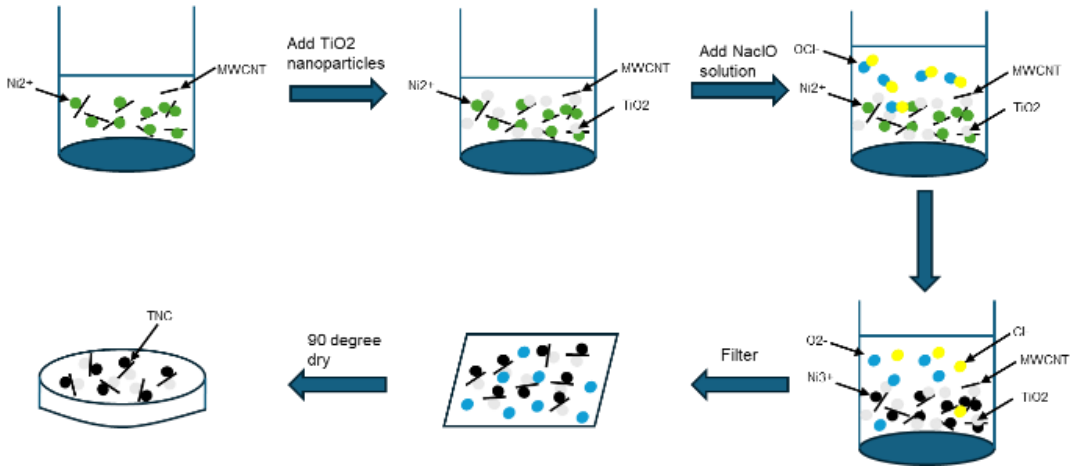

Figure 3-3. The scheme of synthesis process of TNC catalyst.

The composite wasn't synthesized by microfluidic method, the reason is that, the microfluidic synthesis approach was not employed for the preparation of the composite due to the presence of suspended TiO_2 nanoparticles and carbon nanotubes (CNTs) in the precursor solutions. These solid components pose a high risk of channel clogging, which would compromise the reproducibility and continuous-flow operation essential to microfluidic processes.

\

The synthesis of TNC composites followed a simple oxidization method shown in figure 3-3. In the experiment, 400 mg of $Ni(NO_3)_2 \cdot 6H_2O$, 400 mg of TiO_2 nanoparticles, 5 mg of oxidized CNTs and 20 ml of deionized water were mixed by ultrasonic treatment for 15 minutes before being stirred for 20 minutes to form solution A. 20 ml of NaClO with at least 4% active chlorine and 1.2 g of NaOH were added in another beaker, stirred for 30 minutes until the solution became clear with light yellow color to form solution B, which was subsequently added into solution A slowly in drop-wise manner. It can be observed subsequently the formation of black participate in the solution, which was stirred for 30 minutes before the solution became dark black. The participate was then filtered and washed with NaClO solution several times, then washed with deionized water several times. The black sol-gel was dried in the oven at 90°C overnight to remove the water in the composite. After the MWCNTs were oxidized, the surface of oxidized MWCNTs carries negative charges, which could attract positive ion in the solution (Ni^{2+}, Ti^{4+}), meanwhile, the reaction synthesis the compound happened on the surface to compose the composites.

High pH environment will inhibit the self-decomposition of sodium hypochlorite to ensure the effectiveness of active oxygen. The ion reaction is as follow:

$$ClO^- + Ni^{2+} \rightarrow Ni^{3+} + O^{2-} + Cl^-$$

\

$$NaClO + 2Ni(NO_3)_2 + 4NaOH \rightarrow Ni_2O_3 \bullet H_2O$$

$$\downarrow (Black\ participate) + H_2O + 4NaNO_3 + NaCl$$

$$Ni_2O_3 \bullet H_2O \ \rightarrow heat\ treatment \rightarrow Ni_2O_3$$

The synthesized nickel sesquioxide hydrate was treated at relatively low temperature to protect the Ni^{3+} to prevent the ion from being reduced into Ni^{2+}.

3.2.3 Oxidation process of carbon nano tubes

Initially, 1 gram of MWCNTs underwent purification through calcination at 500 °C followed by washing with 40 ml of diluted hydrochloric acid (10 wt%) to eliminate any amorphous carbon content. The resulting purified MWCNTs were then gathered, subjected to repeated washing with water, and subsequently dried overnight. In a 250-ml round flask, a mixture was prepared by combining 23 ml of concentrated sulfuric acid with the purified MWCNTs. This mixture was then stirred at room temperature for a duration of 12 hours. Then, approximately 100 mg of NaNO3 and 1 g of KMnO4 (equivalent to the mass of purified MWCNTs) were gradually added after stirring for 30 minutes at 40 °C. Afterwards, 3 ml of water was introduced, with an additional 3 ml added after 5 minutes. To regulate the temperature below 45 °C, water (40 ml) was incrementally added 5 minutes later. Following a 15-minute interval, 140 ml of water was introduced into the solution at room

temperature, followed by the addition of 10 ml of 30% H_2O_2 to terminate the reaction after 10 minutes. The oxidized MWCNTs were subsequently collected, subjected to two washes with a diluted HCl solution (5 wt%), and rinsed repeatedly with water until the pH reached or exceeded 5. The resulting suspension in H_2O was then subjected to lyophilization to obtain solid oxidized MWCNTs. [154]

3.2.4 Hydrogen generation experiment

The process was applied in Perfectlight labsolar6A photocatalysis system from Perfectlight company, the detail parts of the labsolar6A system have been shown in figure 3-4. The inner volume of the reactor is 150ml and the outer layer contains cyclic cold water. Add 10 mg catalyst in the reactor with 45 ml deionized water with 5ml triethanolamine then add 0.2 g KOH to create a relative alkaline environment. Ultrasonic for 15 minutes then turn on vacuum pump until the pressure equals to 0.01 MPa. Blow Argon into the reactor several times to wipe out the air. Turn on the cold water circulation system and gas circulation system and set cold water temperature as 5 ℃. Wait for the system to be stable for 30 minutes. Turn on the 300W Xenon lamp source to start the experiment.

\

Figure 3-4 The photocatalytic working station of PerfectLight labsolar6A system.

3.2.5 Hydrogen standard curve preparation method for GC

In order to calculate the generation rate of hydrogen production. The standard curve needs to be done first to establish the relation between peak areas and the amount of generated hydrogen (mole). As the Gas chromatograph only provide peak areas. The standard curve was created through the following procedure. Firstly, add 50 ml deionized water in the reactor (shown in figure 3-4). Turn on the vacuum pump until the pressure equals 0.01 MPa. Then blow argon into the reactor several times. Turn on the condensation circulation system, wait for the system to be stable for 30 minutes then inject 10 μl pure H_2. Turn on the 6A system for 30 minutes to diffuse the gas uniformly in the reactor

\

and get the point of 10 µl. When getting the peak areas, inject another 10µl H_2 and repeat the previous steps to get 20 µl point. Repeat the steps for three more times to get points from 30-50 µl. Fit the points as a straight line from 0 point to get the relation between amount of H_2 and peak areas. The fitted curve results shown in figure 3-5. In order to get the mole number, it can be calculated from volume divided by 22.4.

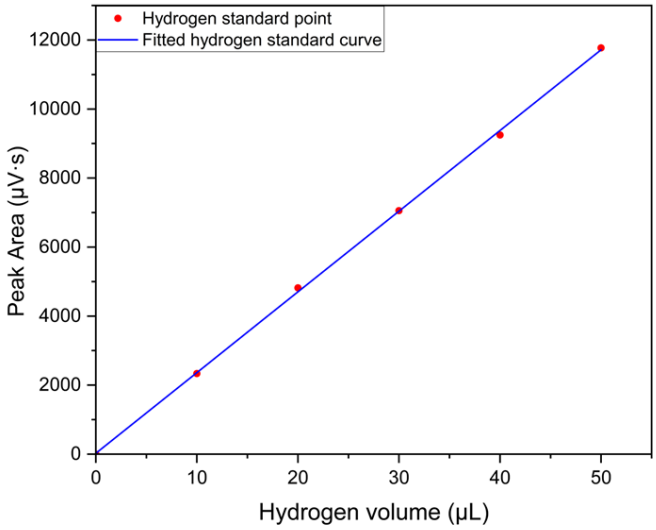

Figure 3-5. Hydrogen standard curve of gas chromatograph

3.2.6 Core-shell TiO_2- Ni/NiO/ Ni_2O_3-CNT photocatalyst synthesis

The synthesis process of the catalyst primarily followed the same process as **3.2.2.** After that, the product was calcined in an oven for 1 hour under 800 ℃ with 10% H_2 and 90% Ar atmosphere environment marked as TNC800, increased calcination time from 1 hour to 2 hour,

\

the samples are marked as TNC800-2. The 10% H_2 atmosphere was created by the following procedure. Firstly, closed the gas outlet of tube furnace. Secondly, the chamber was vacuumed by a vacuum pump for 5 minutes. After that, turn on the valve of gas cylinder with 100ul/s flow rate to slowly filled the tube with 10% H_2 and 90% Ar until the pressure reaches 1 atmosphere pressure. Open the gas outlet tube, created a slowly flow 10% H_2 atmosphere environment in the tube furnace.

3.2.7 Life cycle assessment

The carbon footprint of this novel hydrogen production technology was conducting using the Life Cycle Assessment (LCA) methodology, adhering to a series relevant standards established by the International Organization for Standardization (ISO), detailed in ISO14044 and ISO 14064[155, 156]. The carbon emissions calculation step was following the LCA framework steps, employing the IPCC 2013 GWP 100a method[157]. The LCA was performed utilizing SimaPro, a practical tool developed by PRé Sustainability Co., which facilitates the evaluation of carbon footprints through the Ecoinvent database version 3.0.3.0[158, 159]. This comprehensive database supports the management and analysis of LCA data, enabling stakeholders to conduct thorough evaluations of the environmental impacts of products and systems.

\

Goal and scope definition: The scope of the study is defined in Figure 3-6, which illustrates the boundaries of the process flow diagram, encompassing stages from the preparation of photothermal catalyst to the produce the hydrogen process. The functional unit is defined as the carbon footprint of 1 kg photothermal catalyst preparation. The objectives of this research are twofold: 1. quantify the carbon footprint of this emerging technology, 2. compare its carbon emissions with those of traditional hydrogen production technology.

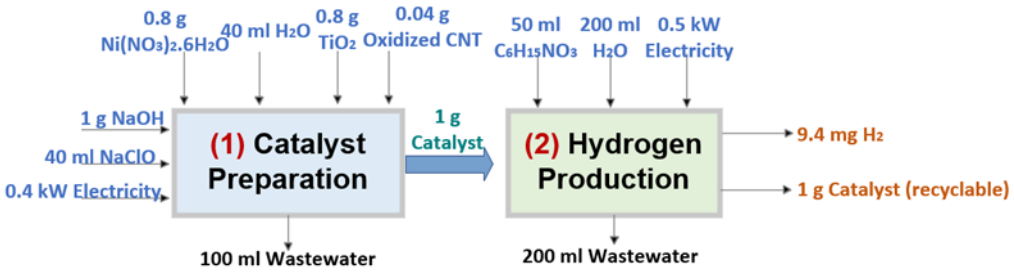

Figure 3-6 The novel hydrogen production technology process flow diagram.

Life Cycle Inventory: The inventory database for the targeted hydrogen production was gathered through experimental and monitoring, encompassing all potential carbon emissions associated with the process. As detailed in Table 6, the inventory database is composed of entries related to materials, energy, and emissions. This comprehensive collection aids in accurately quantifying the environmental impact of the desalination process.

\

Table 6 Life cycle inventory for the targeted photocatalytic hydrogen generation technology.

Material		
Indicator	**Consumption**	**Unit**
NaOH	1	g
NaClO	40	ml
$Ni(NO_3)_2.6H_2O$	0.8	g
H_2O	240	ml
TiO_2	0.8	g
Oxidized CNT	0.04	g
$C_6H_{15}NO_3$	50	ml
Energy		
Electricity	0.9	kWh
Emissions		
Wastewater	300	ml

Calculation method: The evaluation of the carbon footprint was conducted in accordance with the guidelines from the IPCC Fifth Assessment Report, covering a 100-year period[160, 161]. The results

\

are presented in terms of CO_2 equivalents, only considering six greenhouse gases. For the photocatalytic hydrogen generation process, the carbon footprint is calculated using the formula provided by the IPCC, enabling a precise quantification of the environmental impact:

$$E_i = \sum AD_i \times EF_i \ . \qquad \textit{Equation 2}$$

E_i depicts the carbon emissions from source i, AD_i represents the process activity data, while EF_i is the carbon emissions factor of activity i.

In this study, carbon emissions were mainly calculated using the above formula provided by the IPCC. The material usage, energy consumption and wastewater volume during the experiment were collected, and then the carbon emissions for each process could be obtained by using SimaPro.

3.3 Characterization of samples

3.3.1 Physical properties characterization

The morphology and microstructure of composite was characterized by **High-Resolution transmission electron microscope** (HRTEM JEOL JEM-F200) at 200kv. The **UV-Vis** results was analyzed by Shimadzu UV-3600, the sample preparation process is that the powder was finely

ground using an agate mortar and pestle to reduce particle agglomeration and ensure a uniform surface. It was then packed into a holder equipped with a transparent glass window to create a flat, opaque sample surface. The crystal structure was tested by **X-ray diffraction** (XRD D8 ADVANCE DAVINCI CuKα, λ = 1.5406， 40 kV, 40 mA). The binding energy of different samples were analyzed **X-ray photoelectron spectroscopy** (XPS Thermo Scientific K-Alpha). The chemical constituents of samples were tested by **Energy Dispersive X-ray spectroscopy** (EDS, JEOL JEM-F200).

3.3.2 Electrochemical characterization

The electrochemical characterization **(photocurrent, EIS, Mott-schottky)** were tested on a tri-electrode electrolytic cell in a CHI 760E electrochemical workstation (counter electrode: platinum wire; reference electrode: Ag/AgCl electrode; electrolyte: 20% l-lactic acid water solution) from CH Instruments Ins company. The methods of preparing working electrode were as follow:

Firstly, add 60mg samples in 9 ml ethanol. Stirred and then added 50μl Teflon and ultrasonic for 15 minutes. Then dripped the solution on the 1 × 4 cm F-doped tin oxide (FTO) glass. Then washed with deionized water for several times and dry at 80 ℃ for 4 hours.

Z View is a software used to analyze the composite resistance of different parts from AMETEK Scientific Instruments with version v.40h

\

. To extract resistance values from EIS data in Z View, an appropriate equivalent circuit model is constructed and fitted to the experimental impedance spectrum using a non-linear least squares (NLLS) algorithm. After assigning initial values and performing global fitting, the optimized parameters—including specific resistances such as solution resistance (R_s) and charge-transfer resistance (R_{ct})—are obtained, providing quantitative insight into the electrochemical interface processes [162] [163].

Photoluminescence (PL) spectra were acquired at room temperature using a Edinburgh FLS1000 spectrofluorometer equipped with a 150 W xenon arc lamp as the excitation source. Finely ground powder samples were packed into a solid sample holder, and the excitation wavelength was set to 325 nm with excitation and emission slit widths maintained at 5 nm to ensure optimal signal resolution. The emission spectra were collected across a range of 350 to 800 nm using a photomultiplier tube (PMT) detector operating in photon-counting mode, with all spectra automatically corrected for instrumental response. The resulting PL intensity, which is inversely correlated with charge carrier separation efficiency, was analyzed to evaluate the influence of Ni_2O_3 content on the recombination dynamics within the TiO_2-Ni_2O_3/CNT composites. The sample preparation for **time-resolved photoluminescence** (TRPL) measurements followed the same procedure as for steady-state PL, but with stricter requirements on

sample concentration and homogeneity to avoid artifacts such as concentration quenching and scattering, which are critical for obtaining accurate fluorescence lifetime data. The measured PL intensity is unsuitable for direct quantitative comparison between samples or different experimental groups because it is convoluted by numerous extrinsic factors, including instrumental response variability (e.g., excitation source power, optical alignment, and detector sensitivity) and sample-dependent optical effects (e.g., light absorption, scattering, and inner-filter effects), rather than solely reflecting the material's intrinsic quantum yield [164]. Consequently, PL intensity is typically reported in arbitrary units and is only reliable for qualitative analysis or for identifying trends within a series of measurements performed under identical conditions; for robust, quantitative comparison of charge carrier dynamics, TRPL measurements of fluorescence lifetime are essential as this parameter is an intrinsic property of the emissive state and largely independent of these confounding variables [165].

\

4 Chapter 4. Centrifugal microfluidic synthesis of Ni_2O_3 nanoparticles.

4.1 Introduction

The synthesis of nanoparticles with tailored properties has garnered significant attention in scientific and technological research, driven by their unique characteristics and versatile applications. Nickel oxide (Ni_2O_3) nanoparticles, in particular, have emerged as promising materials due to their remarkable electrical, optical, and magnetic properties [61, 62, 166]. However, conventional synthesis methods often encounter challenges in achieving precise control over nanoparticle size, shape, and composition, limiting their potential for practical applications [167]. To overcome these limitations, microfluidic technology has emerged as a powerful approach for the synthesis of Ni_2O_3 nanoparticles, offering enhanced control, reproducibility, and scalability [128] [128].

Microfluidics which involves the manipulation of fluids at the microscale has gained prominence in recent years owing to its ability to precisely control reaction conditions and exhibit unique fluidic behaviors [168-170]. Microfluidic platforms provide numerous advantages for nanoparticle synthesis, including superior mixing efficiency [171], rapid heat transfer [169], and the capability to perform multiple steps in a controlled manner [172].Wu et al. [173] introduced current-flow field in micro-mixer which significantly improved the mixing efficiency. Sasaki

\

et al. [174] similarly introduced a pair of coplanar electrodes to enhance the mixing efficiency. These features enable precise control over the nucleation, growth, and assembly processes, facilitating the synthesis of Ni_2O_3 nanoparticles with tailored properties.

Several synthesis strategies have been successfully implemented in microfluidic systems for the controlled fabrication of nanoparticles [169, 175]. For instance, Lian et al. effectively connected microfluidics in manufacturing TiO_2 nanoparticles through surfactant wrapping sol-gel strategy, with TiO_2 nanoparticles equitably conveyed on the external surface of the multi-wall carbon nanotubes (MWCNTs), and it has the capacity to photodegrade Rhodamine B for wastewater treatment [176].

Characterization of the synthesized Ni_2O_3 nanoparticles is critical for understanding their structural, morphological, and compositional properties[90, 177-179]. Techniques such as X-ray diffraction (XRD), transmission electron microscopy (TEM), scanning electron microscopy (SEM), and Fourier-transform infrared spectroscopy (FTIR) can provide valuable insights into the crystal structure, size, shape, and surface chemistry. These characterization techniques enable researchers to establish correlations between nanoparticle properties and their performance in specific applications, facilitating further optimization and customization.

\

Therefore, microfluidic synthesis offers a promising pathway for the controlled fabrication of Ni_2O_3 nanoparticles with enhanced properties. The precise control over reaction conditions, uniform size distribution, and tunable morphology and crystalline of the nanoparticles open up exciting possibilities for their integration into various energy and environmental applications. Among various microfluidic systems, centrifugal microfluidics has demonstrated superior properties in comparison to the conventional pump-driven microchips. For instance, it requires only a compact motor to generate the centrifugal pumping for fluid manipulation and hence will eliminate the need of syringe pumps. The complete fluidic network can be contained in a single disc. The different fluidic functions such as valving, decanting, calibration, mixing, as well as sample splitting and separation have been successfully integrated on the centrifugal microfluidic platform. Furthermore, the centrifugal microfluidic disk can be fabricated to be disposable in an economical way by mass-production from inexpensive materials such as polycarbonate. To the best of our knowledge, there has no work reporting the synthesis of Ni_2O_3 nanoparticles using centrifugal microfluidics. By exploring recent advancements in microfluidic synthesis, this chapter therefore aims to provide a new strategy using centrifugal microfluidic platform for the synthesis of nanomaterials.

\

4.2 Microfluidic design and simulation results

4.2.1 Simulation model and calculations

The simulation was conducted using the Ansys Fluent program to simulate the flow and mixing conditions of two different fluids in a microchannel. This simulation aims to provide insight into the underlying principles of microfluidics by enabling the direct visualization of internal flow dynamics within a microchannel. The flow conditions were analyzed in terms of velocity vectors and heat exchange. The following assumptions were adopted in the simulation model:
The volume of fluid method was employed with energy and gravity effects enabled. Turbulent flow conditions were represented using the SST k-omega viscous model. Two fluids, alcohol and water were included. For the stationary flow scenario, an inlet velocity of 2 m/s was imposed, while under centrifugal conditions, a rotational speed of 500 rpm was applied.

Table 7 The parameters of simulation model.

Simulation dimensions	Rectangular inlet microtube	Rectangular mixing tube
Width	500μm	1mm
Length	8mm	10mm
Depth	500μm	500μm

\

Two fluids, alcohol and water, were specified for the simulation. The reason for choose water and alcohol to simulate the process is because the density and other physical factors between reactants, water and alcohols are similar. The parameters of flow tube have been shown in Table 7. In the stationary flow condition, an inlet velocity of 2m/s was assigned to the flow fluid. For the centrifugal condition, a centrifugal speed of 500rpm was applied. To analyze the impact of centrifugal microfluidic application, the velocity vector distribution and phase interactions between these two conditions were compared.

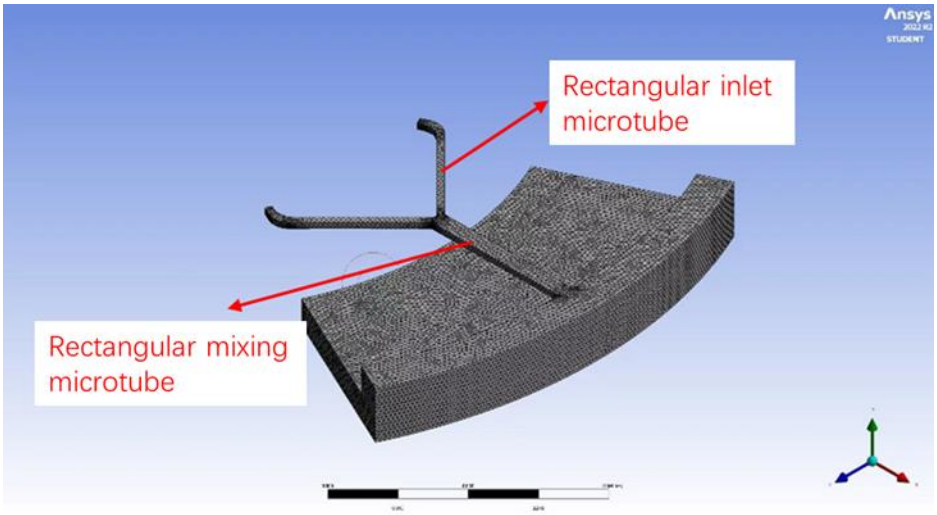

Figure 4-1 Simulation mesh of microchannel of microfluidic chip.

On a rotating microfluidic chip, the fluid will experience the Centrifugal force,

$$F_c = \rho r \omega^2 \qquad \textit{Equation 3}$$

Euler force for non-uniform velocity condition,

\

$F_E = \rho r * d\omega/dt$ *Equation 4*

For Coriolis force (Density):

$F_{cr} = 2\rho\omega v$ *Equation 5*

Navier-stokes equations for motion describing of momentum in a viscous fluid in simulation:

$\rho \frac{\partial V}{\partial t} = \rho f - \nabla p + \mu \nabla^2 V$ *Equation 6*

Transformed into Equation 7

$\frac{\partial V}{\partial t} + (V * \nabla)V = f - \frac{1}{\rho}\nabla p + \frac{\mu}{\rho}\nabla^2 V$ *Equation 7*

In the equation, ρ represents density, *r* is radius, ω is angular velocity, *t* is time, *v* is velocity, *V* is velocity vector, *p* is pressure, *f* is the external force per unit volume of fluid, if only gravity is considered, then *f*= ρg, *g* is gravity, μ is dynamic viscosity.

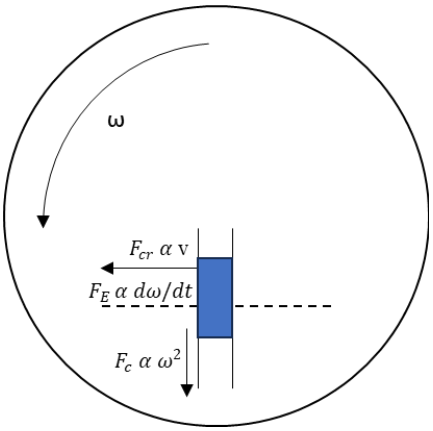

\

Figure 4-2 Force distribution and direction on a rotating centrifugal microfluidic chip.

Grid independence analyzes which aims to investigate the reliability of simulation mesh, the simulation has been run under different mesh. The mesh element size is 0.005, 0.0035 and 0.0075 corresponding to 464829, 645872 and 215249 elements. Compare the corresponding velocity magnitude to analyze the reliability. As shown in Figure 4-3, the plot of 0.005 and 0.0075 are similar, the results of 0.0035 is relative close to the figure of 0.005, therefore, 0.005 element size mesh was applied to the simulation.

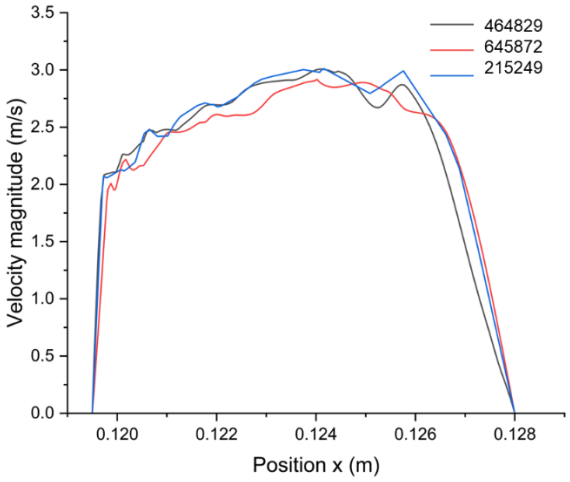

Figure 4-3 Grid independence analyze results.

4.2.2 Simulation results

\

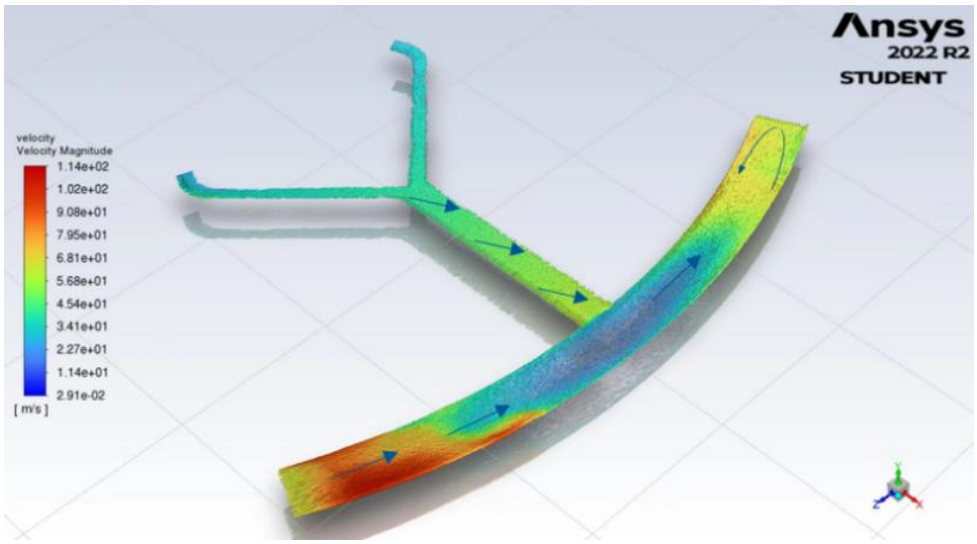

Figure 4-4 Plot of flow in centrifugal microfluidic channel.

Figure 4-4 displays the velocity vector distribution results of the microchannel following the addition of a 500rpm counterclockwise and clockwise rotational speed. The reason for included velocity magnitude distribution is to see the ununiform flow condition inside microfluidic chip. As shown in Figure 4-5, the flow field becomes more unstable, and the interphase exchange significantly increases. Within the microchannel, the high-velocity region is observed at the distal portion of the mixing channels. In the collecting chamber, high velocities accumulate at both the left and right ends of the chamber. This phenomenon is attributed to the cyclic fluctuations in rotational speed, with the plot generated during a speed decrease cycle.

\

4.3 Experimental results and discussion

The morphology and microstructure of the microfluidic-synthesized nanoparticles were characterized using a scanning electron microscope (SEM). The crystal structure and purity were investigated through x-ray diffraction (XRD) analysis, as shown in Figure 4-5 and Figure 4-6, respectively. The SEM results reveal the complete particle shape of Ni_2O_3, with the nanoparticles bonded together to form loose aggregates. Unlike the conventional synthesis methods that typically require several hours, the reaction time in this research was reduced to five minutes. The activity included in the reaction time is mixing reactants on magnetic stirrer for the conventional method. In microfluidic synthesis, the activity is rotation of microfluidic chip. Furthermore, the study analyzed the effects of rotation speed, rotation acceleration, and rotation on the particle diameter and purity. The particle diameters were calculated using ImageJ software to analyze SEM results, while the purity was assessed based on the XRD patterns.

\

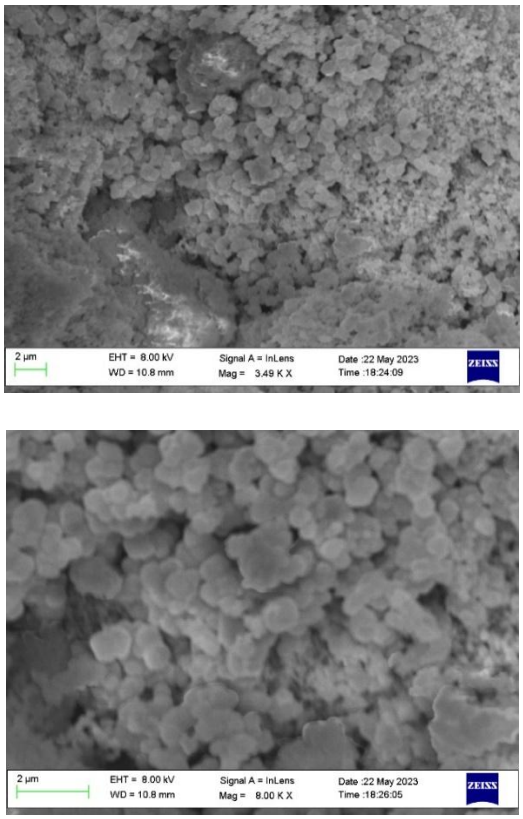

Figure 4-5 SEM results of synthesized Ni_2O_3 Nano particles.

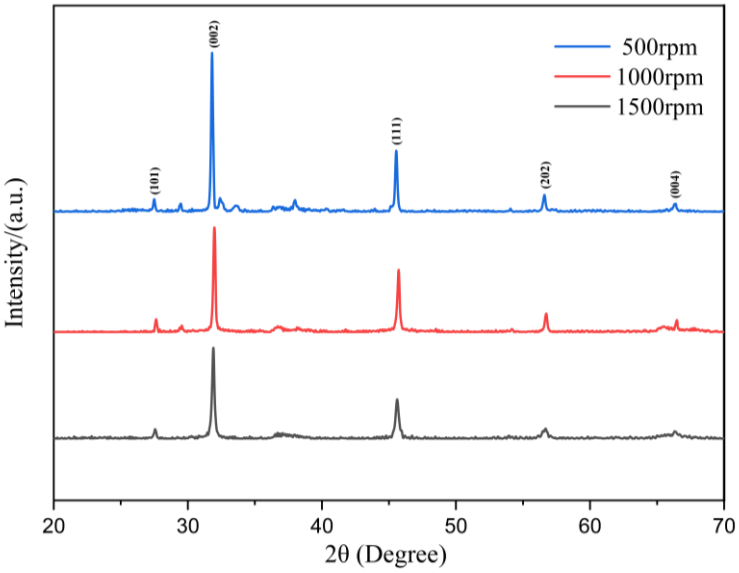

Figure 4-6 The x-ray diffraction pattern of synthesized Ni_2O_3 nano particles.

\

Figure 4-6 presents the x-ray diffraction (XRD) pattern of the particles synthesized at rotation speeds of 500 rpm, 1000 rpm, and 1500 rpm. The observed peaks at 27.64°, 31.66°, 45.61°, 56.58°, and 66.2° correspond to the crystal surfaces of the (101), (002), (111), (202), and (004) planes, respectively. Figure 4-7 shows the HRTEM figure of synthesized Ni_2O_3 Nano particles, it can be summarized that, the nano particles has relative complete sphere shape, the size varies form 30nm to 80nm, there is also some impurity content shown in the figure, it should be the NaCl crystal and NaOH, this also explain the wave peaks in XRD pattern. The observed discrepancies in particle size measurements between Scanning Electron Microscopy (SEM) and Transmission Electron Microscopy (TEM) primarily stem from fundamental differences in their imaging principles and sample preparation requirements. TEM provides high-resolution two-dimensional projections of individual particles, allowing for precise measurement of the core particle size with minimal interference [180] . In contrast, SEM captures three-dimensional surface topography, where the apparent particle size can be significantly influenced by surface coating (e.g., sputtered gold or carbon layers) and charging effects [181]. Consequently, SEM measurements often systematically overestimate particle size due to the additional conductive layer and surface artifacts, whereas TEM is generally regarded as more accurate for determining the true nanocrystal dimensions. In this case, the

analysis was based on SEM results because, despite their limited absolute accuracy, they provide sufficient consistency for reliable comparative evaluation.

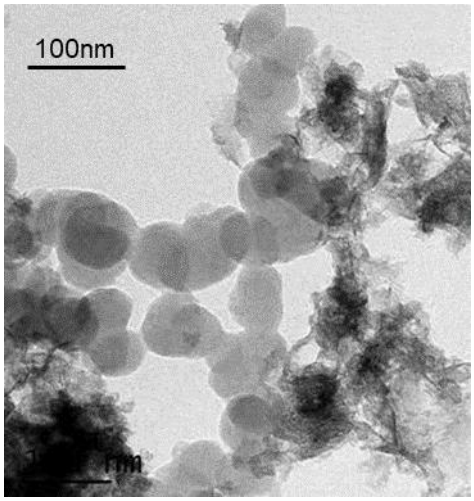

Figure 4-7 HRTEM results of synthesized Ni_2O_3 Nano particles.

The synthesized process was a pure 5-minute reaction time without any purification or washing procedures. Consequently, the XRD results exhibit miscellaneous peaks due to the presence of impurities, primarily sodium chloride (NaCl), which is a byproduct of the reaction. As the experiment needs excess amount of sodium hydroxide, therefore the final product may contain NaOH when washing is incomplete. Comparing the three rotation speeds, the 500rpm group exhibits additional peaks around the main peak of Ni_2O_3 (31.66°), indicating relatively lower particle purity. As the rotation speed increases, the

occurrence of miscellaneous peaks diminishes, and the curve around 31.66° becomes smoother. In the 1500 rpm group, the curve appears smooth with minimal disturbances, confirming the high purity of the crystal surface.

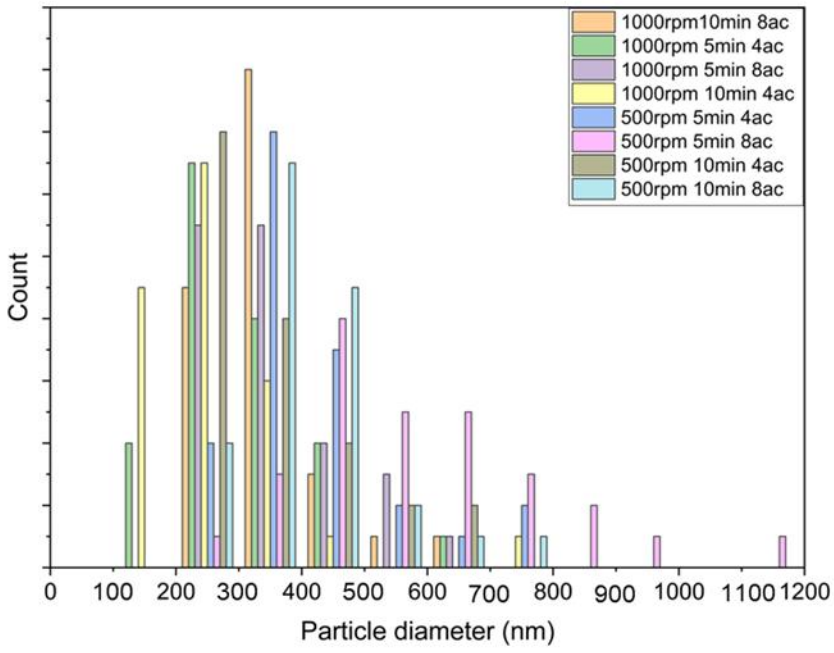

Figure 4-8 The particles diameter distribution of all groups.

The diameter of synthesized Ni_2O_3 nano particles are plotted in Figure 4-8, the statistical method is to using ImageJ to recognize the sphere shape particles in the SEM results, randomly pick 30 particles from the SEM picture, count the diameter of the particles and analyses the distribution and curve. Moreover, the acceleration 4, 8 represents the

acceleration class, the actual acceleration is 252 rad/m². 8 class acceleration (8ac) is 1800 rad/m².

4.3.1 Effect analyze

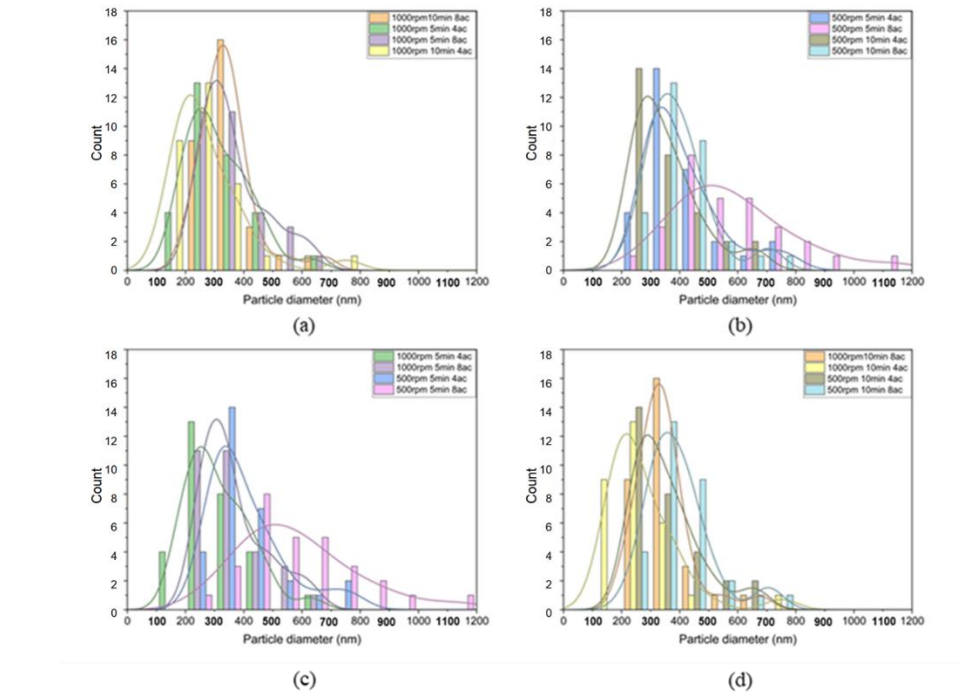

Figure 4-9 The diameter distribution of different group (a) At 1000 rpm, different time and acceleration. (b) At 500 rpm, different time and acceleration. (c) At 5 minutes, different rotation speed and acceleration. (d) At 10 minutes, different rotation speed and acceleration.

To investigate the influence of different factors on microfluidic synthesis, the data were divided into four groups for separate analysis of their effects. Figure 4-9(a) illustrates the results for the 1000 rpm

\

condition. In this condition, the smallest diameter range observed is 100 nm-200 nm. Within this range, the 1000 rpm 10 min 4ac group exhibits the highest particle count. Comparing the 5 min 4ac and 10 min 4ac groups, it can be concluded that as the reaction time increases, the particle diameter range shifts from larger sizes to smaller sizes. Approximately 80% of the particles in the 1000rpm 10min 4ac group are below 300 nm, while only about 60% of the particles in the 5 min 4ac group fall within that range. Similar observations can be made for the 1000 rpm 5 min 8ac and 1000 rpm 10 min 8ac groups, where the diameter ranges are more concentrated below 400 nm. Notably, nearly 90% of the particles in the 10 min 8 ac group are below 400nm, and it also exhibits the highest particle count within that range, indicating a narrower distribution of particle diameters.

Figure 4-9(b) demonstrates a similar trend. In the 500 rpm condition, the highest particle count for the 10 min 4 ac group falls between 200 nm-300 nm. Comparing this with the 5 min 4 ac group, a clear shift in the peak can be observed from 300 nm-400 nm to 200 nm-300 nm. This effect becomes more pronounced when comparing the 5 min 8 ac and 10 min 8 ac groups. The diameter distribution for 5 min 8 ac is broader, with a mean particle diameter over 580 nm. However, with an increase in reaction time, the diameter distribution becomes more concentrated and shifts towards a lower range.

\

The results from Figure 4-10 support these findings. With an increase in mixing time, the mean particle diameter significantly decreases for the 500 rpm 8 ac and 1000 rpm 8 ac groups. The effect is relatively smaller for the 500 rpm 4 ac and 1000 rpm 4 ac groups.

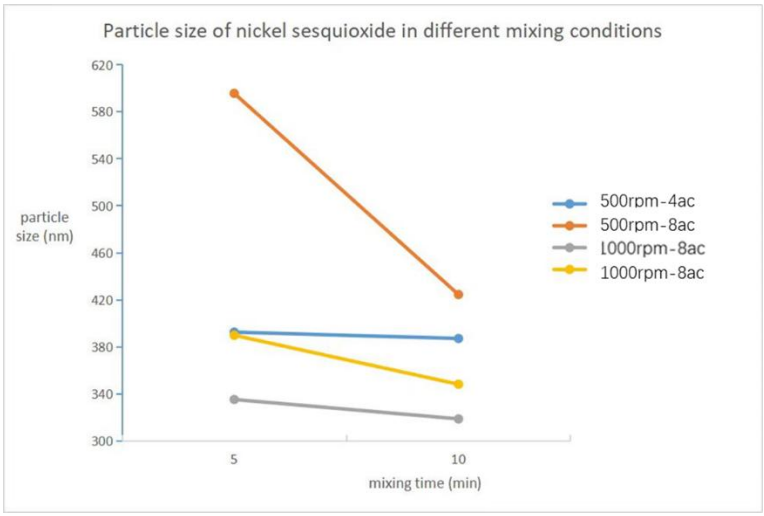

Figure 4-10The effect of reaction time on mean particles diameter.

From Figure 4-9(c) and Figure 4-9(d), the effects of rotation speed are analyzed. At the same reaction time and acceleration, an increase in rotation speed leads to a decrease in particle diameter and a narrowing of the diameter distribution. In the 5 min 4 ac group, the performance of 1000 rpm 5 min 4 ac is superior to that of 500rpm 5min 4 ac. Over 90% of the particles in the 1000 rpm 5 min 4 ac group are smaller than 400 nm, with the majority focusing around 200nm. Conversely, for the 500 rpm 5 min 4a c group, the diameter range is more concentrated between 300 nm and 500 nm. Similar observations can be made for the

\

500 rpm 5 min 8 ac and 1000 rpm 5 min 8 ac groups, as well as for the 500 rpm 10 min 4 ac and 1000 rpm 10 min 4 ac groups.

In contrast, the acceleration factor exhibits different behavior compared to the other two factors. As shown in Figure 4-9 and Figure 4-10. In the 5 min group, increasing the acceleration from 4 to 8 (representing an increase from252 rad/m² to 1800 rad/m²) results in an increase in average particle diameter. Comparing the 500 rpm 5 min 4 ac and 500 rpm 5 min 8 ac groups, as well as the 1000 rpm 5 min 4 ac and 1000 rpm 5 min 8 ac groups, the diameter distribution range shifts to a larger range with the increase in acceleration. A similar pattern is observed in the 10 min groups, where the 8 ac groups exhibit larger diameters and wider diameter distributions compared to the 4 ac groups.

4.4 Conclusion

Our work investigates the effects of various factors on the morphology, purity, particle size, and particle size distribution in the synthesis of Ni_2O_3 nanoparticles using centrifugal microfluidics, which has significantly reduced the processing time from hours to 5 -10 minutes, in comparison to conventional procedures. With the help of simulation model, the mechanism for the improvement is that, microfluidic has powerful mixing efficiency which significantly improve the substance exchange and reaction speed. Thereby it will provide new insights for nanoparticle synthesis using centrifugal microfluidics. In this work, the

\

rotational speed of the microfluidic disc and the reaction duration contribute as a determining role to particle size reduction and a narrower particle size distribution. However, the rotational acceleration exhibits an inverse relationship, whereby an increase in acceleration leads to an enlargement of particle size and a wider particle size distribution.

\

5 Chapter 5. Photocatalytic hydrogen evolution of TiO_2-Ni_2O_3/CNT heterojunctions

5.1 Introduction

Photocatalytic hydrogen production, a critical aspect of sustainable energy research, has seen increasing focus on the development of advanced composite materials to boost efficiency and effectiveness[4, 182, 183]. The process of water photolysis for hydrogen generation addresses contemporary energy and environmental challenges effectively[184]. Hydrogen, with its high energy density, sustainability, and zero carbon emissions, is considered a premier future energy source[185, 186]. Nevertheless, existing photocatalytic technologies encounter several limitations, including low energy conversion efficiency, inadequate sunlight utilization, rapid electron-hole recombination, and instability. To mitigate these issues, various strategies have been employed to modify semiconductor properties, such as metal doping, bandgap alteration, and the introduction of heterogeneous structures, which significantly improve the efficiency and stability of photocatalytic hydrogen production. Typically, these catalysts incorporate precious metals like platinum (Pt) and gold (Au) to enhance electron transfer and create an efficient internal field[66, 187], boosting catalytic performance. However, these modifications also elevate the cost, posing challenges for widespread industrial application. Modification through heterojunctions, such as p-n junctions,

\

Type II junctions, and z-type junctions, can direct electron flow, enhance charge separation, and reduce electron recombination time[188]. The innovative Ni_2O_3-TiO_2/CNT composite includes a z-type heterojunction, enhancing charge separation capabilities.

Titanium dioxide, known for its photocatalytic properties, triggers redox reactions upon light absorption, generating electron-hole pairs. These pairs, however, tend to recombine quickly and have limited visible light absorption, reducing the overall process efficiency[189] [190] [152] [191]. Nickel trioxide, serving as a co-catalyst, exhibits excellent electronic conductivity, which aids in the separation of these charge carriers and lessens recombination losses[192] [90] [166] .This synergistic interaction between TiO_2 and Ni_2O_3 enhances charge carrier lifetimes, significantly improving the efficiency of photocatalytic hydrogen production. The inclusion of carbon nanotubes further boosts the composite's performance. Owing to their high surface area and exceptional electrical conductivity, carbon nanotubes promote efficient electron transfer and facilitate the movement of charge carriers to the photocatalyst's surface. This structural addition not only prevents charge recombination but also lends durability and stability to the composite, ensuring consistent performance in repeated photocatalytic reactions.

This advanced composite capitalizes on its ability to utilize a wider spectrum of light, extending from ultraviolet to visible light. The enhanced light absorption of the Ni_2O_3-TiO_2/CNT (TNC) composite marks it as an effective solar energy harvester, broadening its practical applications. Meanwhile, this study evaluates the carbon footprint of this novel photocatalytic hydrogen production and then gives a comprehensive analysis of other hydrogen production methods, including the gray hydrogen and blue hydrogen production from industry process.

5.2 Results and discussion

5.2.1 Morphology and physical results

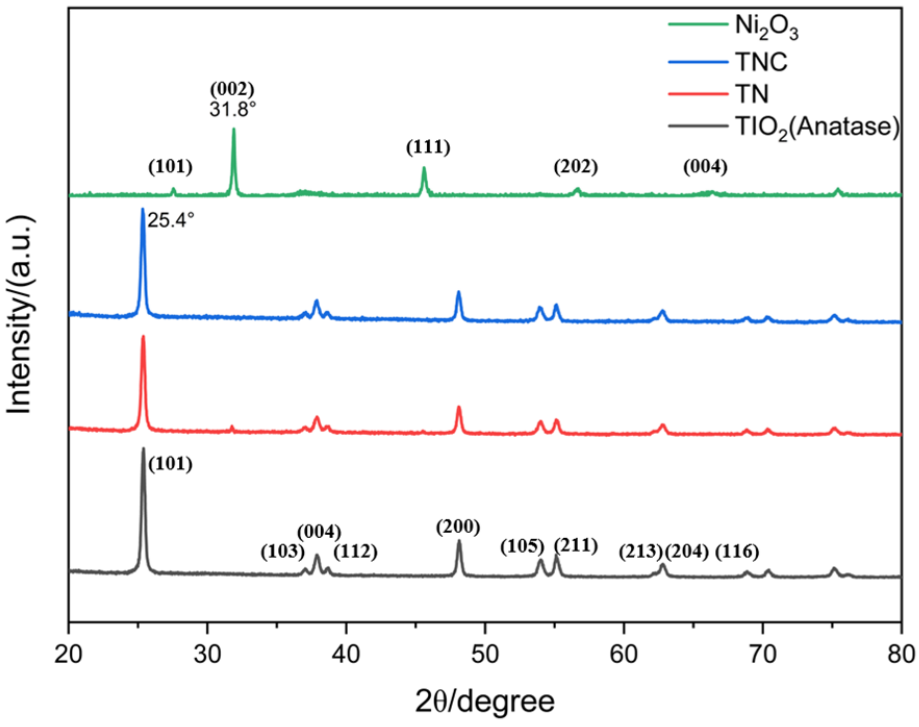

\

Figure 5-1XRD pattern of TNC, TN and TiO_2

Figure 5-1 depicts the XRD pattern of three samples: TiO_2, TiO_2-Ni_2O_3 (TN), and TiO_2-Ni_2O_3/CNT (TNC). The XRD analysis reveals that the predominant crystal structure present in all samples is TiO_2 (anatase). Notably, the major peaks of TiO_2 (anatase) are observed at 2θ=25.4°, 36.9°, 37.8°, 38.5°, 48.0°, 51.9°, 53.9°, 55.1°, 62.1°, 62.7°, and 68.9°, corresponding to the (101), (103), (004), (112), (200), (202), (105), (211), (213), (204), and (116) crystalline planes, respectively. All samples exhibit prominent peaks attributed to TiO_2 (anatase), with the highest intensity peak observed at 25.4°, indicating high purity and a well-defined crystal structure[193]. The average lattice constant of TiO_2 anatase is determined to be 3.7761 nm, a parameter that is conducive to efficient charge transfer and catalytic performance. A minor peak is observed at 31.8° in the sample, corresponding to the predominant peak of Ni_2O_3 crystalline structure, specifically the (101) crystalline plane[194, 195]. This minor peak is attributed to the relatively low proportion of Ni_2O_3 (25% mol ratio) within the sample. The XRD pattern of TiO_2-Ni_2O_3/CNT closely resembles that of TiO_2, suggesting a similar crystalline composition. This observation can also be attributed to the issue of Ni_2O_3 proportion within the sample, indicating a need for further optimization in controlling the ratio of Ni_2O_3 in the composite material.

\

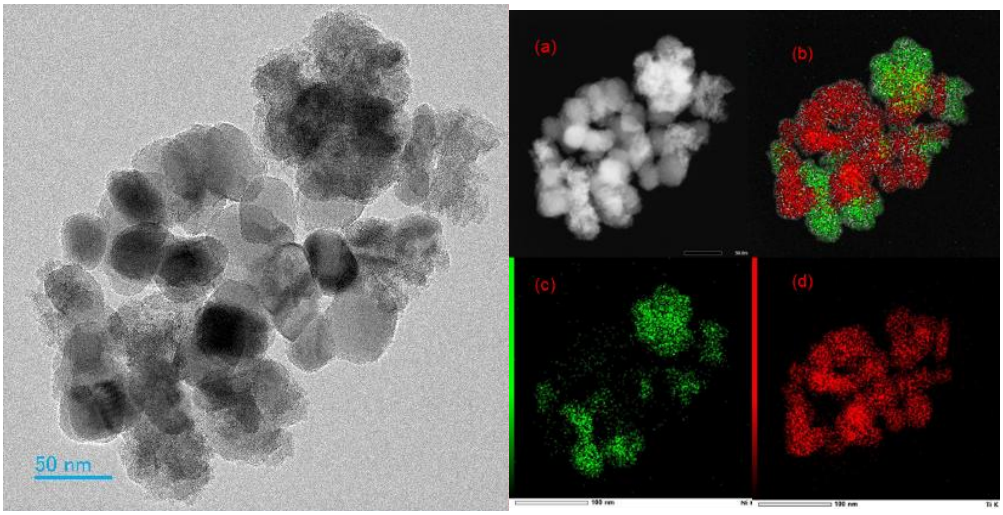

(A) (B)

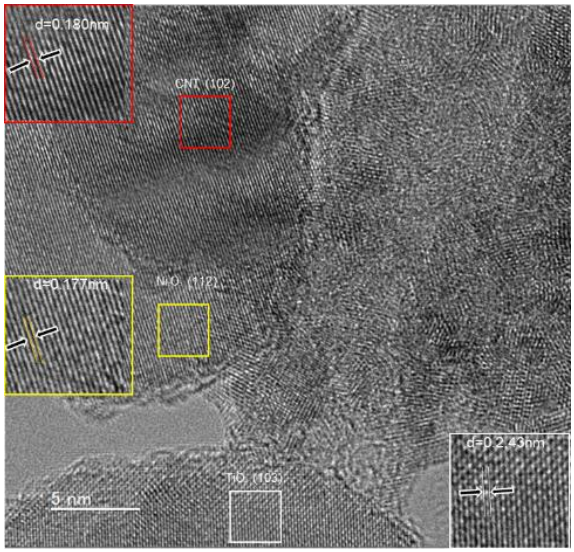

(C)

Figure 5-2(A) HRTEM pattern of TNC composite. (B)Eds mapping results of Ni and Ti element. (B)(a) The morphology of particle

compound. (B)(b) Mapping of Ni (green) and Ti (red) element. (B)(c) Mapping of nickel element. (B)(d) Mapping of titanium element. (C) HRTEM results of composite.

In Figure 5-2(B), the elemental mapping of Ni and Ti reveals that the synthesized Ni_2O_3 nanoparticles exhibit good contact with TiO_2 nanoparticles. Figure 5-2(B)(a) illustrates the morphology of the composites, characterized by numerous spherical particles. Figure 5-2(B)(b) displays the distribution of Ni and Ti elements, while Figure 5-2(B)(c) and (d) depict each element individually. The energy-dispersive X-ray spectroscopy (EDS) results demonstrate that the synthesized Ni_2O_3 nanoparticles establish effective contact with TiO_2 nanoparticles and are uniformly distributed within the composite.

The HRTEM images in Figure 5-2(A) reveal complete spherical particles with an average size of approximately 30 nm. Particle accumulation, as observed in Figure 5-2(A), ensures direct crystal face contact between each component.

Figure 5-2(C) presents the high-resolution TEM (HRTEM) results of the composite. The HRTEM image displays a lattice fringe of 0.180 nm in the top-left position of the composite (indicated by the red triangle), consistent with the (102) crystal plane of carbon nanotubes (CNT) (PDF#41-1487). The lattice fringe of 0.177 nm, observed in the left yellow

\

triangle, corresponds to the (112) crystal plane of Ni_2O_3 (PDF#14-481). Furthermore, the bottom area exhibits a lattice fringe of 0.243 nm, corresponding to the crystal plane of TiO_2 (anatase) (103) (PDF#21-1272). These HRTEM observations confirm the distinct crystallographic features of each component within the composite structure.

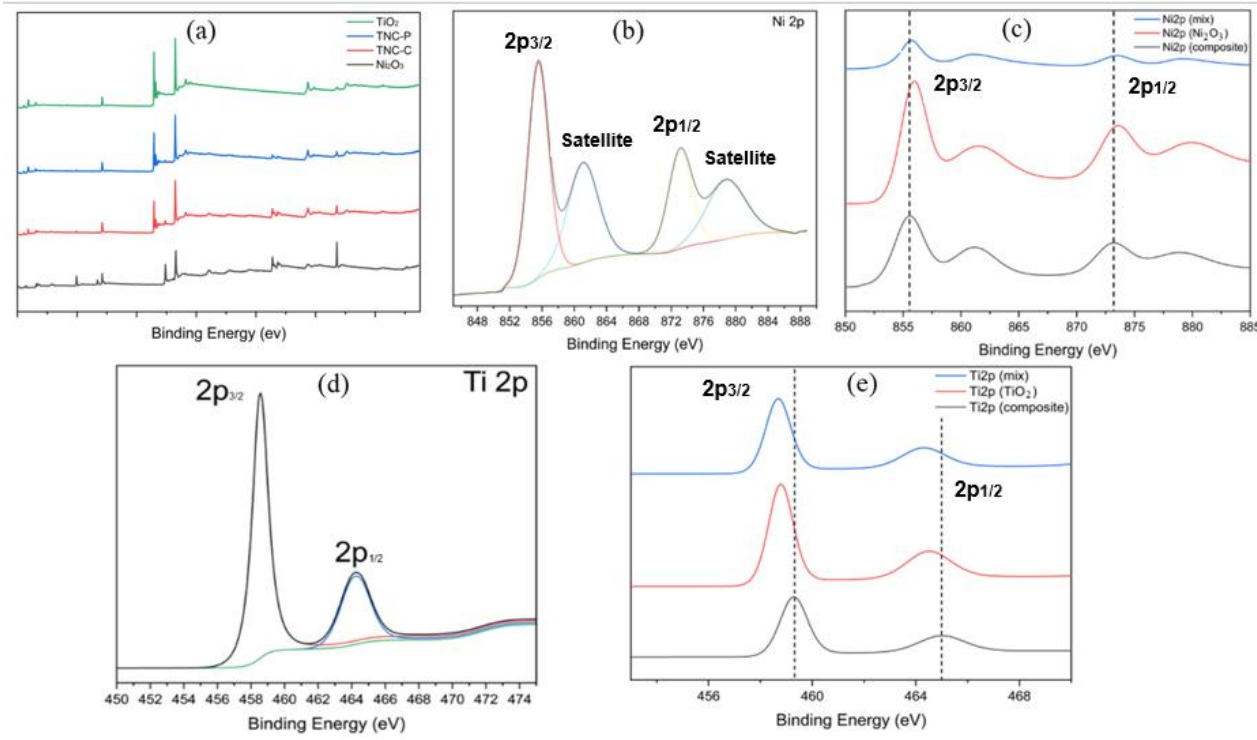

Figure 5-3 XPS results of (a) Ni_2O_3/TiO_2-CNT (b) Ni 2p (c) Ni 2p in composition, physical mix sample and pure Ni_2O_3 (d) Ti 2p of pure TiO_2 (e) Ti 2p in composition, physical mix sample and pure TiO_2

In order to obtain detailed information regarding the valence states of elements and chemical compositions, the samples were subjected to X-ray photoelectron spectroscopy (XPS) analysis. As depicted in Figure 5-

\

3(a), the XPS results reveal the presence of Ti, Ni, O, and C elements. Figure 5-3(b) presents the Ni 2p spectrum, which exhibits four main peaks. The peaks observed at 855.4 eV and 873.4 eV correspond to Ni $2p^{3/2}$ and Ni $2p^{1/2}$, respectively, while the satellite peaks are located at 861.2 eV and 879.0 eV. These four peaks provide evidence supporting the valence state of nickel as Ni_2O_3. Figure 5-3(d) displays the spectrum results of Ti 2p, revealing two distinct peaks at 458.6 eV and 464.2 eV, corresponding to Ti $2p^{3/2}$ and Ti $2p^{1/2}$, respectively. To determine the direction of electron flow and hetero-junction characteristics, a comparison of XPS results among the composition, pure Ni_2O_3/TiO_2, and physical mix was conducted. As illustrated in Figure 5-3(c), noticeable peak shifts are observed; both Ni $2p^{3/2}$ and Ni $2p^{1/2}$ peaks shift to lower binding energy positions, indicating electron transfer to Ni_2O_3 during catalysis. Similarly, in Figure 5-3(e), the peaks of Ti $2p^{3/2}$ and Ti $2p^{1/2}$ shift to higher binding energy ranges. Based on these observations, the electron transfer path can be proposed as follows: solar energy activates electrons in TiO_2, followed by electron transfer to the surface of Ni_2O_3 via CNT and recombined with the holes from Ni_2O_3. After that, the electrons motivated from Ni_2O_3 react with free H^+ ions in the solution to generate H_2. The electron flow path and reaction pattern are depicted in Figure 5-4, indicating a typical z-type heterojunction, electrons move from low band position to high, holes move from high position to low, enlarge the electron exist time and restrain the repair of electrons and holes. In order

\

to determine the band position of Ni_2O_3 and TiO_2, UV-Vis and Mott-Schottky were applied. The optical band gap energy (*Eg*) of the semiconductor sample was determined from ultraviolet-visible (UV-Vis) absorption spectroscopy data using the Tauc method. This approach is employed to account for the electronic transition type (direct or indirect allowed) and is based on the principle that the absorption coefficient (*α*) near the band edge follows the equation:

$$(\alpha h\nu)^n = A(h\nu - E_g) \qquad \textit{Equation 8}$$

where:

α is the absorption coefficient (in cm^{-1}),

hv is the photon energy (in eV),

A is a proportionality constant,

E_g is the optical band gap energy (in eV),

n is a power index *n*=1/2 for TiO_2, and *n*=2 for Ni_2O_3.

The requisite Tauc plot is then constructed by plotting $(\alpha h\nu)^{1/n}$ versus the photon energy *hv*. Finally, fitted line to the x-axis finding the value of *hv* where $(\alpha h\nu)^{1/n}$ =0 which is bandgap.

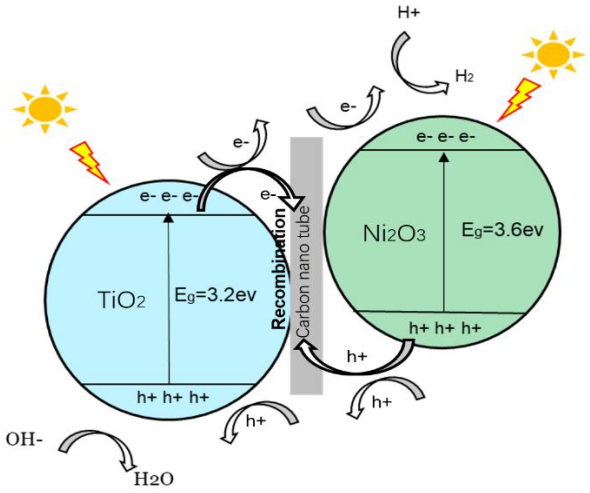

Figure 5-4 The composition catalysis pattern of electrons and holes transfer path

Figure 5-5 shows the results of Mott-schottky results of TiO_2 and Ni_2O_3, as the figure shown, the forbidden band position for TiO_2 is -0.83V and Ni_2O_3 is 0.97V.

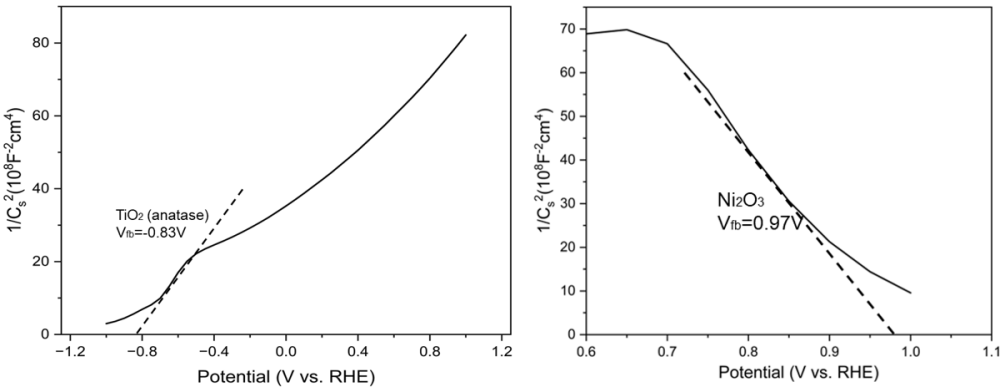

Figure 5-5 Mott-Schottky results of TiO_2 and Ni_2O_3

\

5.2.2 electro-photo results

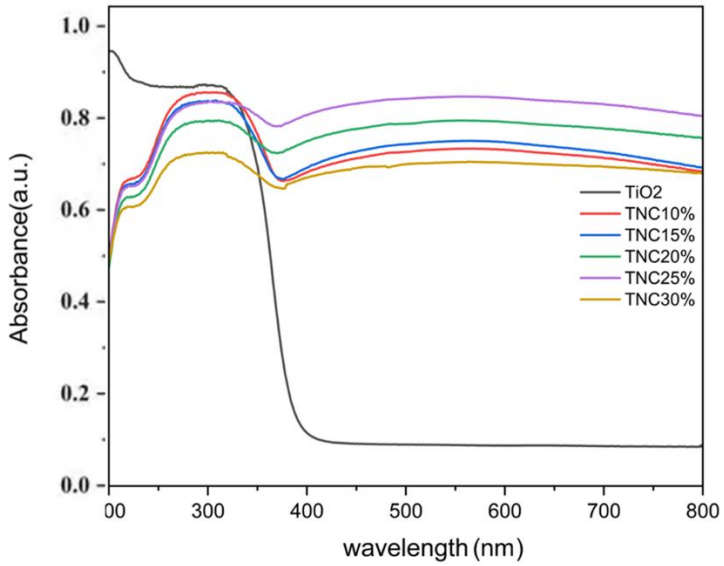

Figure 5-6 The UV-vis results of different mole ratio of composition of TNC

Figure 5-6 presents the UV-visible (UV-vis) spectrum results of samples with different mole ratios. The curves indicate a notable enhancement in the absorbance of visible light by TiO_2 upon the introduction of Ni_2O_3 into the composition. In the UV region, TiO_2 demonstrates a strong ability to absorb light. However, as the wavelength of light increases beyond 325 nm, the light absorbance decreases rapidly. Around 400 nm, the light absorption ability of TiO_2 diminishes significantly. Upon incorporating Ni_2O_3 into the composite, there is sustained high absorbance in the UV region, particularly around 300 nm. Subsequently, a gradual decrease in absorbance is observed until approximately 375 nm. Following this, there

\

is a remarkable increase in absorbance, indicative of strengthened ability to absorb visible light. The absorbance then stabilizes at a relatively high value in the visible light range. As shown in Figure 5-6, the absorbance for visible light will increase with the ratio increase of Ni_2O_3, TNC25% has the best absorbance for visible light area. However, when the ratio of Ni_2O_3 exceed 25%, the absorbance will decrease significantly. Excessive Ni_2O_3 forms large agglomerates that act as a physical barrier, obstructing incident light from reaching the underlying TiO_2 and significantly reducing its strong intrinsic UV absorption. Furthermore, these agglomerates become potent light-scattering centers, reflecting light away instead of allowing absorption. This, coupled with potential pore blockage within the TiO_2 matrix which diminishes light-trapping through internal reflection, results in a net decrease in measured absorbance across the spectrum, despite the increased visible light absorption from the excess Ni_2O_3 itself. Overall, the addition of Ni_2O_3 enhances the UV absorbance of the composite and significantly improves its ability to absorb visible light, thereby expanding its potential application in photocatalysis and other related fields.

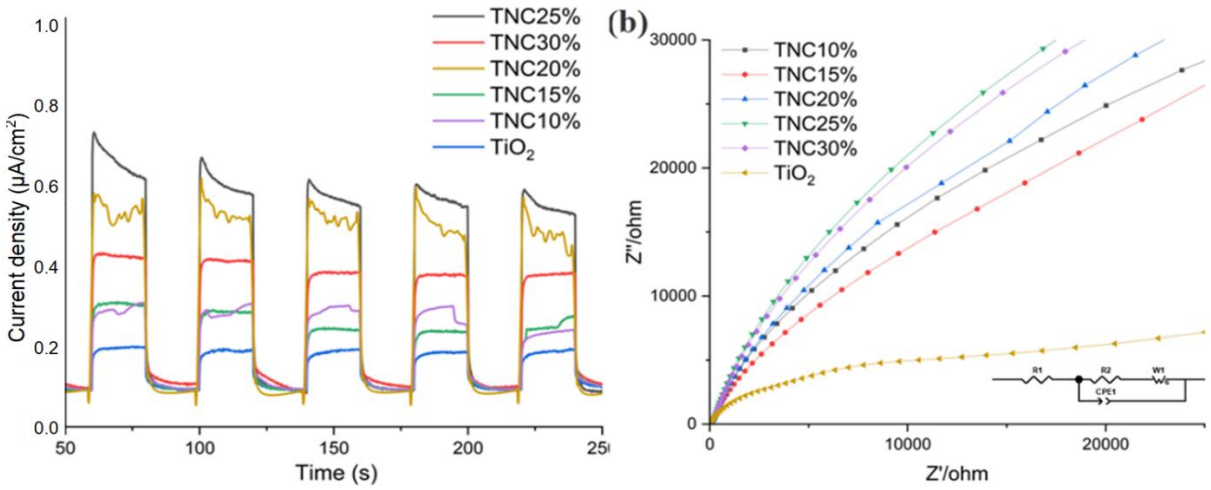

Figure 5-7 (a) Photocurrent results of different mole ratio of TNC. (b) EIS results of different mole ratio of TNC.

Table 8 The resistance of different composite of Z View equivalent curve.

Phase	R_s	R_{ct}
TiO2	6.716	428.4
10%TNC	8.352	379.5
15%TNC	7.745	323.7
20%TNC	8.515	305.8
25%TNC	9.186	271.6
30%TNC	8.216	369.2

Figure 5-7 (a) displays the photo current results, where a higher current density indicates a greater number of photo-induced electrons being generated. Due to the fast recombination of electrons and holes,

\

TiO_2 showed very limited photocurrent density. After loading Ni_2O_3 and CNT, more electrons are separated and easily to be transferred in the composite which leads to a higher photocurrent density [196-198]. Conversely, Figure 5-7 (b) represents the results of electrochemical impedance spectroscopy (EIS) with test range 0.1-100000 HZ, amplitude 10 mV, illustrating the electron transfer resistance within the composite. Using Z View software to simulate the EIS results shown in Table 8, the charge transfer resistance (R_{ct}) and solution resistance (R_s) were obtained and compared shown in Table 8. TNC25% has the smallest R_{ct} which is 271.6Ω, the improvement in conductivity owing to the existence of Ni^{3+} and CNT. In EIS, a smaller arc radius corresponds to a smaller resistance, the lower the resistance, the easier the charge transfer within the composite. More electrons transfer within the composite could enlarge the electron lifetime and make it easier to reach the surface of composite and catalysis. By combining the results of photocurrent and EIS, it can be observed that the TNC25% sample exhibits the highest current intensity and the smallest resistance. This suggests that TNC25% possesses the ability to readily induce free electrons and facilitate their transfer to the active sites within the composite. With the increase ratio of Ni^{3+}, more electrons were active and easily transferred within the composite, the decreased resistance allowed electrons rapidly reaches active spot and start catalysis. However, after the ratio of Ni^{3+} exceed 25%, the amount of electrons actived from TiO_2 were decrease which

leads to the less recombination of TiO_2 electrons and Ni_2O_3 holes. Therefore, more electrons of Ni_2O_3 were recombined with holes of Ni_2O_3, z-type heterojunction have weaker effect and photocurrent density will decrease. Overall, these findings highlight the superior performance of the TNC25% composite in terms of electron generation and transfer efficiency, underscoring its potential for applications in photocatalysis and related fields.

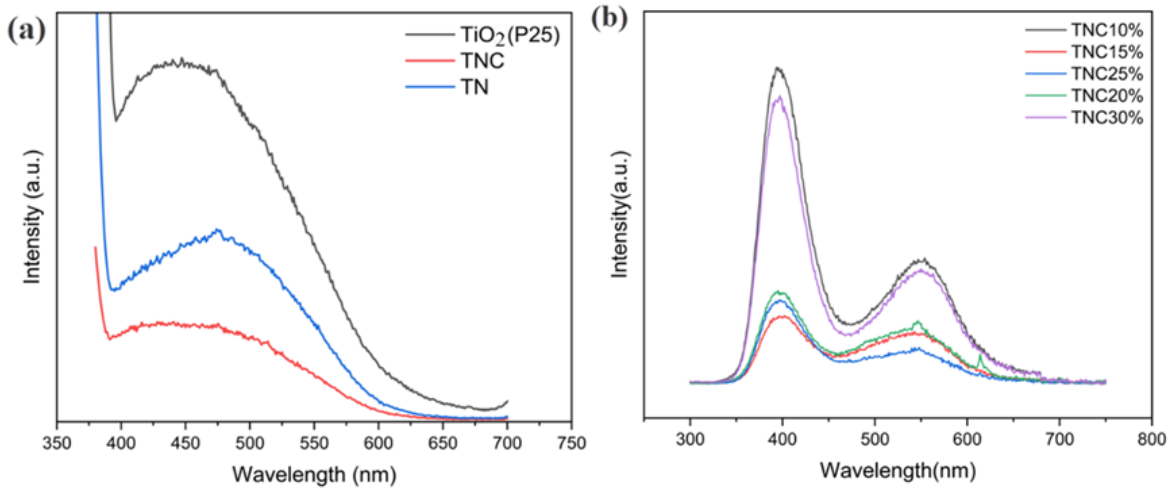

Figure 5-8 (a) PL results of different composite (TiO_2, TN and TNC). (b) PL results of TNC in different mole ratio.

Figure 5-8(a) illustrates the photoluminescence (PL) (Edinburgh FLS1000) intensity results, where a higher intensity indicates lower charge separation efficiency of electrons. Comparing the intensities of TiO_2, TN (TiO_2- Ni_2O_3), and TNC (TiO_2- Ni_2O_3/CNT)(TNC15%) samples, it can be observed that TNC exhibits the lowest PL intensity,

\

indicating the most efficient charge separation. This suggests that the incorporation of both carbon nanotubes (CNT) and Ni_2O_3 significantly enhances charge separation within the composite. Furthermore, Figure 5-8 (b) demonstrates that TNC25% and TNC15% exhibit the best charge separation performance. Specifically, within the wavelength range of 425 nm, TNC15% shows slightly better charge separation efficiency compared to TNC25%. The reason for the phenomenon is that TiO_2 is a UV sensitive material, more electrons will be activated under UV light and Ni_2O_3 has great absorbance at visible light area. Therefore at 425 nm TNC15% shows better charge separation ability than TNC25%. However, beyond 425 nm, TNC25% exhibits superior performance in charge separation. The participation of both CNT and Ni_2O_3 in the composite material leads to enhanced charge separation efficiency, with TNC25% and TNC15% demonstrating the best performance in charge separation, albeit with slightly different characteristics across different wavelength ranges. Additionally, the reason for the difference between TNC in Figure 5-9 (a) and Figure 5-10 (b) is that, the samples were not synthesized simultaneously; Figure 5-8(a) represents one experimental group, while Figure 5-8(b) corresponds to another. Furthermore, the characterization procedures were conducted at different times. Consequently, variations in the measured values may occur due to differences in experimental

\

conditions. Nonetheless, the results remain valid for intragroup comparative analysis.

5.2.3 Hydrogen generation results

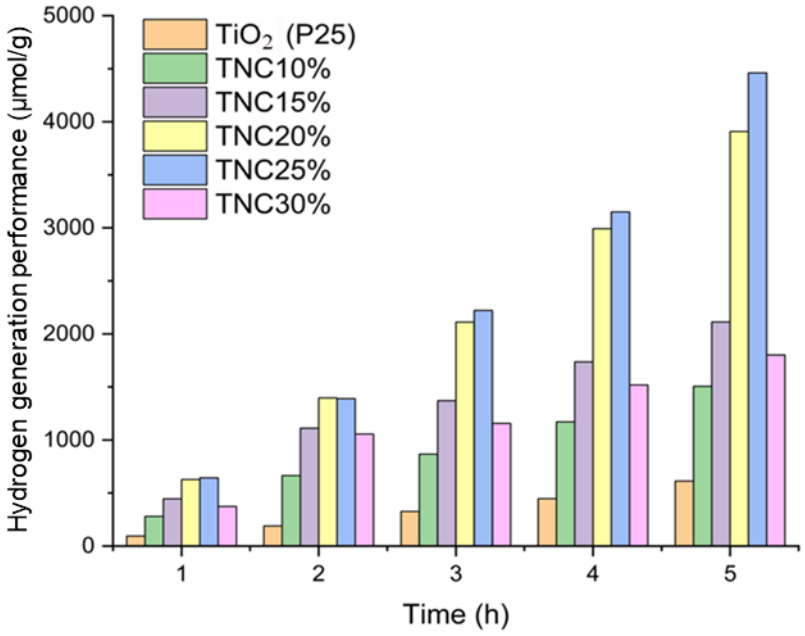

Figure 5-11 The hydrogen generation performance of different group of TNC.

Figure 5-9 illustrates the hydrogen generation performance, with TNC25% exhibiting the highest hydrogen generation rate of 4835 μmol/g. The superior performance of TNC25% can be attributed to several factors identified through characterization. Firstly, TNC25% demonstrates enhanced light absorbance across both the UV and visible light regions

compared to other compositions. This improved light absorption allows for more efficient utilization of solar power. Secondly, the composite structure of TNC25% facilitates the activation of a greater number of electrons by the collected solar power. These electrons are then easily transferred within the composite and reach the surface of Ni_2O_3, facilitating the hydrogen generation process. The hydrogen generation rate of TNC25% exhibits an increasing trend over five hours of operation. In the first hour, TNC25% generates 675 µmol/g of hydrogen, followed by 772 µmol/g in the second hour, 834 µmol/g in the third hour, and 1033 µmol/g in the fourth hour. Notably, the sample exhibited its maximum hydrogen evolution rate during the fifth hour of reaction, reaching 1,422 µmol/g·h. This value exceeds that of pure TiO_2 by more than 11-fold and is also higher than that reported for NiO/TiO_2[89], though it remains lower than those achieved by Cu/TiO_2[81] and other composite catalysts. Despite this, the material's cost-effectiveness and broad light absorption capacity demonstrate significant potential for industrial scalability. In conclusion, the exceptional hydrogen generation performance of TNC25% is attributed to its improved light absorbance, efficient electron transfer, and enhanced catalytic activity, underscoring its potential for applications in renewable energy generation.

5.2.4 Carbon footprint of the novel photocatalytic hydrogen production technology

\

By adopting the LCA methodology, carbon footprint of this hydrogen production technology based on the innovative photocatalytic catalytic was assessed. Materials consumption include all chemicals used in catalyst synthesis, while energy consumption only considers the electricity usage. Due to the scope of this study is delineated for the entire process, the treatment of wastewater was excluded. Hence, wastewater was considered as no carbon emissions at this stage. For this study, based on the guideline of Kyoto Protocol[199, 200], six greenhouse gases were taken into consideration, which include CO_2, CH_4, N_2O, HFCs, PFCs, and SF_6. It is obviously to obtain that electricity contributed to the highest carbon emissions in the whole process, which accounted for 65.1%. And then followed by triethanolamine and sodium hypochlorite. As shown in Table 10, for per gram of the photocatalyst making, 9.4mg hydrogen would be produced, and this photocatalytic hydrogen production process would emit 0.77 kg CO_2 equivalent. In other word, by adopting this novel photocatalytic hydrogen production technology, there would be 81.9kg CO_2-eq carbon emissions for producing 1kg hydrogen. The detail electricity consumption are shown in Figure 5-10 and Table 9, for Table 9, the term "light" in this context refers to the electrical energy consumption of the xenon (Xe) lamp illumination system. A magnetic stirrer was employed throughout both the catalyst synthesis and photocatalytic hydrogen evolution experiments. An oven was utilized during the synthesis stage for sample drying purposes.

\

Auxiliary equipment, including a recirculating chiller for maintaining temperature control and an ultrasonic apparatus for catalyst dispersion, was implemented during the catalytic testing phase.

The energy consumption data were systematically evaluated based on the operational protocols of both synthesis and catalysis procedures. For the catalyst synthesis, the cumulative electricity input required to produce one gram of the final catalyst material was calculated by tracking the energy consumption of all relevant apparatus throughout the synthetic sequence. Similarly, for the hydrogen production phase, the electrical energy consumption normalized to per gram of catalyst was quantified by monitoring the power input of all operational systems during the standardized catalytic reaction process.

Additionally, once the electricity light is substituted by sunlight technology, then, the electricity usage of 390 W by providing light could be saved. Hence, the comparison of CO_2 emissions of photocatalytic hydrogen can be seen as follows Table 10. By adopting sunlight, the carbon emissions could be reduced by 0.217 kg CO_2-eq per one-gram catalytic usage. Which means that there would be 58.5 kg CO_2-eq carbon emissions for producing 1kg hydrogen.

\

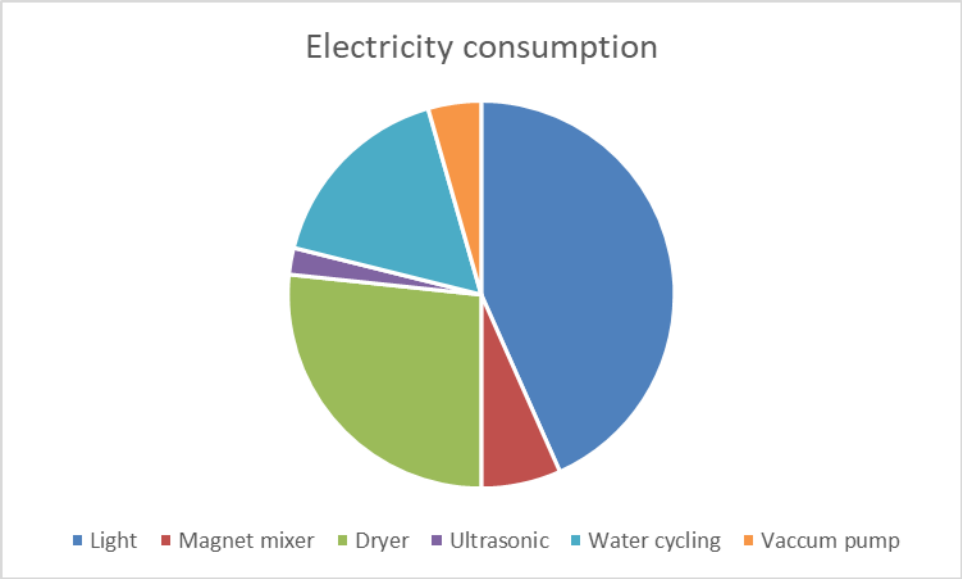

Figure 5-12 The electricity consumption for total procedure.

Table 9 Table of electricity consumption.

Total Electricity (W/h)	Light	Magnet mixer	Dryer	Ultrasonic	Water cycling	Vacuum pump
900	390	60	240	20	150	40

Table 10 Carbon emissions of the new hydrogen production method

Materials	
Indicator	**Carbon footprint (kg CO_2-eq)**
NaOH	0.003

\

NaClO	0.104	
$Ni(NO_3)_2.6H_2O$	0.005	
TiO_2	0.006	
Oxidized CNT	0.004	
$C_6H_{15}NO_3$	0.147	
Total- Materials	0.269	
Energy		
Electricity	Electricity light usage	Sunlight usage
	0.501	0.284

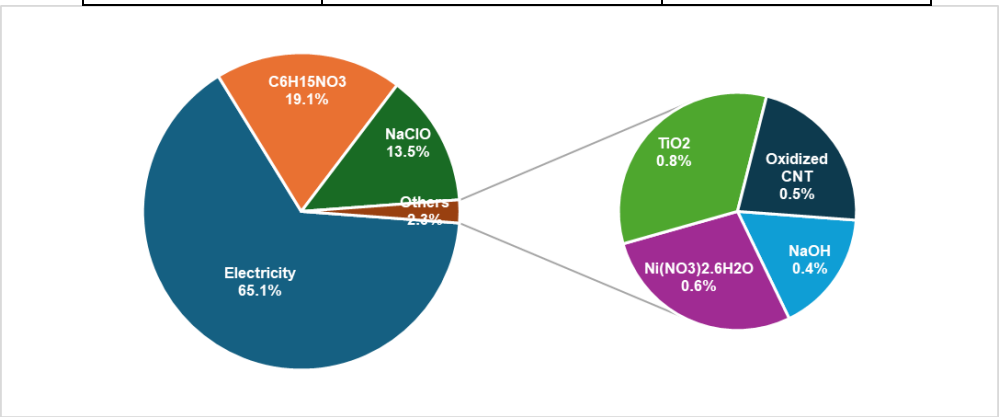

Figure 5-13. The proportion of carbon emissions for each indicator.

\

5.2.5 A comprehensive comparison of different hydrogen production technologies

Based on different environmental impact and hydrogen production process, gray hydrogen, blue hydrogen, and green hydrogen are terms used to describe different methods of hydrogen production. Gray hydrogen is produced from natural gas through a process called steam methane reforming (SMR)[201]. This process emits a significant amount of CO_2, contributing to greenhouse gas emissions. Blue hydrogen is also produced from natural gas through steam methane reforming, but with an additional step of carbon capture and storage (CCS)[202]. In this process, the CO_2 generated is captured and stored underground, preventing it from entering the atmosphere. This makes blue hydrogen a lower-carbon alternative compared to gray hydrogen. Green hydrogen is produced using renewable energy sources such as wind, solar, or hydroelectric power[203]. This method produces no carbon emissions, making green hydrogen the most environmentally friendly option.

This study mainly gives a detailed comparison of gray hydrogen, blue hydrogen, the electrolysis hydrogen, and this new photocatalytic hydrogen production technology. While the green hydrogen generation was excluded, due to the renewable energy usage is complex and data inadequate. Table 11 is a comprehensive

\

carbon emissions comparison of these methods. It indicated that the carbon emissions of blue hydrogen generation are lower than the gray hydrogen generation, this is because of the CCUS technology usage would improve the use ratio of carbon dioxide. While this novel photocatalytic hydrogen production has the highest carbon emissions with 81.91 kg CO_2-eq/kg, followed by the electrolysis hydrogen production. Both technologies are the new method, which depend mainly on the electricity usage. While this targeted technology also employed the triethanolamine to synthetic catalyst, therefore, higher than the electrolysis hydrogen. Therefore, though this technology current is the highest carbon emitter among these technologies, two suggestions are recommended to further decreased: 1. Given that the primary source of emissions stems from electricity consumption, it is proposed that power generation be transitioned to renewable energy sources. This shift would significantly reduce the carbon emissions associated with electricity generation. 2. The triethanolamine material can be made by waste recycling, which would sharply reduce carbon emissions at the same time.

Table 11 Carbon footprint comparison of different hydrogen production technologies[204].

Technologies adopted (Average)	**Carbon emissions (kg CO_2-eq)**

\

Gray hydrogen	
Coal gasification-based hydrogen	24.67
Natural gas reforming hydrogen	5.39
Methanol reforming hydrogen	8.25
Blue hydrogen	
Coal gasification-based hydrogen with CCUS	20.28
Natural gas reforming hydrogen with CCUS	0.41
Others	
Electrolysis hydrogen	59.54
This novel photocatalytic hydrogen generation	81.91

5.3 Conclusion

This research presents a novel approach to photocatalytic hydrogen generation using a cost-effective and straightforward method. The synthesis of Ni_2O_3-TiO_2/CNT composite was achieved via a simple micro-emulsion method, avoiding the use of precious metals while achieving a remarkable maximum hydrogen generation rate of 1422 µmol/g/h. Characterization techniques including X-ray diffraction (XRD), high-resolution transmission electron microscopy (HRTEM), X-ray photoelectron spectroscopy (XPS), UV-visible spectroscopy (UV-vis), photocurrent, photoluminescence (PL), and electrochemical impedance

\

spectroscopy (EIS) were employed to elucidate the morphology, structure, and optical properties of the composite. TNC25% was identified as the most active composition, surpassing the performance of TiO_2 by generating hydrogen at a rate more than eleven times higher. Furthermore, Ni_2O_3 demonstrated excellent potential as a co-catalyst, enhancing light absorption and charge separation within the composite. As a nickel-based material, Ni_2O_3 holds promise for future applications in the development of cost-effective metal-based hydrogen generation catalysts. For producing 1kg H_2, the total carbon footprint of this novel photocatalytic hydrogen process is 81.91 kg CO_2-eq/kg. The carbon emissions can be further reduced by using renewable energy power generation, and waste-recycling triethanolamine. Overall, this study presents a significant advancement in the field of photocatalytic hydrogen generation, offering a low-cost and efficient alternative for renewable energy production. The insights gained from the characterization of the Ni_2O_3-TiO_2/CNT composite pave the way for further exploration and optimization of novel catalyst materials for sustainable hydrogen generation.

\

6 Chapter 6. Hydrogen evolution reaction of core-shell Ni/NiO/Ni_2O_3/TiO_2-CNT composites

6.1 Introduction

Nickel-doped composites have shown great promise in photocatalytic hydrogen generation due to their ability to enhance light absorption, charge separation, and catalytic efficiency. In photocatalytic hydrogen production, the composite materials utilize solar energy to drive the water splitting reaction, producing hydrogen as a clean fuel. The incorporation of nickel as a dopant into semiconducting materials, such as titanium dioxide (TiO_2), enables the modification of electronic structures, improving the light-harvesting capabilities and enhancing the material's charge carrier dynamics. Nickel doping helps facilitate faster electron transfer, reduces charge recombination, and increases the number of active sites for proton reduction, thereby improving the overall efficiency of hydrogen evolution. Additionally, nickel's role in promoting surface reactions and its ability to lower activation energy make it an effective cocatalyst for accelerating the hydrogen production process. These nickel-doped composites, combining the benefits of semiconductors and metallic catalysts, represent a promising avenue for developing high-performance, cost-effective photocatalysts for sustainable hydrogen generation from water. For Nickel oxide (NiO), it has suitable bandgap and ability to absorb visible light, makes it an attractive material for efficient photocatalysis. NiO's ability to act as

\

both a cocatalyst and a photocatalyst enhances the hydrogen evolution reaction (HER) by promoting electron transfer and reducing charge recombination, which is often a limiting factor in photocatalytic processes. Furthermore, NiO can effectively support water oxidation and aid in the generation of reactive oxygen species, thus facilitating the overall water splitting process. Despite its promising characteristics, the performance of NiO in photocatalysis is often limited by its relatively low conductivity and slow charge carrier mobility. However, strategies such as doping, heterojunction formation, and composite material design are being explored to further enhance the photocatalytic activity of NiO, making it a highly promising candidate for sustainable hydrogen production from water under visible light. Therefore, in this chapter, a multi-layer structure of Ni/NiO/Ni_2O_3 nano particles was investigated to enhance the catalysis process, combining the effect of metal doped surface and band engineering to optimize the electron transfer path, increase the charge transfer and restrain the recombination of electrons and holes.

6.2 Results and discussion

\

6.2.1 Morphology and physical results

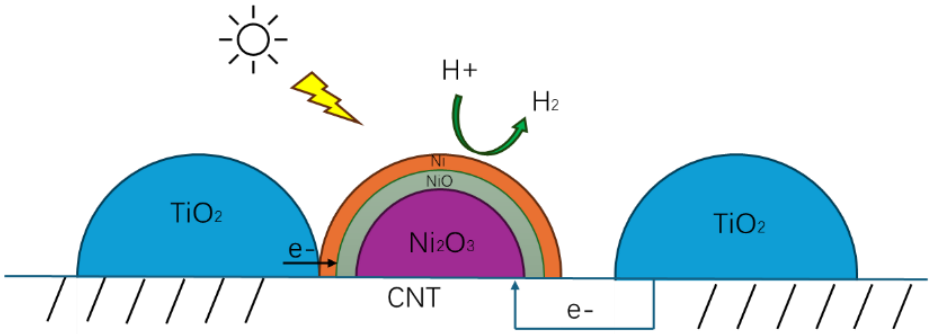

Figure 6-1 The scheme of catalyst structure and electron transfer directions.

As proved in chapter 5, the electrons transfer path is from TiO_2 to CNT then to the surface of Ni_2O_3 and catalysis H^+ TO hydrogen. TNC800 included a 800 ℃ calcination in 10%H_2 and 90% Ar atmosphere which aimed to reduce the Ni_2O_3 to nickel metal and nickel oxide. Figure 6-1 shows the catalyst structure. There are two main conditions of electrons transferring, when the surface of TiO_2 nano particles contact the surface of core-shell particles, the electrons transfer directly from TiO_2 to Nickel metal at the shell. When TiO_2 nano particles have no contact with Ni_2O_3 nano particles, the electrons transfer through carbon nano tubes and from Ni_2O_3 core to nickel shell. In order to investigate the existence of Ni^{2+} and Ni, XPS was applied to the catalyst.

\

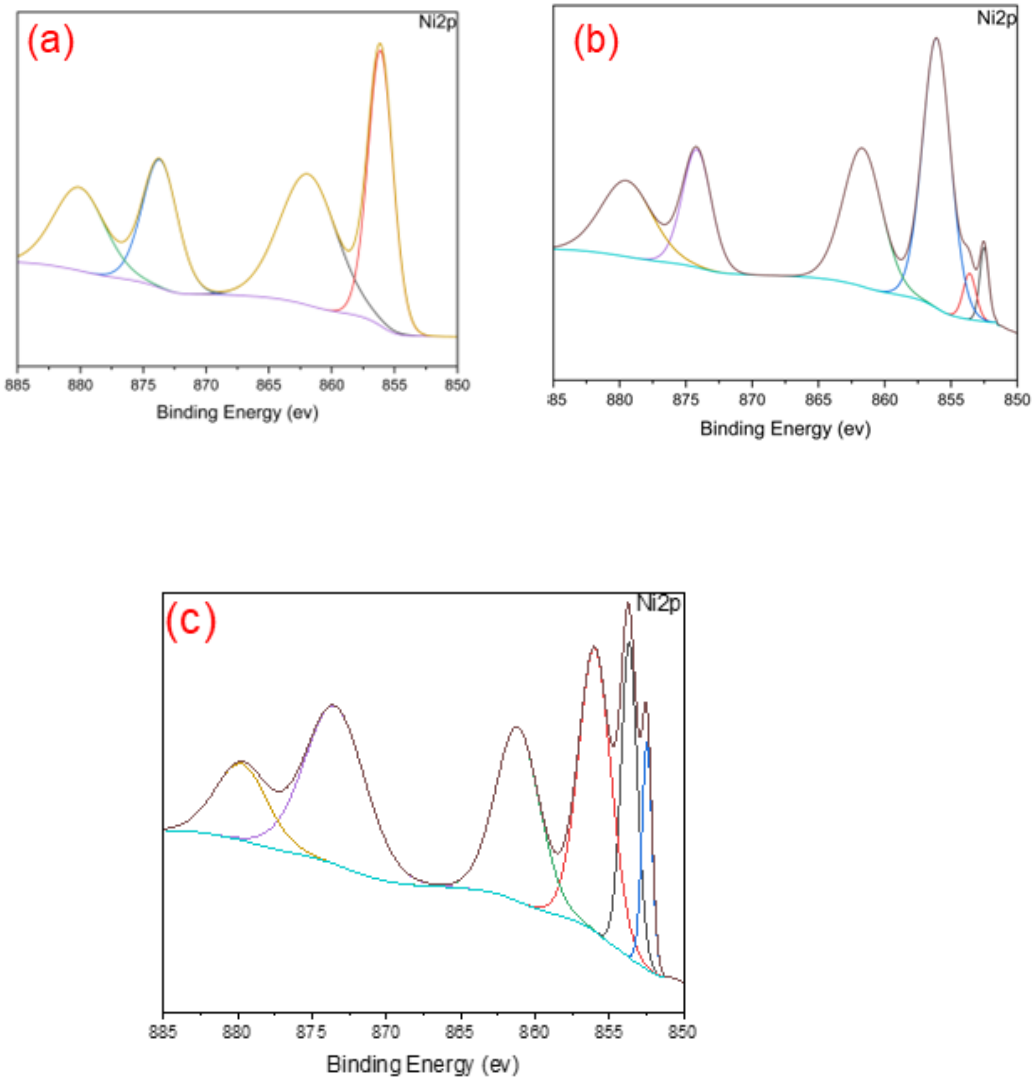

Figure 6-2. XPS results of Ni2p of (a) TNC (b) TNC800 (c) TNC800-2

For the detail element state in the composite, XPS was taken. Figure 6-2 shows the Ni 2p spectrum of TNC, TNC800 and TNC800-2. For Figure 6-2 (a), there is 4 main peaks positioned at 855.4 eV, 873.4 eV correspond to Ni 2p3/2 and Ni 2p1/2, 861.2 eV, 879.0 eV corresponding to satellite peaks. These four peaks support the

\

existence valance of Ni as Ni_2O_3. For TNC800 results, two more peaks at 853.6ev and 852.5ev can be observed. It is reported that the peak at 853.6ev corresponding to Ni^{2+} and 852.5ev corresponding to Ni^0[205, 206]. The spectrum results of TNC800-2 support the presence of Ni^{2+} and Ni^0, as the calcination time increased, more Ni^{3+} transferred to Ni^{2+} and Ni^0 which shown as two high peaks at 853.6ev and 852.5ev compare to Figure 6-2(b). The absolute numerical values on the y-axis (counts per second, CPS) of an XPS spectrum are not intrinsically meaningful for direct quantitative comparison between different samples or instruments. This is because the raw intensity is a function of numerous experimental variables, including the specific X-ray source flux, analyzer transmission function, detector efficiency, and the geometry of the excitation and detection relative to the sample surface.

\

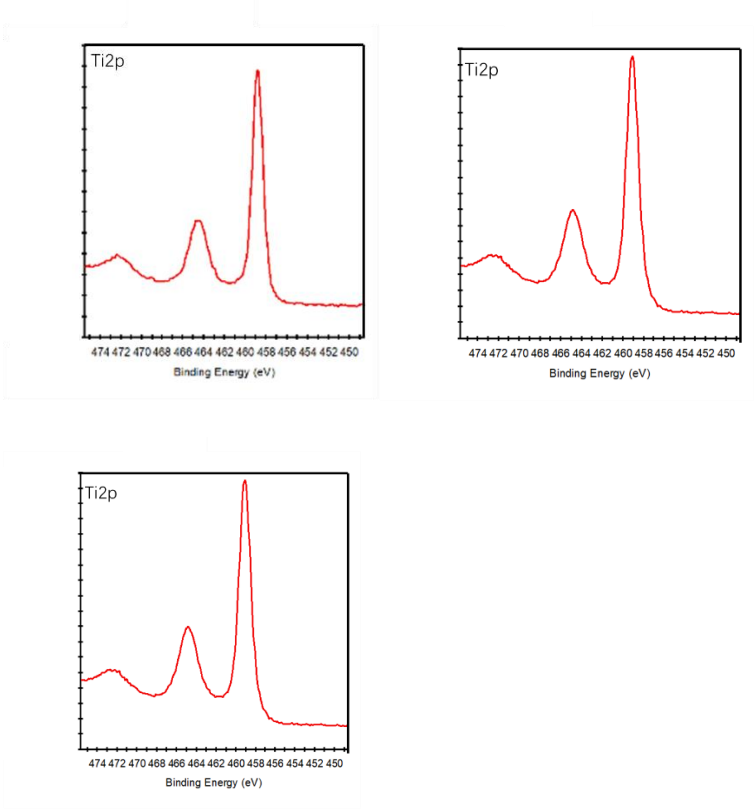

Figure 6-3 XPS results of Ti2p of (a) TNC (b) TNC800 (c) TNC800-2

For Ti2p, the peaks at 458.6 eV and 464.2 eV, corresponding to Ti 2p3/2 and Ti 2p1/2, respectively. By comparing Figure 6-3 (a)(b)(c), it can be summarized that the reduction temperature of Ti^{4+} is higher than 800 degress, therefore, the valance Ti wasn't influenced.

\

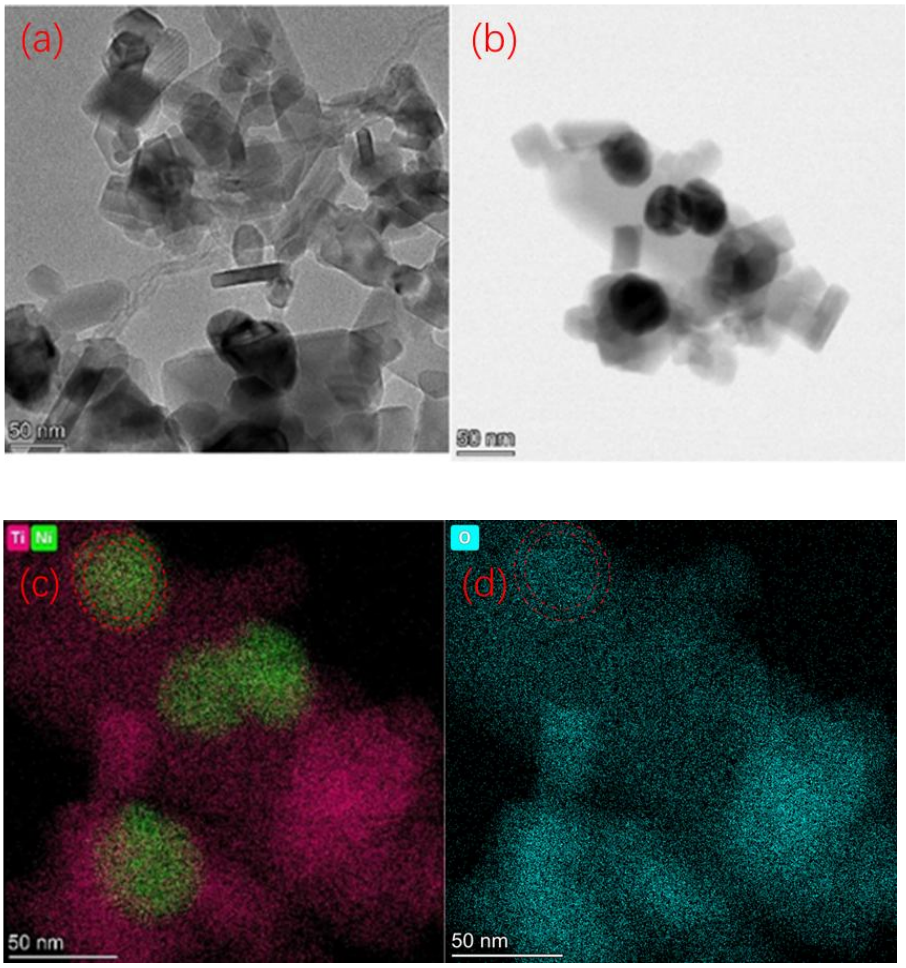

Figure 6-4(a)(b) HRTEM results of TNC800. (c) EDS mapping results of Ti and Ni. (d) EDS mapping results of O element

To characterize the core-shell structure, HRTEM and EDS analyses were performed. As depicted in Figure 6-4(a) and (b), elemental distribution profiles of Ni and O were compared to identify compositional differences across distinct layers. According to the core-shell identification method of Gong, et al [154], they used the ratio difference of oxygen in shell and core to identify the structure. In this research, the outermost layer, consisting of metallic Ni, is expected to

exhibit minimal oxygen content, corresponding to reduced signal intensity (light blue regions) in Figure 6-4(d). The intermediate layer (NiO) should demonstrate increased oxygen concentration. The core, identified as Ni_2O_3, is anticipated to display the highest oxygen abundance, manifesting as enhanced signal intensity and clarity in elemental maps. However, the multilayer configuration of NiO_x particles remains indistinct in Figure 6-4(d). This ambiguity arises from TiO_2 substrate interference, wherein its substantial oxygen content elevates the background signal in EDS mapping. Consequently, resolving oxygen signatures specific to NiO_x is impeded by this significant spectral interference

6.2.2 Photo-electron results

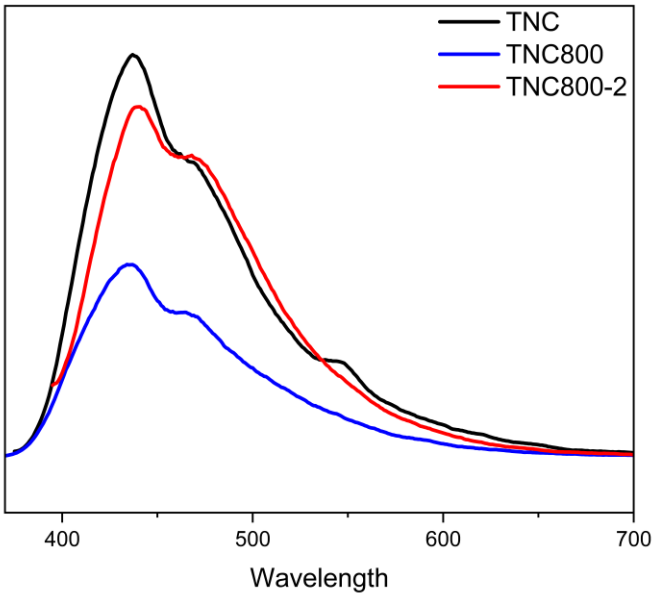

\

(a)

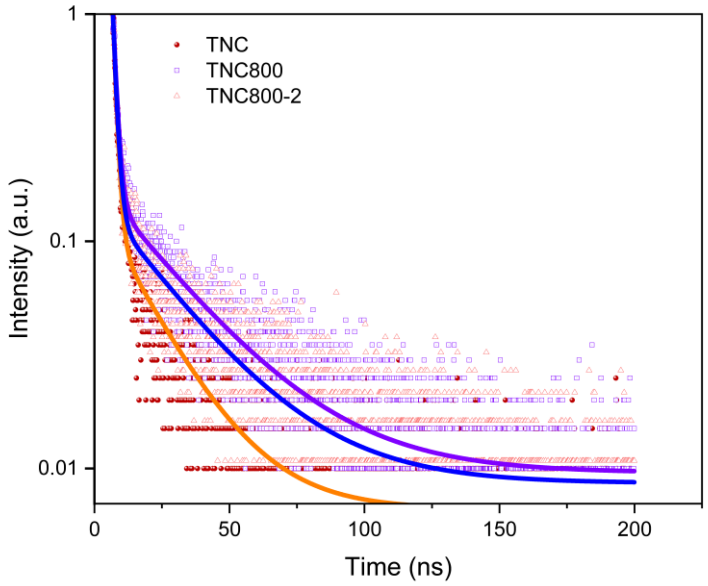

(b)

Figure 6-5 (a) PL results of TNC, TNC800, TNC800-2. (b) TRPL results of TNC, TNC800, TNC800-2

Table 12 The fit cuve equation and kinetic factors.

Model	ExpDec2		
Equation	y = A1*exp(-x/t1) + A2*exp(-x/t2) + y0		
Plot	TNC	TNC800	TNC800-2
y0	0.00663 ± 3.30418E-4	0.00957 ± 5.48198E-4	0.00862 ± 4.7017E-4
A1	202.6501 ± 14.49388	120.34984 ± 9.75698	161.64255 ± 12.76045
t1	1.25966 ± 0.016	1.38842 ± 0.02164	1.30925 ± 0.0188
A2	0.14303 ± 0.00561	0.1765 ± 0.00432	0.1529 ± 0.00411
t2	18.67992 ± 0.65342	28.65477 ± 0.82661	26.84727 ± 0.81769
Reduced Chi-Sqr	1.26859E-4	2.32105E-4	1.85807E-4
R-Square (COD)	0.97044	0.95878	0.96158
Adj. R-Square	0.97038	0.95869	0.9615

\

Figure 6-5 shows the photoluminescence (PL) intensity results, which indicates the charge separation performance, the higher the intensity, the lower the charge separation of composites. TNC800 has the best charge separation performance, TNC800-2 and TNC has the similar value. The carrier lifetime of different composite was characterized by TRPL. From TRPL results, TNC800 has the longest carrier lifetime which is 2.18ns, TNC800-2 is 1.80ns, TNC is 1.44ns. The calculation equation is shown in equation 9,

$$\tau_{ave} = (A_1{\tau_1}^2 + A_2{\tau_2}^2)/(A_1\tau_1 + A_2\tau_2) \qquad \textit{Equation 9}$$

The curve equation and kinetic factors is in Table 12, put A_1, A_2, τ_1 and τ_2 from the table into the equation to get the average fly time. τ_1 and τ_2 correspond to the *t_1* and *t_2* in Figure 6-5(b). It can be summarized from the PL results is that the involvement of Nickel atom and NIO significantly increase the electron lifetime and decrease the recombination electrons and holes. Meanwhile, The formation of a p-n heterojunction between titanium dioxide (TiO_2) and nickel oxide (NiO) is driven by their intrinsic semiconductor characteristics and favorable band alignment. TiO_2, an archetypal n-type semiconductor due to its inherent oxygen vacancies, exhibits a Fermi level close to its conduction band. In contrast, NiO, a well-established p-type semiconductor resulting from nickel vacancies, possesses a Fermi level

near its valence band. Upon contact, charge redistribution occurs to achieve Fermi level equilibration: electrons diffuse from TiO_2 to NiO, while holes transfer in the opposite direction. This process creates a built-in electric field across the interface, directed from TiO_2 to NiO, and induces band bending in the space charge region. This interfacial electric field effectively facilitates the spatial separation of photogenerated charge carriers—electrons migrate toward the n-side (TiO_2) and holes toward the p-side (NiO)—thereby suppressing recombination and significantly enhancing photocatalytic performance.

XPS analysis show in Figure 6-2 reveals that the Ni^0/Ni^{2+} ratio increases with calcination time and the decrease of Ni_2O_3, as determined by quantitative assessment of the respective peak areas. The TNC800-2 sample exhibits the highest Ni^0/Ni^{2+} ratio. Consistent with Figure 6-5, the presence of Ni^0 and Ni^{2+} enhances charge separation and extends electron lifetime; however, these properties diminish when Ni^0 and Ni^{2+} concentrations exceed an optimal threshold. This decline primarily results from reduced Ni_2O_3 content, given that charge separation predominantly occurs at the TiO_2/Ni_2O_3 interface. Concurrently, the increasing Ni/NiO ratio modifies the material's band structure.

\

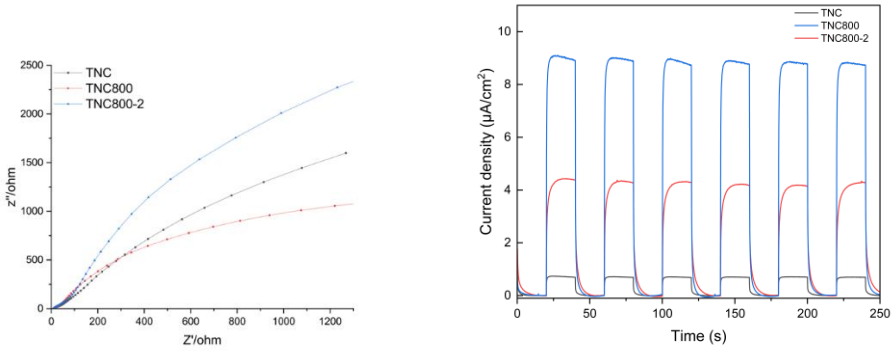

Figure 6-6 (a) EIS results of TNC, TNC800 and TNC800-2. (b) Photocurrent results of TNC, TNC800 and TNC800-2

Figure 6-6 illustrated the electro characters of TNC, TNC800 and TNC800-2 includes EIS and photocurrent results. EIS results analyzed the electron transfer resistance in the composite. The higher the arc radius of the curve represents the higher charge transfer resistance. From Figure 6-6(a), TNC800 has the lowest charge transfer resistance which corresponds to the existence of Ni metal. However, as mentioned, the conductivity of NiO is relatively low, therefore, when the content of NiO increase, the resistance of composite increases. That's the reason why TNC800-2 has a weaker performance than TNC. As shown in Figure 6-6 (b), TNC800 and TNC800-2 demonstrated a significant enhancement in photocurrent than TNC. The lower transfer resistance and higher charge separation contributes to the bigger value of current density.

\

The ratio of metallic Ni to NiO plays a critical role in modulating the charge transfer pathways at the TiO_2-based interface, significantly influencing the photocatalytic efficiency. A higher proportion of metallic Ni facilitates the formation of Schottky junctions at the TiO_2/Ni interface, acting as electron sinks that promote the direct migration of electrons from the conduction band of TiO_2 to Ni. This enhances electron-hole separation but may favor backward charge transfer or shield active sites if excessive. Conversely, a dominant NiO phase establishes a p-n heterojunction with n-type TiO_2, where the built-in electric field drives the separation of carriers—electrons flow toward TiO_2 and holes toward NiO—resulting in more spatially separated and energetically favorable charge distribution. However, an optimal balance between Ni and NiO is crucial: excessive NiO can introduce interfacial defects acting as recombination centers, while disproportionate Ni may weaken the heterojunction effect and impede hole extraction. Thus, the Ni/NiO ratio directly governs the competition between Schottky-mediated electron trapping and p-n junction-driven charge separation, ultimately determining the overall efficacy of photocatalytic reactions [207].

6.2.3 Hydrogen generation results

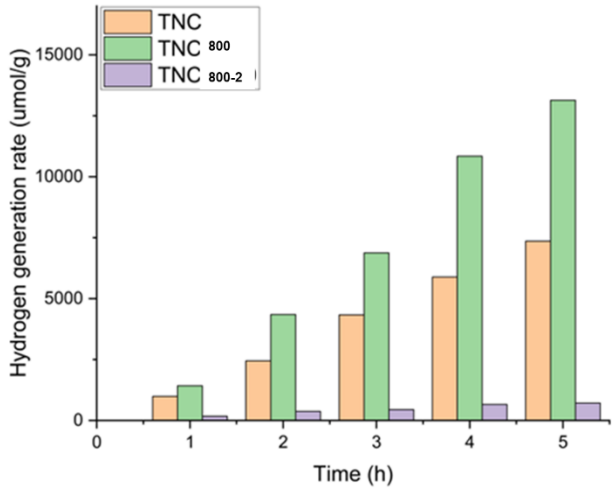

Figure 6-7 Photocatalysis hydrogen evolution performance of TNC, TNC800 and TNC800-2

Figure 6-7 illustrates the hydrogen generation rate of TNC, TNC800 and TNC800-2. TNC800 shows significant improvement than TNC whose average hydrogen generation rate reaches 2626μmol/g/h which is more than two times generation rate than TNC. The improvement of hydrogen generation rate belongs to the lower transfer resistance, higher charge separation and longer carrier lifetime, which obeys the photo-electro characterization results. The average hydrogen generation rate of TNC800-2 is 143.7μmol/g/h, this observed reduction in performance may be attributed to the diminished presence of Ni_2O_3. As the relative ratio of metallic Ni to NiO increases, a greater proportion of photogenerated electrons are transferred directly from the conduction band of TiO_2 to NiO and Ni, thereby bypassing the Z-scheme charge transfer pathway.

\

This alteration in carrier dynamics results in a less effective Z-scheme band alignment and reduced overall light absorption. Although both Ni and NiO contribute positively to electron-hole separation, the detrimental effects of the compromised Z-scheme structure and attenuated photon utilization outweigh these benefits, leading to a net decrease in photocatalytic activity.

The observed marginal discrepancy in the photocatalytic performance of the TNC sample between Chapter 6 and Chapter 5 may be attributed to modifications in the experimental setup between the two study phases. Specifically, the vacuum grease blocked in the tube was washed, therefore, clearing of the gas transmission tubing were implemented to enhance system integrity and gas diffusion homogeneity. These improvements likely promoted more uniform distribution of evolved gases within the closed system, thereby facilitating more consistent sampling and detection by gas chromatography (GC). As a result, the measured hydrogen evolution rate in Chapter 6 exhibited a slight increase compared to that reported in Chapter 5, reflecting improved gas transfer efficiency from the reactor to the detection system rather than a fundamental change in the catalytic activity.

\

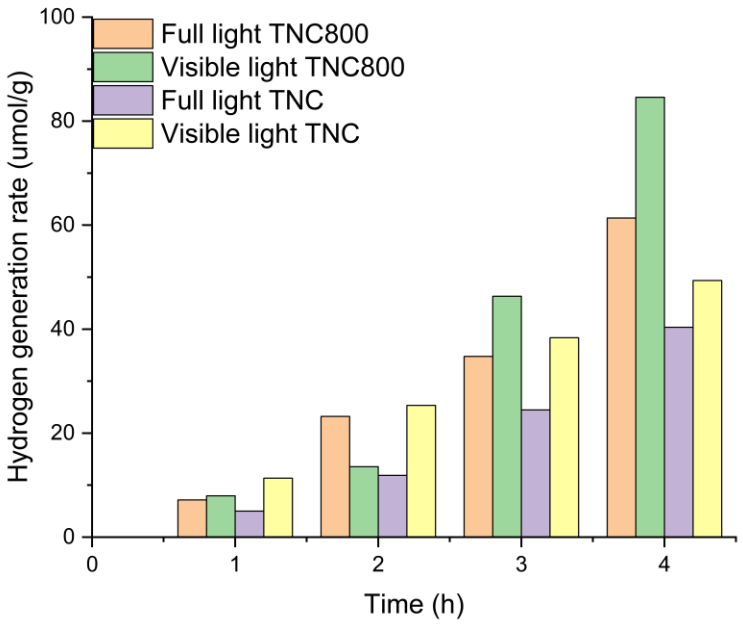

Figure 6-8 Hydrogen generation rate of TNC and TNC800 under full light and visible light.

Another interesting scene is the enhanced behavior under visible light range (λ>420nm) of TNC and TNC800. As shown in figure 6-8, in ph=7 environment, both TNC and TNC800 generated more hydrogen in visible light area than full light. The reason for this phenomenon is that, as mentioned in chapter 6, the participation of Ni_2O_3 significantly improves the absorbance of composite on visible light area. Moreover, the increasement in charge transfer and separation enlarge the electron active time and restrain the recombination of electrons and holes. These characters significantly improve the catalytic performance in visible light area.

\

6.3 Conclusion

By introducing Ni metal and NiO in TNC photocatalyst, the electro-photo characters has been optimized significantly. Ni_2O_3 reduced to Ni metal and NiO at 800 ℃, provide a core-shell structure of nickel as outer shell, NiO as the second layer and Ni_2O_3 as core. The structure improve the electron transfer efficiency and enhance the charge separation and carrier life time. PL intensity is influenced by external factors such as instrument status and sample optical effects, making it unsuitable for direct quantitative comparison and generally serving only as a qualitative reference. Fluorescence lifetime is an intrinsic parameter of the luminescent state and is not affected by the aforementioned factors. Therefore, TRPL lifetime measurements are considered a reliable method for the quantitative analysis of charge carrier dynamics. From TRPL results, the electron lifetime increased from 1.44ns to 2.18ns. The enhancement in photo-electro characters directly reflect to the catalysis performance which is photocatalysis generation rate, the average generation rate was remarkably increased from 1471.5μmol/g/h (TNC) to 2626.7μmol/g/h(TNC800). Furthermore, when the calcination time increased to 2hours, the ration of nickel and NiO increased, the catalytic performance decreased from 2626.7μmol/g/h to 143.7μmol/g/h, indicating the importance of Ni_2O_3.

\

7 Chapter 7. Conclusions and recommendations for future work

7.1 General conclusion

This thesis focuses on the high-quality preparation of nickel trioxide-based materials and their application in photocatalytic hydrogen production. Building upon existing conventional methods, we integrated and optimized microfluidic technology, significantly reducing preparation time and offering a novel, promising approach for industrial-scale production and uniform high-quality synthesis. We designed a noble-metal-free, highly efficient photocatalyst that substantially increased hydrogen yield while addressing the limitations of titanium dioxide, including its poor light absorption and rapid electron-hole recombination. By constructing Z-scheme heterojunctions and core-shell structures, we optimized electron transfer pathways, extended electron lifetimes, and improved hydrogen production efficiency, offering insights for future low-cost hydrogen generation. Although the characterization can't be analyzed out of the group due to sample inconsistency and other effects, the results still valid for inner group analyze. The microfluidic synthesis approach was not employed for the preparation of the composite due to the presence of suspended TiO_2 nanoparticles and carbon nanotubes (CNTs) in the precursor solutions. These solid components pose a high risk of channel clogging, which

\

would compromise the reproducibility and continuous-flow operation essential to microfluidic processes.

Details are listed below:

(1) **Centrifugal microfluidic synthesis of Ni_2O_3 nanoparticles.** This study explores the synthesis of Ni_2O_3 nanoparticles using centrifugal microfluidics, which enhance the mixing and synthesis efficiency. The results demonstrate that rotational speed and reaction duration are key factors in reducing particle size and narrowing the size distribution. Conversely, increased rotational acceleration leads to larger particle sizes and a wider size distribution

(2) **Photocatalytic hydrogen evolution of TiO_2- Ni_2O_3/CNT heterojunctions.** This research introduces an efficient and low-cost method for photocatalytic hydrogen generation by synthesizing a Ni_2O_3-TiO_2/CNT composite through a simple micro-emulsion process, without the need for precious metals. The composite achieved a remarkable hydrogen generation rate of 1422 μmol/g/h. Various characterization techniques, including XRD, HRTEM, XPS, UV-vis, photocurrent, PL, and EIS, were used to analyze the composite's morphology, structure, and optical properties. The Ni_2O_3-TiO_2/CNT composite, particularly the TNC25% composition, outperformed TiO_2 (P25), generating hydrogen at over eleven times the rate. Ni_2O_3 was found to enhance light absorption and charge separation,

demonstrating its potential as a co-catalyst. Additionally, the process showed a carbon footprint of 81.91 kg CO_2-eq/kg for producing 1 kg of H_2, with further reductions possible through renewable energy and waste-recycling techniques. This work offers a promising, cost-effective approach to photocatalytic hydrogen generation and provides valuable insights for optimizing catalysts in sustainable hydrogen production.

(3) **Adding Ni metal and NiO into the TNC photocatalyst significantly enhanced its electro-photo properties**. Reduction of Ni_2O_3 to Ni metal and NiO at 800°C resulted in the formation of a core-shell structure, with Ni as the outer shell, NiO as the intermediate layer, and Ni_2O_3 as the core. This structure improved electron transfer efficiency, charge separation, and carrier lifetime, with the electron lifetime increasing from 1.44 ns to 2.18 ns. These improvements in the photo-electrochemical characteristics directly translated into enhanced photocatalytic performance, with the hydrogen generation rate increasing from 1471.5 μmol/g/h (TNC) to 2626.7 μmol/g/h (TNC800). However, extending the calcination time to 2 hours resulted in an increased ratio of Ni and NiO, which led to a decline in catalytic performance, reducing the hydrogen generation rate to 143.7 μmol/g/h. This underscores the critical role of Ni_2O_3 in optimizing photocatalytic efficiency.

\

7.2 Recommendation for future work

The current research was based on z-scheme heterojunction to optimize the electron transfer path meanwhile increase the carrier lifetime to increase the photocatalysis hydrogen generation performance. However, due to the core-shell particles diameter and structure restrictions, the contact surface of main catalyst and co-catalyst is quite limited. To increase the active point and contact surface between catalysts, Ni_2O_3 are more recommended to be added as plate or other multi-layer structures. Reducing Ni_2O_3 by heat treatment to doped Nickel single atoms on the surface to increase catalysis efficiency. Formed functional multi-layer structure could be a great improvement in the photo-electro characters. Furthermore, the reduction of Ni_2O_3 and TiO_2 could be applied at the same time at a relative high temperature, for example 1500 ℃ to create oxygen vacancy in TiO_2 crystal structure then induce nickel single atom to improve the conductivity and electrons separation.

For microfluidic synthesis of nano particles, even composites, a more complex continuous flow system should be invented instead of a fixed microfluidic chip. As microfluidic chips are commonly used as detective and test samples which require very limited amounts of samples. However, for nanoparticles synthesis, the product is required to be synthesized at a higher numerical level. Therefore, continuous flow microfluidic system could generate nano particles at a constant

\

production rate which benefits industry or large amount synthesis. Furthermore, if possible, a much more complex microfluidic chip should be created to direct one step synthesis of composite for example, design more chambers to contain different reactants, valves to control the reaction steps and chemicals release orders, more layers could be added to separate the products and wastes. Left only heat treatment for applied after microfluidic synthesis.

\

References:

1. Alfaifi, B.Y., et al. *Photoelectrochemical solar water splitting: From basic principles to advanced devices*. 2018.
2. Bowker, M., *Sustainable hydrogen production by the application of ambient temperature photocatalysis.* Green Chemistry, 2011. **13**(9): p. 2235-2246.
3. Albadani, A., M. Hassan, and F. Obaid, *Kinetic study of factor affecting the reaction of cyanide and picrate ions in the presence of micellar catalyst.* 2022. **8**: p. 136-143.
4. Mohsin, M., et al., *Prospects, challenges, and opportunities of the metals-modified TiO_2 based photocatalysts for hydrogen generation under solar light irradiation: A review.* FlatChem, 2023. **42**: p. 100547.
5. Elbanna, O., et al., *TiO_2 mesocrystals composited with gold nanorods for highly efficient visible-NIR-photocatalytic hydrogen production.* Nano Energy, 2017. **35**: p. 1-8.
6. Yang, L., et al., *A surface modification resultant thermally oxidized porous g-C_3N_4 with enhanced photocatalytic hydrogen production.* Applied Catalysis B: Environmental, 2017. **204**: p. 335-345.
7. Chang, Y., et al., *Ternary CdS/Au/3DOM-$SrTiO_3$ composites with synergistic enhancement for hydrogen production from visible-light photocatalytic water splitting.* Applied Catalysis B: Environmental, 2017. **215**: p. 74-84.
8. AlSalka, Y., O. Al-Madanat, and A. Hakki, *TiO_2-based photocatalytic hydrogen production: How to transfer it to an applicable approach?* Applied Catalysis A: General, 2023. **662**: p. 119287.
9. Li, H., et al., *Turbulence enhanced ferroelectric-nanocrystal-based photocatalysis in urchin-like TiO_2/$BaTiO_3$ microspheres for hydrogen evolution††Electronic supplementary information (ESI) available. See DOI: 10.1039/d1na00331c.* Nanoscale Advances, 2021. **3**(19): p. 5618-5625.
10. Rakibuddin, M. and H. Kim, *Samarium (III)-doped ZnO/graphitic−C_3N_4 composites for enhanced hydrogen generation from water under visible light photocatalysis.* Journal of Alloys and Compounds, 2020. **832**: p. 154887.
11. Matawale, R., et al., *Enhanced energy storage and solar hydrogen generation via Mg-VO_2@ZnO-MWCNT composites.* Inorganic Chemistry Communications, 2025. **173**: p. 113875.
12. Sadiq Mohamed, M.J. and M.A. Gondal, *Nanostructured defects-rich black-ZnO/biowaste-derived carbon composites for efficient visible light-driven hydrogen generation: A study on the role of C–Zn@C–O–Zn interface.* International Journal of Hydrogen Energy, 2024. **92**: p. 47-58.
13. Pratiwi, R., et al., *Development of CdS/TNTA nanocomposite to improve performance of simultaneous electrocoagulation-photocatalysis process for hydrogen production and ciprofloxacin elimination.* Materials Science for Energy Technologies, 2025. **8**: p. 121-130.
14. Vargas, R., et al., *Simultaneous p-nitrophenol remediation and hydrogen generation via dual-function photoelectrolytic cell: P–TiO_2 photoanode and CuP cathode.* International Journal of Hydrogen Energy, 2024. **59**: p. 159-167.

15. Baghsiyahi, F.B. and M. Yeganeh, *The theoretical investigation of the electronic and optical properties of Fe-doped anatase TiO_2.* Solid State Communications, 2025. **396**: p. 115758.
16. Lukong, V.T., et al., *The development and application of Cu@TiO_2@$SAPO_{-34}$ as better photocatalyst towards degradation of various pollutants.* Environmental Technology & Innovation, 2024. **35**: p. 103700.
17. Ruzimuradov, O., et al., *Structural and optical properties of sol-gel synthesized TiO_2 nanocrystals: Effect of Ni and Cr (co)doping.* Optical Materials, 2023. **143**: p. 114203.
18. Ida, S., et al., *Facile synthesis of black N-TiO_2 / N-RGO nanocomposite for hydrogen generation and electrochemical applications: New insights into the structure-performance relationship.* Applied Surface Science Advances, 2022. **9**: p. 100249.
19. Li, Y., et al., *A 3D C@TiO_2 multishell nanoframe for simultaneous photothermal catalytic hydrogen generation and organic pollutant degradation.* Journal of Colloid and Interface Science, 2022. **609**: p. 535-546.
20. Jin, Z., et al., *Constructing tightly integrated 2D conductive metal-organic framework/TiO_2 S-scheme heterostructure by chemical bonds for photocatalytic hydrogen evolution.* International Journal of Hydrogen Energy, 2025. **99**: p. 785-792.
21. Gao, M., et al., *Functionalization of TiO_2 Nanofibers with Ag and Ag_2S Nanoparticles for Enhanced Photocatalytic Hydrogen Generation.* Procedia Engineering, 2017. **215**: p. 188-194.
22. Kuru, T., et al., *Rational design of ZnO/$SrTiO_3$ S-scheme heterojunction for photo-enhanced piezocatalytic hydrogen production.* Applied Surface Science, 2025. **682**: p. 161704.
23. Rasheed, H.M., et al., *A review on modified ZnO to address environmental challenges through photocatalysis: Photodegradation of organic pollutants.* Materials Today Energy, 2025. **48**: p. 101774.
24. Suo, R., et al., *A Z-scheme heterojunction constructed by ZnO/$CeVO_4$ for high active photocatalytic hydrogen production.* Journal of Rare Earths, 2024.
25. Zakariyya, Y., et al., *Recent trends and optimization strategies for CdS-based photocatalysts: A scale-up approach for efficient solar fuel (hydrogen) generation.* International Journal of Hydrogen Energy, 2024. **95**: p. 185-211.
26. Wang, H., et al., *Efficient hydrogen peroxide production: Enhancing electron transfer on PANI/CdS photocatalysts in aqueous solution.* Journal of Environmental Chemical Engineering, 2024. **12**(6): p. 114979.
27. Wang, J., et al., *Surface plasmon assisted photocatalytic hydrogen generation with Ag decorated g-C_3N_4 coupled SnO_2 nanophotocatalyst under visible-light driven photocatalysis.* International Journal of Hydrogen Energy, 2023. **48**(57): p. 21674-21685.
28. Arabacı, B., et al., *Integrating experimental and machine learning approaches for predictive analysis of photocatalytic hydrogen evolution using Cu/g-C_3N_4.* Renewable Energy, 2024. **237**: p. 121737.
29. Nagar, O.P. and N. Chouhan, *Non-metal doped graphitic carbon nitride (g-C_3N_4): Prospects and review on hydrogen generation via water splitting.* International Journal of Hydrogen Energy, 2024. **96**: p. 533-565.

30. Yang, F., et al., *Formation of monodispersed anatase TiO2 spheres from $TiOSO_4$ for enhanced hydrogen evolution of TiO2/g-C3N4 photocatalysts.* Journal of Environmental Chemical Engineering, 2024. **12**(6): p. 114888.
31. Zhang, B., et al., *Piezoelectric assisted boosting photocatalytic hydrogen evolution over a finely prepared $Pt/TiO_2/g\text{-}C_3N_4$ composite system using lactic acid as sacrificial agent.* International Journal of Hydrogen Energy, 2024. **84**: p. 480-490.
32. Muthukumar, R. and G. Balaji, *Noble metal-free ternary $MoS_2/g\text{-}C_3N_4/ZnIn_2S_4$ heterojunction with efficient charge transfer for highly efficient photocatalytic H_2 production.* Diamond and Related Materials, 2025. **152**: p. 111941.
33. Pan, F., et al., *Visible light driven hydrogen generation and pollutant degradation with Au loaded 2D/2D heterojunctional nanocomposite of MoS_2 and $g\text{-}C_3N_4$.* International Journal of Hydrogen Energy, 2024. **51**: p. 1141-1153.
34. Luna, A.L., et al., *Photocatalytic Hydrogen Evolution Using Ni–Pd/TiO_2: Correlation of Light Absorption, Charge-Carrier Dynamics, and Quantum Efficiency.* The Journal of Physical Chemistry C, 2017. **121**(26): p. 14302-14311.
35. Liu, X., et al., *Type II/Schottky heterojunctions-triggered multi-channels charge transfer in Pd-TiO_2-Cu_2O hybrid promotes photocatalytic hydrogen production.* Journal of Colloid and Interface Science, 2025. **685**: p. 173-185.
36. Qi, X., et al., *Photocatalytic degradation of PET coupled to green hydrogen generation using flexible $Ni_2P/TiO_2/C$ nanofiber film catalysts.* Applied Catalysis A: General, 2023. **656**: p. 119130.
37. Ribag, K., et al., *Enhancing the hydrogen production of tetragonal silicon carbide (t-SiC) with biaxial tensile strain and pH.* Materials Science and Engineering: B, 2025. **311**: p. 117854.
38. Soni, V., et al., *Recent updates on full solar spectrum metal sulphides photocatalyst for hydrogen peroxide generation: Modification strategies and mechanistic insights.* Journal of Environmental Chemical Engineering, 2025. **13**(1): p. 115151.
39. Hsu, C.-Y., et al., *Nano titanium oxide (nano-TiO_2): A review of synthesis methods, properties, and applications.* Case Studies in Chemical and Environmental Engineering, 2024. **9**: p. 100626.
40. Sekar, M., et al., *An investigation on the synthesis and characterization of MoS_2 nanoflowers draped $g\text{-}C_3N_4$ nano sheet ($g\text{-}C_3N_4$ / MoS_2 / MnOOH) ternary composite for the efficient photocatalytic applications.* Chemical Physics Impact, 2024. **9**: p. 100665.
41. Van Tuan, P., N.D. Hung, and L.T. Ha, *Effect of rGO on the microstructure, electrical, optical, and photocatalytic properties of ZnO/rGO nanorods.* Journal of Molecular Structure, 2025. **1330**: p. 141515.
42. Jawale, N., et al., *Enhanced photocatalytic performance of hydrothermally synthesized TiO_2 nanowires for H_2 production via water splitting.* Next Energy, 2025. **6**: p. 100205.

43. Zha, M., et al., *2D/2D layered $Bi_{12}O_{15}Cl_6/Bi_4O_5Br_2$ heterostructure facilitated photocatalytic CO2 reduction in aerobic environments.* Separation and Purification Technology, 2025. **368**: p. 132995.
44. Zhao, D., et al., *Microwave assisted metal-free catalysts preparation from waste plastics for efficient pollutants degradation: Interesting relationship between plastic types and nonradical/radical pathways.* Chinese Chemical Letters, 2025: p. 111631.
45. Li, J., et al., *Preparation of core-shell structure Ag@TiO_2 plasma photocatalysts and reduction of Cr(VI): Size dependent and LSPR effect.* Environmental Research, 2024. **248**: p. 118265.
46. Wu, Y.-Z. and W.J. Tseng, *Preparation of ZnO@ZnS core-shell nanorod arrays with enhanced photocurrent for removal of methylene blue dyes in wastewater.* Open Ceramics, 2025. **21**: p. 100756.
47. El Boraei, N.F., et al., *Facile synthesis of $Fe_{2.96}Cr_{0.03}Ni_{0.01}O_4$@Ag core-shell nanoparticles and its efficient applications in green hydrogen generation and in removing hazardous dyes.* Surfaces and Interfaces, 2025. **56**: p. 105486.
48. Reddy, B.P., et al., *Hierarchical Copper Indium Sulfide and MXene Composites: Synergistic Effects for Enhanced Lithium-Ion Battery Performance and Photocatalytic Hydrogen Production.* Ceramics International, 2025.
49. Kumar, R., D. Das, and A.K. Singh, *C_2N/WS_2 van der Waals type-II heterostructure as a promising water splitting photocatalyst.* Journal of Catalysis, 2018. **359**: p. 143-150.
50. Wang, K., et al., *The Construction of Type II $Cu_2O/ZnFe_2O_4$ Heterojunction Promoted the Photocatalytic Hydrogen Production Activity.* Catalysis Letters, 2024. **154**(12): p. 6227-6240.
51. Ning, Y., et al., *Novel hollow core-shell $Zn_{0.5}Cd_{0.5}S@ZnIn_2S_4/MoS_2$ nanocages with Z-scheme heterojunction for enhanced photocatalysis of hydrogen generation.* Journal of Colloid and Interface Science, 2024. **662**: p. 928-940.
52. Liu, B., et al., *Photo-reduction assisted synthesis of W-doped TiO_2 coupled with Au nanoparticles for highly efficient photocatalytic hydrogen evolution.* CrystEngComm, 2017. **19**(4): p. 675-683.
53. Yan, K., et al., *Recent advances in graphite carbon nitride-based nanocomposites: structure, antibacterial properties and synergies.* Nanoscale Advances, 2021. **3**.
54. Zhang, S., et al., *Chiral induction enhances hydrogen generation performance of CdS quantum dots.* International Journal of Hydrogen Energy, 2023. **48**(87): p. 33903-33912.
55. Shen, Z.-K., et al., *Black phosphorus photocatalysts for photocatalytic H_2 generation: A review.* Chemical Engineering Journal, 2020. **386**: p. 123997.
56. Sharma, K., et al., *Unraveling the synergism mechanistic insight of O-vacancy and interfacial charge transfer in WO_3-x decorated on Ag_2CO_3/BiOBr for photocatalysis of water pollutants: Based on experimental and density functional theory (DFT) studies.* Environmental Research, 2024. **260**: p. 119610.

57. Wang, L., et al., *Machine learning and DFT dual-guidance of carbon dots implanted $SrTiO_3$ hollow nanosphere for efficient all-pH-value photocatalysis.* Journal of Materials Science & Technology, 2025. **217**: p. 169-181.
58. Zhang, B., et al., *Effect for the electronic configurations of $LuVO_4$ induced by D4h crystal-field-splitting discovered in the systematic DFT investigation on photocatalysis capacities of vanadates.* Materials Today Chemistry, 2023. **29**: p. 101395.
59. Wang, B., et al., *Synthesis and enhanced microwave absorption properties of $Ni@Ni_2O_3$ core–shell particles.* Journal of Alloys and Compounds, 2013. **567**: p. 21-25.
60. Viswanathan, A. and A.N. Shetty, *High energy supercapacitance of magnetic $PANI/Ni_2O_3$ nanocomposite and its magnetic structural repair.* Journal of Energy Storage, 2024. **90**: p. 111759.
61. Shaban, M., et al., *Photocatalytic removal of Congo red dye using MCM-48/Ni_2O_3 composite synthesized based on silica gel extracted from rice husk ash; fabrication and application.* Journal of Environmental Management, 2017. **204**: p. 189-199.
62. Sayed, M.A., et al., *Photocatalytic hydrogen generation from raw water using zeolite/polyaniline@Ni_2O_3 nanocomposite as a novel photo-electrode.* Energy, 2019. **187**: p. 115943.
63. Wang, Y., et al., *Investigation on the synergistic effect in multiple active centers (Pd/Ni/PdO/NiO/Ni_2O_3) in situ formed on the surface of the self-assembly β-ketoimide Pd(II)/Ni(II) film anchored on graphene oxide for Suzuki-Miyaura cross-coupling reaction.* Molecular Catalysis, 2024. **555**: p. 113843.
64. Şeşe, A. and M.S. Akkus, *TiO_2-coated thin films: A catalyst for sustainable hydrogen production from potassium borohydride.* International Journal of Hydrogen Energy, 2025.
65. Maitlo, H.A., B. Anand, and K.-H. Kim, *TiO_2-based photocatalytic generation of hydrogen from water and wastewater.* Applied Energy, 2024. **361**: p. 122932.
66. Rahul, T.K., M. Mohan, and N. Sandhyarani, *Enhanced Solar Hydrogen Evolution over In Situ Gold–Platinum Bimetallic Nanoparticle-Loaded Ti^{3+} Self-Doped Titania Photocatalysts.* ACS Sustainable Chemistry & Engineering, 2018. **6**(3): p. 3049-3059.
67. Wang, X.H., et al., *Wavelength-Sensitive Photocatalytic Degradation of Methyl Orange in Aqueous Suspension over Iron(III)-doped TiO_2 Nanopowders under UV and Visible Light Irradiation.* The Journal of Physical Chemistry B, 2006. **110**(13): p. 6804-6809.
68. Reddy, N.L., et al., *Multifunctional Cu/Ag quantum dots on TiO2 nanotubes as highly efficient photocatalysts for enhanced solar hydrogen evolution.* Journal of Catalysis, 2017. **350**: p. 226-239.
69. El-Bery, H.M., et al., *Enhancing photocatalytic hydrogen generation on TiO_2 using thermally derived nickel-based cocatalysts from Hofmann-type cyanide coordination polymer flakes.* International Journal of Hydrogen Energy, 2024. **78**: p. 470-480.

70. Liao, Y.-X., et al., *TiN/TiO_2 embedded in ReS_2 nanoflowers with wide light absorption and multi-interfacial charge transfer for efficient photocatalytic hydrogen generation.* Applied Surface Science, 2025. **682**: p. 161708.
71. Mandari, K.K., et al., *Rare earth metal Gd influenced defect sites in N doped TiO_2: Defect mediated improved charge transfer for enhanced photocatalytic hydrogen production.* International Journal of Hydrogen Energy, 2018. **43**(4): p. 2073-2082.
72. Han, X., et al., *Ti3C2 MXene-derived carbon-doped TiO_2 coupled with g-C_3N_4 as the visible-light photocatalysts for photocatalytic H_2 generation.* Applied Catalysis B: Environmental, 2020. **265**: p. 118539.
73. Wei, X., et al., *Facile in situ synthesis of plasmonic nanoparticles-decorated g-C_3N_4/TiO_2 heterojunction nanofibers and comparison study of their photosynergistic effects for efficient photocatalytic H2 evolution.* Nanoscale, 2016. **8**(21): p. 11034-11043.
74. Li, Y.-F., et al., *Modification of electron transfer paths in CdS-TiO_2 Z-type heterojunction by cobalt-based complexes for boosting visible-light photocatalytic hydrogen evolution.* Journal of Alloys and Compounds, 2024. **1002**: p. 175324.
75. Zhou, Y., et al., *Double shell composite nanoarchitectonics of Cu_2O core with TiO2/metal-organic frameworks for efficient hydrogen generation.* International Journal of Hydrogen Energy, 2023. **48**(2): p. 629-639.
76. Mohamed, R.M., et al., *Novel construction of heterojunction NiS/$ZnWO_4$ S-scheme photocatalysts with boosted photocatalytic hydrogen evolution under visible light.* Materials Science in Semiconductor Processing, 2025. **200**: p. 109907.
77. Liu, Y., et al., *In-situ photodeposition of co-catalyst Ni_2P on CdS for photocatalytic conversion of ethanol for synergistic hydrogen production.* Journal of Fuel Chemistry and Technology, 2024. **52**(11): p. 1629-1640.
78. Gomaa, H.E., et al., *Unlocking high-performance hydrogen evolution: Argon-induced Ni segregation in NiO/TiO_2 of core/shell catalysts.* International Journal of Hydrogen Energy, 2024. **86**: p. 1010-1019.
79. Wang, Z., et al., *Mo-doped Ni/NiO as a highly efficient and stable electrocatalyst for the hydrogen evolution reaction.* International Journal of Hydrogen Energy, 2025. **166**: p. 151037.
80. Huang, J., et al., *Efficient photocatalytic hydrogen production over Rh and Nb codoped TiO_2 nanorods.* Chemical Engineering Journal, 2018. **337**: p. 282-289.
81. Montoya, A.T. and E.G. Gillan, *Enhanced Photocatalytic Hydrogen Evolution from Transition-Metal Surface-Modified TiO_2.* ACS Omega, 2018. **3**(3): p. 2947-2955.
82. Zhang, W., et al., *Photocatalytic hydrogen production from methanol aqueous solution under visible-light using Cu/S–TiO_2 prepared by electroless plating method.* Catalysis Communications, 2015. **59**: p. 189-194.
83. Luo, S., et al., *Enhanced, robust light-driven H2 generation by gallium-doped titania nanoparticles.* Physical Chemistry Chemical Physics, 2018. **20**(3): p. 2104-2112.

84. Ouyang, W., et al., *Enhancing photocatalytic performance of TiO_2 in H_2 evolution via Ru co-catalyst deposition.* Applied Catalysis B: Environmental, 2018. **238**: p. 434-443.
85. El-Shazly, A.N., et al., *Novel facet-engineered multi-doped TiO_2 mesocrystals with unprecedented visible light photocatalytic hydrogen production.* Solar Energy Materials and Solar Cells, 2021. **220**: p. 110825.
86. Montoya, A.T. and E.G. Gillan, *Enhanced Photocatalytic Hydrogen Evolution from Transition-Metal Surface-Modified TiO_2.* ACS Omega, 2018. **3**(3): p. 2947-2955.
87. Ismael, M., *Enhanced photocatalytic hydrogen production and degradation of organic pollutants from Fe (III) doped TiO_2 nanoparticles.* Journal of Environmental Chemical Engineering, 2020. **8**(2): p. 103676.
88. Tahir, B. and M. Tahir, *Morphological effect of 1D/1D In_2O_3/TiO_2 NRs/NWs heterojunction photo-embedded with Cu-NPs for enhanced photocatalytic H2 evolution under visible light.* Applied Surface Science, 2020. **506**: p. 145034.
89. Fujita, S.-i., et al., *Photocatalytic hydrogen production from aqueous glycerol solution using NiO/TiO_2 catalysts: Effects of preparation and reaction conditions.* Applied Catalysis B: Environmental, 2016. **181**: p. 818-824.
90. Jouini, K., et al., *Investigation of gamma-ray irradiation induced phase change from NiO to Ni2O3 for enhancing photocatalytic performance.* Optik, 2019. **195**: p. 163109.
91. Zhang Yu , Q.Y., *Prepration and application of NiO nanoparticles.* Journal of Chemical Industry & Engineering, 2009.
92. XIA Yun-sheng, L.J.-t., LU Qi-lin,BAO De-cai, *Preparation and characterization of high surface area mesoporous nickel oxide.* Chemical Research and Applications, 2015. **27**: p. 127-132.
93. Wang, Y., et al., *Preparation of NiO nanoparticles and their catalytic activity in the thermal decomposition of ammonium perchlorate.* Thermochimica Acta, 2005. **437**(1): p. 106-109.
94. Hosny, N.M., *Synthesis, characterization and optical band gap of NiO nanoparticles derived from anthranilic acid precursors via a thermal decomposition route.* Polyhedron, 2011. **30**(3): p. 470-476.
95. Karatutlu, A., A. Barhoum, and A. Sapelkin, *Chapter 1 - Liquid-phase synthesis of nanoparticles and nanostructured materials*, in *Emerging Applications of Nanoparticles and Architecture Nanostructures*, A. Barhoum and A.S.H. Makhlouf, Editors. 2018, Elsevier. p. 1-28.
96. Bahadur, J., et al., *Effect of heat treatment on pore structure in nano-crystalline NiO: A small angle neutron scattering study.* Journal of Solid State Chemistry, 2008. **181**(5): p. 1227-1235.
97. Deng, X. and Z. Chen, *Preparation of nano-NiO by ammonia precipitation and reaction in solution and competitive balance.* Materials Letters, 2004. **58**(3): p. 276-280.
98. Thota, S. and J. Kumar, *Sol–gel synthesis and anomalous magnetic behaviour of NiO nanoparticles.* Journal of Physics and Chemistry of Solids, 2007. **68**(10): p. 1951-1964.

99. Cao, S., et al., *Hydrothermal synthesis of nanoparticles-assembled NiO microspheres and their sensing properties.* Physica E: Low-dimensional Systems and Nanostructures, 2020. **118**: p. 113655.
100. Han, D.Y., et al., *Synthesis and size control of NiO nanoparticles by water-in-oil microemulsion.* Powder Technology, 2004. **147**(1): p. 113-116.
101. Tao, D. and F. Wei, *New procedure towards size-homogeneous and well-dispersed nickel oxide nanoparticles of 30 nm.* Materials Letters, 2004. **58**(25): p. 3226-3228.
102. Munkaila, S., et al., *Polymer directed synthesis of NiO nanoflowers to remove pollutant from wastewater.* Journal of Molecular Liquids, 2021. **324**: p. 114676.
103. Pan, T., et al., *Facile homogeneous precipitation method to prepare MnO2 with high performance in catalytic oxidation of ethyl acetate.* Chemical Engineering Journal, 2021. **417**: p. 129246.
104. Kumar, A. and S.S. Han, *Chapter 13 - Bioactive glass–based composites in bone tissue engineering: synthesis, processing, and cellular responses*, in *Materials for Biomedical Engineering*, A.-M. Holban and A.M. Grumezescu, Editors. 2019, Elsevier. p. 397-439.
105. Zorkipli, N.N.M., N.H.M. Kaus, and A.A. Mohamad, *Synthesis of NiO Nanoparticles through Sol-gel Method.* Procedia Chemistry, 2016. **19**: p. 626-631.
106. Pooyandeh, S., et al., *In situ deposition of NiO nano particles on cotton fabric using sol–gel method- photocatalytic activation properties.* Journal of Materials Research and Technology, 2021. **12**: p. 1-14.
107. Sree, G.S., et al., *Enhanced UV–Visible triggered photocatalytic degradation of Brilliant green by reduced graphene oxide based NiO and CuO ternary nanocomposite and their antimicrobial activity.* Arabian Journal of Chemistry, 2020. **13**(4): p. 5137-5150.
108. Adschiri, T., K. Kanazawa, and K.I. Arai, *Rapid and Continuous Hydrothermal Synthesis of Boehmite Particles in Subcritical and Supercritical Water.* ChemInform, 1992. **23**.
109. Lv, Y., et al., *A simple and promoter free way to synthesize spherical γ-alumina with high hydrothermal stability.* Materials Letters, 2015. **155**: p. 75-77.
110. Malik, M.A., M.Y. Wani, and M.A. Hashim, *Microemulsion method: A novel route to synthesize organic and inorganic nanomaterials: 1st Nano Update.* Arabian Journal of Chemistry, 2012. **5**(4): p. 397-417.
111. Ita, K., *Chapter 6 - Microemulsions*, in *Transdermal Drug Delivery*, K. Ita, Editor. 2020, Academic Press. p. 97-122.
112. Crichton, R.R., *Chapter 2 - Basic Coordination Chemistry for Biologists*, in *Biological Inorganic Chemistry (Second Edition)*, R.R. Crichton, Editor. 2012, Elsevier: Oxford. p. 21-34.
113. Xiao—Zhao, L.S.-F.W.C.Y.H., *Preparation of Nanoscale NiO Powders by Polymer-network Gel Process.* CHINESE JOURNAL OF INORGANIC CHEMISTRY, 2003.

114. Imran Din, M. and A. Rani, *Recent Advances in the Synthesis and Stabilization of Nickel and Nickel Oxide Nanoparticles: A Green Adeptness.* International Journal of Analytical Chemistry, 2016. **2016**: p. 3512145.
115. Arumugam, J., et al., *Green synthesis of zinc oxide nanoparticles using Ficus carica leaf extract and their bactericidal and photocatalytic performance evaluation.* Chemical Physics Letters, 2021. **783**: p. 139040.
116. Sabouri, Z., et al., *Plant-based synthesis of cerium oxide nanoparticles using Rheum turkestanicum extract and evaluation of their cytotoxicity and photocatalytic properties.* Materials Technology, 2020: p. 1-14.
117. Najjar, M., et al., *Preparation of tin oxide (IV) nanoparticles by a green chemistry method and investigation of its role in the removal of organic dyes in water purification.* Research on Chemical Intermediates, 2020. **46**(4): p. 2155-2168.
118. Sabouri, Z., et al., *Tragacanth-mediate synthesis of NiO nanosheets for cytotoxicity and photocatalytic degradation of organic dyes.* Bioprocess and Biosystems Engineering, 2020. **43**(7): p. 1209-1218.
119. Sabouri, Z., et al., *Green-based bio-synthesis of nickel oxide nanoparticles in Arabic gum and examination of their cytotoxicity, photocatalytic and antibacterial effects.* Green Chemistry Letters and Reviews, 2021. **14**(2): p. 404-414.
120. Shah, M., et al., *Green Synthesis of Metallic Nanoparticles via Biological Entities.* Materials, 2015. **8**(11): p. 7278-7308.
121. Wuled Lenggoro, I., et al., *Control of size and morphology in NiO particles prepared by a low-pressure spray pyrolysis.* Materials Research Bulletin, 2003. **38**(14): p. 1819-1827.
122. Oh, S.W., et al., *Effect of calcination temperature on morphology, crystallinity and electrochemical properties of nano-crystalline metal oxides (Co3O4, CuO, and NiO) prepared via ultrasonic spray pyrolysis.* Journal of Power Sources, 2007. **173**(1): p. 502-509.
123. Moravec, P., et al., *NiOx Nanoparticle Synthesis by Chemical Vapor Deposition from Nickel Acetylacetonate.* Materials Sciences and Applications, 2011. **2**: p. 258-264.
124. Hosny, N.M., *Synthesis, characterization and optical band gap of NiO nanoparticles derived from anthranilic acid precursors via a thermal decomposition route.* Polyhedron, 2011. **30**: p. 470-476.
125. Barakat, A., et al., *One Step Synthesis of NiO Nanoparticles via Solid-State Thermal Decomposition at Low-Temperature of Novel Aqua(2,9-dimethyl-1,10-phenanthroline)$NiCl_2$ Complex.* International Journal of Molecular Sciences, 2013. **14**(12): p. 23941-23954.
126. Han, D., et al., *Synthesis and size control of NiO nanoparticles by water-in-oil microemulsion.* Powder Technology, 2004. **147**: p. 113-116.
127. Liu, S.F., C.Y. Wu, and X.Z. Han, *Preparation of nanoscale NiO powders by polymer-network gel process.* Chinese Journal of Inorganic Chemistry, 2003. **19**: p. 624-626.
128. Jensen, K.F., *Flow chemistry—Microreaction technology comes of age.* AIChE Journal, 2017. **63**(3): p. 858-869.

129. Shepherd, S.J., D. Issadore, and M.J. Mitchell, *Microfluidic formulation of nanoparticles for biomedical applications.* Biomaterials, 2021. **274**: p. 120826.
130. Zhang, J., et al., *Design and Scaling Up of Microchemical Systems: A Review.* Annual Review of Chemical and Biomolecular Engineering, 2017. **8**(1): p. 285-305.
131. Wang, K., Y. Lu, and G. Luo, *Strategy for Scaling-up of a Microsieve Dispersion Reactor.* Chemical Engineering & Technology, 2014. **37**(12): p. 2116-2122.
132. Jocic, D., *14 - Smart coatings for comfort in clothing*, in *Active Coatings for Smart Textiles*, J. Hu, Editor. 2016, Woodhead Publishing. p. 331-354.
133. Wang, Y., et al., *Preservative effects of allicin microcapsules on daily foods.* LWT, 2018. **98**: p. 225-230.
134. Dai, X., et al., *Enhanced radiotherapy efficacy and induced anti-tumor immunity in HCC by improving hypoxia microenvironment using oxygen microcapsules.* Chemical Engineering Journal, 2021. **422**: p. 130109.
135. Yip, J. and M.Y.A. Luk, *3 - Microencapsulation technologies for antimicrobial textiles*, in *Antimicrobial Textiles*, G. Sun, Editor. 2016, Woodhead Publishing. p. 19-46.
136. Zhang, W., L.P. Liao, and Y. Zhao, *12 - Incorporating microcapsules in smart coatings for corrosion protection of steel*, in *Handbook of Smart Coatings for Materials Protection*, A.S.H. Makhlouf, Editor. 2014, Woodhead Publishing. p. 287-306.
137. Zhao, Y., et al., *Microfluidic interface boosted synthesis of covalent organic polymer capsule.* Green Chemical Engineering, 2020. **1**(1): p. 63-69.
138. Lian, Z., et al., *Synergetic treatment of dye contaminated wastewater using microparticles functionalized with carbon nanotubes/titanium dioxide nanocomposites.* RSC Advances, 2020. **10**(16): p. 9210-9225.
139. Du, L., et al., *Controllable Preparation of SiO_2 Nanoparticles Using a Microfiltration Membrane Dispersion Microreactor.* Industrial & Engineering Chemistry Research, 2011. **50**(14): p. 8536-8541.
140. Du, L., et al., *Process intensification of BaSO4 nanoparticle preparation with agitation of microbubbles.* Powder Technology, 2013. **247**: p. 60-68.
141. Wang, K., et al., *Enhancement of Mixing and Mass Transfer Performance with a Microstructure Minireactor for Controllable Preparation of $CaCO_3$ Nanoparticles.* Industrial & Engineering Chemistry Research, 2007. **46**(19): p. 6092-6098.
142. Chen, T., S. Yin, and J. Wu, *Nanomaterials meet microfluidics: Improved analytical methods and high-throughput synthetic approaches.* TrAC Trends in Analytical Chemistry, 2021. **142**: p. 116309.
143. Liang, H., et al., *Highly-ordered microstructure and well performance of $LiNi_{0.6}Mn_{0.2}Co_{0.2}O_2$ cathode material via the continuous microfluidic synthesis.* Chemical Engineering Journal, 2020. **394**: p. 124846.
144. Kockmann, N., et al., *Convective mixing and chemical reactions in microchannels with high flow rates.* Sensors and Actuators B: Chemical, 2006. **117**(2): p. 495-508.

145. Kawasaki, S.-I., et al., *Engineering study of continuous supercritical hydrothermal method using a T-shaped mixer: Experimental synthesis of NiO nanoparticles and CFD simulation.* The Journal of Supercritical Fluids, 2010. **54**(1): p. 96-102.
146. Sue, K., et al., *Continuous Hydrothermal Synthesis of Nickel Ferrite Nanoparticles Using a Central Collision-Type Micromixer: Effects of Temperature, Residence Time, Metal Salt Molality, and NaOH Addition on Conversion, Particle Size, and Crystal Phase.* Industrial & Engineering Chemistry Research, 2011. **50**(16): p. 9625-9631.
147. Sue, K., et al., *Continuous hydrothermal synthesis of Fe_2O3, NiO, and CuO nanoparticles by superrapid heating using a T-type micro mixer at 673K and 30MPa.* Chemical Engineering Journal, 2011. **166**(3): p. 947-953.
148. Kiwamu, S., et al., *Hydrothermal-reduction Synthesis of Ni Nanoparticles by Superrapid Heating Using a Micromixer.* Chemistry Letters, 2009. **38**(11): p. 1018-1019.
149. Zhao, D., et al., *Controllable construction of micro/nanostructured NiO arrays in confined microchannels via microfluidic chemical fabrication for highly efficient and specific absorption of abundant proteins.* Journal of Materials Chemistry B, 2015. **3**(20): p. 4272-4281.
150. Zardi, P., T. Carofiglio, and M. Maggini, *Mild Microfluidic Approaches to Oxide Nanoparticles Synthesis.* Chemistry – A European Journal, 2022. **28**(9): p. e202103132.
151. Dincau, B., et al., *Clog mitigation in a microfluidic array via pulsatile flows.* Soft Matter, 2022. **18**(9): p. 1767-1778.
152. Hou, R., et al., *BiOCl modified TiO_2 based catalyst with enhanced hydrogen generation properties under visible light via promote photogenerated electron-hole separation.* Materials Today Physics, 2024. **44**: p. 101426.
153. Mabaleha, S.S., et al., *Microfluidic synthesis of MOFs, COFs, and HOFs: Insights and advances.* Materials Science and Engineering: R: Reports, 2025. **165**: p. 101005.
154. Gong, M., et al., *Nanoscale nickel oxide/nickel heterostructures for active hydrogen evolution electrocatalysis.* Nature Communications, 2014. **5**(1): p. 4695.
155. Finkbeiner, M., et al., *The New International Standards for Life Cycle Assessment: ISO 14040 and ISO 14044.* The International Journal of Life Cycle Assessment, 2006. **11**(2): p. 80-85.
156. Bastianoni, S., et al., *The connection between 2006 IPCC GHG inventory methodology and ISO 14064-1 certification standard – A reference point for the environmental policies at sub-national scale.* Environmental Science & Policy, 2014. **44**: p. 97-107.
157. *2006 IPCC Guidelines for National Greenhouse Gas Inventories*. 2019, IPCC: Cambridge University Press.
158. *Pre-sustainability*. 2012; Available from: http://www.pre-sustainability.com/simapro-lca-software.
159. Herrmann, I.T. and A. Moltesen, *Does it matter which Life Cycle Assessment (LCA) tool you choose? – a comparative assessment of SimaPro and GaBi.* Journal of Cleaner Production, 2015. **86**: p. 163-169.

160. Wang, C., et al., *The status and improvement opportunities towards carbon neutrality of a university campus in China: A case study on energy transition and innovation perspectives.* Journal of Cleaner Production, 2023. **414**: p. 137521.
161. IPCC, *Guidelines for National Greenhouse Gas Inventories*. 2006. p. 28.
162. El Sharkawy, H.M., M.A. Abo El-Khair, and A.S. Morshedy, *Construction of SnS_2@SnO_2 nanocomposite Z-scheme heterojunction for dual-functional photocatalysis: Green hydrogen generation and crystal violet degradation.* International Journal of Hydrogen Energy, 2025. **137**: p. 471-486.
163. *zView User Guide*
164. de Mello, J.C., H.F. Wittmann, and R.H. Friend, *An improved experimental determination of external photoluminescence quantum efficiency.* Advanced Materials, 1997. **9**(3): p. 230-232.
165. Chen, L.-C., et al., *Chapter 20 - Fluorescence Lifetime Imaging Microscopy for Quantitative Biological Imaging*, in *Methods in Cell Biology*, G. Sluder and D.E. Wolf, Editors. 2013, Academic Press. p. 457-488.
166. Zhang, D., et al., *Use of synergistic effects of the co-catalyst, p-n heterojunction, and porous structure for improvement of visible-light photocatalytic H_2 evolution in porous Ni_2O_3/$Mn_{0.2}Cd_{0.8}S$/Cu_3P@Cu_2S.* Journal of Alloys and Compounds, 2020. **845**: p. 155569.
167. Qin, X., et al., *Microfluidic Instruments for Nanoparticle Synthesis.* Biomedical Instrumentation, 2025: p. 100002.
168. Agha, A., et al., *A review on microfluidic-assisted nanoparticle synthesis, and their applications using multiscale simulation methods.* Nanoscale Res Lett, 2023. **18**(1): p. 18.
169. Mou, J., et al., *Nickel oxide nanoparticle synthesis and photocatalytic applications: evolution from conventional methods to novel microfluidic approaches.* Microfluidics and Nanofluidics, 2022. **26**(4): p. 25.
170. Lian, Z., et al., *Microfluidic fabrication of porous polydimethylsiloxane microparticles for the treatment of toluene-contaminated water.* Microfluidics and Nanofluidics, 2018. **22**(12): p. 145.
171. Zhang, Y., et al., *Versatile platform for performing protocols on a chip utilizing surface acoustic wave (SAW) driven mixing.* Lab on a Chip, 2019. **19**(2): p. 262-271.
172. Ryu, K.S., et al., *Micro magnetic stir-bar mixer integrated with parylene microfluidic channels.* Lab on a Chip, 2004. **4**(6): p. 608-613.
173. Wu, Y., et al., *A novel micromixer based on the alternating current-flow field effect transistor.* Lab on a Chip, 2017. **17**(1): p. 186-197.
174. Sasaki, N., T. Kitamori, and H.-B. Kim, *Fluid mixing using AC electrothermal flow on meandering electrodes in a microchannel.* ELECTROPHORESIS, 2012. **33**(17): p. 2668-2673.
175. Chen, X. and H. Lv, *Intelligent control of nanoparticle synthesis on microfluidic chips with machine learning.* NPG Asia Materials, 2022. **14**(1): p. 69.
176. Lian, Z., et al., *Microfluidic formation of highly monodispersed multiple cored droplets using needle-based system in parallel mode.* ELECTROPHORESIS, 2020. **41**(10-11): p. 891-901.

177. Pan, H., et al., *Interfacial composite FeOOH enhanced efficient electrocatalytic oxygen evolution of $NiSe_2/Ni_2O_3$.* Journal of Alloys and Compounds, 2022. **926**: p. 166779.
178. Narsimulu, D., et al., *Nitrogen-doped reduced graphene oxide incorporated Ni_2O_3-Co_3O_4@MoS_2 hollow nanocubes for high-performance energy storage devices.* Journal of Alloys and Compounds, 2022. **922**: p. 166131.
179. Gong, J., et al., *Catalytic carbonization of polypropylene by the combined catalysis of activated carbon with Ni_2O_3 into carbon nanotubes and its mechanism.* Applied Catalysis A: General, 2012. **449**: p. 112-120.
180. David B. Williams, C.B.C., *Transmission Electron Microscopy*. 2009: Springer New York, NY. LXII, 775.
181. Joseph I. Goldstein, D.E.N., Joseph R. Michael, Nicholas W.M. Ritchie, John Henry J. Scott, David C. Joy, *Scanning Electron Microscopy and X-Ray Microanalysis*. 2017: Springer New York, NY. XXIII, 550.
182. Sari, Y., et al., *A review of TiO_2 photocatalyst for organic degradation and sustainable hydrogen energy production.* International Journal of Hydrogen Energy, 2024. **55**: p. 984-996.
183. Zheng, Y., M. Ma, and H. Shao, *Recent advances in efficient and scalable solar hydrogen production through water splitting.* Carbon Neutrality, 2023. **2**(1): p. 23.
184. Zhao, Y., et al., *Techno-economic analysis of converting low-grade heat into electricity and hydrogen.* Carbon Neutrality, 2023. **2**(1): p. 19.
185. Wang, T., X. Cao, and L. Jiao, *PEM water electrolysis for hydrogen production: fundamentals, advances, and prospects.* Carbon Neutrality, 2022. **1**(1): p. 21.
186. Wang, C., Y. Wei, and L. Gao, *A flexible hydrogen-electricity coproduction system through the decoupling of units with different dynamic characteristics.* Carbon Neutrality, 2023. **2**(1): p. 4.
187. Fontelles-Carceller, O., et al., *Measuring and interpreting quantum efficiency for hydrogen photo-production using Pt-titania catalysts.* Journal of Catalysis, 2017. **347**: p. 157-169.
188. Martínez-García, H., et al., *Rationally designed C_3N_4/ TiO_2 (anatase/brookite) heterojunction for enhanced photocatalytic hydrogen generation under visible light.* Ceramics International, 2023. **49**(21): p. 33901-33911.
189. Mu, X., et al., *Efficient photocatalytic hydrogen generation by CeCO3OH/TiO_2 composites.* International Journal of Hydrogen Energy, 2024. **63**: p. 1174-1181.
190. Jiang, X., et al., *Bimetallic CuCo nanoparticles optimized hydrogen generation active centers thereby significantly enhancing TiO_2 photocatalytic activity.* International Journal of Hydrogen Energy, 2024. **64**: p. 120-131.
191. Bello, M.O., et al., *Na-Y zeolite supported TiO_2/Pd nanoparticles for enhanced photoredox catalytic properties and green hydrogen generation.* Catalysis Communications, 2024. **186**: p. 106817.
192. Gnanasekaran, L., et al., *Mesoporous NiO/Ni_2O_3 nanoflowers for favorable visible light photocatalytic degradation of 4-chlorophenol.* Environmental Research, 2023. **236**: p. 116790.

193. Ma, L., et al., *In situ synthesis of CNTs/Fe–Ni/TiO_2 nanocomposite by fluidized bed chemical vapor deposition and the synergistic effect in photocatalysis.* Particuology, 2014. **14**: p. 24-32.
194. Bai, D.S., R.P. Suvarna, and B.M. Nagabhushana, *Synthesis, characterization and electrical properties of PANI-Ni2O3 nanocomposites.* Materials Today: Proceedings, 2018. **5**(10, Part 1): p. 20793-20802.
195. Mashentseva, A.A., D.T. Nurpeisova, and M. Barsbay, *Effect of copper doping on the photocatalytic performance of Ni_2O3@PC membrane composites in norfloxacin degradation.* RSC Advances, 2024. **14**(7): p. 4424-4435.
196. Patel, A., et al., *Investigation of structural, electrical and optical properties of SbXW1-XSe_2 single crystals.* Materials Science in Semiconductor Processing, 2018. **81**: p. 108-112.
197. Patel, M., P.M. Pataniya, and C.K. Sumesh, *Enhanced photoresponse by plasmon resonance in Ni-WS_2/Si photodiode.* Materials Research Bulletin, 2022. **145**: p. 111518.
198. Chauhan, P., et al., *Engineered interfaces of WSe_2/rhenium doped $SnSe_2$ heterostructures nanosheet arrays for superior hydrogen generation and flexible supercapacitor.* Materials Today Chemistry, 2022. **26**: p. 101079.
199. *Kyoto Protocol*. 2023, Britannica, The Editors of Encyclopaedia.
200. *Kyoto Protocol Reference*. 2008, UNFCCC.
201. Wang, X., et al., *Integration of the grey relational analysis with machine learning for sucrose anaerobic hydrogen production prediction.* International Journal of Hydrogen Energy, 2024. **68**: p. 388-397.
202. Noh, W., et al., *Systems design and techno-economic analysis of a novel cryogenic carbon capture process integrated with an air separation unit for autothermal reforming blue hydrogen production system.* Journal of Cleaner Production, 2024. **457**: p. 142341.
203. Horri, B.A. and H. Ozcan, *Green Hydrogen Production by Water Electrolysis: Current Status and Challenges.* Current Opinion in Green and Sustainable Chemistry, 2024: p. 100932.
204. *CPCD, China Products Crabon Footprint Factors Database*, C.C.G.G.W. Group, Editor. 2025.
205. Nambyaruveettil, S., et al., *A novel Ni–zeolite–biochar green catalyst: optimization of composition and preparation strategy revealed by TPR, TPD, and XPS.* Materials Science and Engineering: B, 2025. **321**: p. 118566.
206. Ribière, N., et al., *XPS and TEM characterization of oxides formed in simulated primary water on steam generator tubes made of Ni based alloy.* Corrosion Science, 2025. **249**: p. 112823.
207. Jamshaid, M., et al., *Enhancement of visible light-induced photocatalytic degradation of tetracycline through highly efficient NiO/TiO_2 p-n heterojunction catalysts.* Polyhedron, 2025. **268**: p. 117371.